An Experimental and Numerical Study of Granular Hopper Flows

A Thesis
Presented to
The Academic Faculty

by

Matthew James Sandlin

In Partial Fulfillment
Of the Requirements for the Degree
Master of Science in Mechanical Engineering

Georgia Institute of Technology

December, 2013

An Experimental and Numerical Study of Granular Hopper Flows

Approved by:

Dr. Sheldon Jeter, advisor
School of Mechanical Engineering
Georgia Institute of Technology

Dr. Said Abdel-Khalik
School of Mechanical Engineering
Georgia Institute of Technology

Dr. Peter Loutzenhiser
School of Mechanical Engineering
Georgia Institute of Technology

Date Approved: August 16, 2013

For Mom, Dad, and Annie

Acknowledgements

I would like to acknowledge several people who made this study possible.

First, I would like to deeply thank Dr. Rick Couvillion of the University of Arkansas, Dr. James Davis of the University of Arkansas, and Mr. Mark Rouk of Public Service Company of Oklahoma. Without the belief of those three, this study could not have even started.

Secondly, I would like to thank the other members of my reading committee, Dr. Said Abdel-Khalik and Dr. Peter Loutzenhiser. Your comments and suggestions provided innumerable improvements to my research and thesis, and like above, made it possible at all.

Thirdly, I would like to thank the other students in Dr. Jeter's research group. You guys helped me in more ways, great and subtle, than I can count. Most importantly, you reminded me that my struggle was not a solitary one.

A special thanks goes to Dennis Sadowski and Matt Golob, the research engineers of Dr. Jeter's group. Your help in the design and construction of the experimental apparatus was critical in the completion of this research.

And finally, thank you Dr. Sheldon Jeter. I don't know how big a part I will play in the theater of concentrated solar power going forward, but I was thrilled to have worked on a project I that I consider so important and fundamental that it made me leave a promising career at a power plant of today to come do research on a power plant of tomorrow.

Table of Contents

List of Tables

List of Figures

Summary

In a proposed design for a concentrated solar power tower, sand is irradiated by solar energy and transfers its energy to another fluid stream by means of a finned tube heat exchanger. To maximize heat transfer and minimize potential damage to the heat exchanger, it is desired to have a very uniform flow through the heat exchanger. However, performing full scale flow tests can be expensive, impractical, and depending upon the specific quantities of interest, unsuitable for revealing the details of what it happening inside of the flow stream.

Thus, the discrete element method has been used to simulate and study particulate flows. In this project, the flow of small glass beads through a square pyramid shaped hopper and a wedge shaped hopper were studied at the lab scale. These flows were also simulated using computers running two versions of discrete element modeling software – EDEM and LIGGGHTS. The simulated results were compared against the lab scale flows and against each other. They show that, in general, the discrete element method can be used to simulate lab scale particulate flows as long as certain material properties are well known, especially the friction properties of the material. The potential for increasing the accuracy of the simulations, such as using better material property data, non-uniform particle size distributions, and non-spherical particle shapes, as well as simulating heat transfer within a granular flow are also discussed.

Chapter 1

Introduction and Motivation

The purpose of this investigation is to asses the suitability for the discrete element method to be used in simulating particulate flows. In general, particulate flows can not be analyzed by simple closed form equations. Therefore, they must be studied as they happen, studied at the lab scale, or otherwise simulated. Depending on the size and complexity of the flow in question, one of the three methods might be preferred over the other two for a given flow.

Particulate flows are of great importance in many fields, including food processing, pharmaceuticals, geology, and in this case, concentrated solar power using sand as the heat transfer and storage medium. While superficially similar to fluid flows, particulate flows in general can not be solved using methods from fluid mechanics. Fluid mechanics treats fluid flows as continua, while a particulate flow is fundamentally different – it is composed of discrete packets of material.

In a proposed design for a concentrated solar power thermal energy storage plant, a granular material such as sand is used as the heat transfer and storage medium. The proposed design takes the form of a power tower, similar to figure 1.

Figure 1 – Abengoa's solar power towers PS10 (top) and PS20 (bottom) in Seville, Spain. The large field of mirrors reflects sunlight towards the top of the power tower, seen in the right of the image. From Abengoa (2009).

In the proposed design, sand is lifted to the top of the tower, where it then falls through a receiver. A large field of movable mirrors, called heliostats, reflects sunlight onto the receiver, causing the sand to absorb solar energy and increase in temperature. The sand then falls into a thermal storage bin where it can either flow through a sand to fluid heat exchanger or can be stored until needed (to generate power at night, for example). To ensure maximum heat exchanger effectiveness, it is desirable to have uniform flow through the storage bin, and thus the heat exchanger. This condition is called mass flow.

Previously, flow experiments were conducted on a full sized hopper with a sand to fluid heat exchanger in the flow path. The inclined section of the hopper was constructed of plates of mill finished carbon steel, while the vertical walls holding the

heat exchanger were sheets of plywood. With a hopper wall angle of approximately 45 degrees from the horizontal, a rat hole quickly developed. A new hopper section was installed that had a wall angle of approximately 70 degrees from the horizontal, but a rat hole still quickly formed.

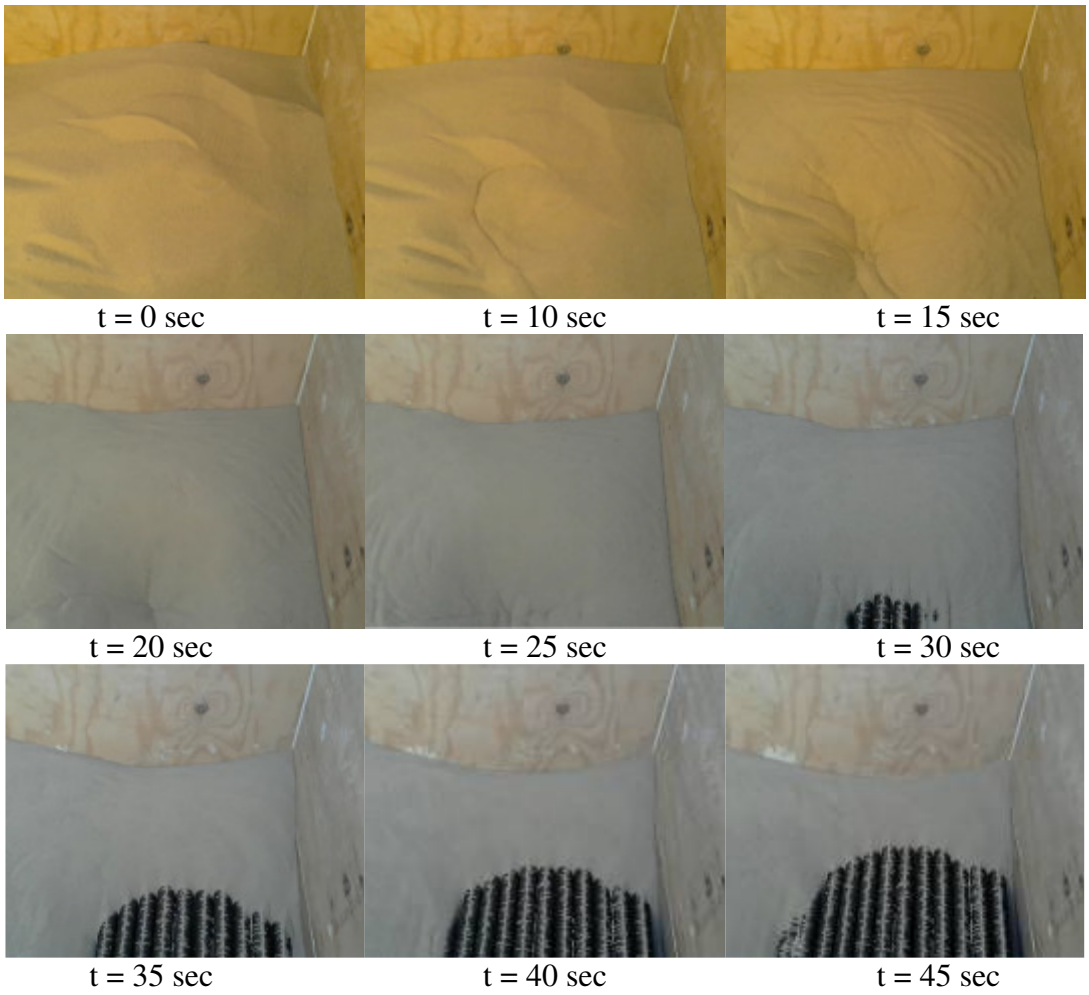

Figure 2 – Series of still shots taken from a movie with the full sized hopper (70 degree version) with heat exchanger inserted, clearly showing funnel flow. Camera was a consumer grade webcam being recorded on a laptop. Change in color is due to software trying to correct exposure as darker areas of frame come into view.

Due to the size and expense of running this experiment at scale, it was decided that lab scale experiments would be conducted to investigate the flow characteristics of this particular hopper set up.

Another previous project, the so-called Sand Shifter, used a rotating pipe with internal baffles arranged in such a way as to scoop sand from the bottom of the pipe, elevate it, and dump it onto an internal heat exchanger. However, constructing lab scale models of this device was not a trivial task. Thus, it was desired to investigate the possibilities of using computer simulation to study flow patterns, as the geometric modeling was potentially much easier done with computer software than with traditional fabrication methods.

This investigation compares the results of lab scale flow tests with tests simulated in a computer using the discrete element method. Using different hopper geometries and wall surface characteristics, mass flow rates and general qualitative flow descriptions of glass beads are recorded. The same hopper and particulate geometries are then modeled on a computer. Then, using combinations of published and experimentally obtained values for material properties, the same flows are simulated using the discrete element method. This data is compared with the data obtained through lab scale flow testing to determine the validity of the simulated data.

This thesis is organized in the following manner. Chapter 2 presents a brief review of the fundamentals of granular hopper flows, the discrete element method, and modeling particulate collisions using the discrete element method. Chapter 3 describes the experimental apparatus and procedure used to measure the mass flow rate of small glass marbles from two different hopper configurations. Chapter 4 describes the general

approach used to simulate the lab scale flow tests on the computer using the discrete element method, and briefly summarizes the two different software packages used. Chapter 5 presents the data obtained from the flow tests and computer simulations, and discusses the similarities and differences in the results. Finally, Chapter 6 gives some final conclusions and hints at opportunities for further refinement of this study in particular, and the future use of the discrete element method in general.

Chapter 2

Background

This chapter provides some of the theoretical background behind this investigation. This background includes theory of granular flows in hoppers as well as an introduction into the fundamentals of the discrete element method and the methods used to model the contact between particles.

2.1 - Granular Flows in Hoppers

Bins, silos, hoppers, and chutes are all widely used in the storage and distribution of granular materials. In general, bins and silos refer to the vertical portion of the storage area and are often used interchangeably. Hoppers are often used to describe the bottom of the bin, whether it be a sloped conical shape or simply a flat plate with a hole in it for discharge. Chute refers to material distribution structures that use gravity to transport material, as opposed to powered means such as conveyor belts (Marinelli, 2005). Understanding the behavior of granular material in a hopper not only aids in designing to obtain the correct flow (of more interest here), but also ensure that the hopper is properly designed to withstand the expected loads and stresses placed upon it during operation.

In very broad terms, flow from hoppers occurs in two modes: mass flow and funnel flow. Mass flow describes a flow pattern in which all of the solid material in a

hopper is in motion during discharge – a so called “first in, first out” flow pattern (Jenike, 1968).

Funnel flow occurs when an internal flow channel, or “rat hole,” develops through the solid material. This flow pattern is described as “first in, last out,” as the material in the top of a hopper flow out through the rat hole before the material along the sides or bottom of the hopper (Jenike, 1968). Figure 3 shows a schematic of each of these flow patterns.

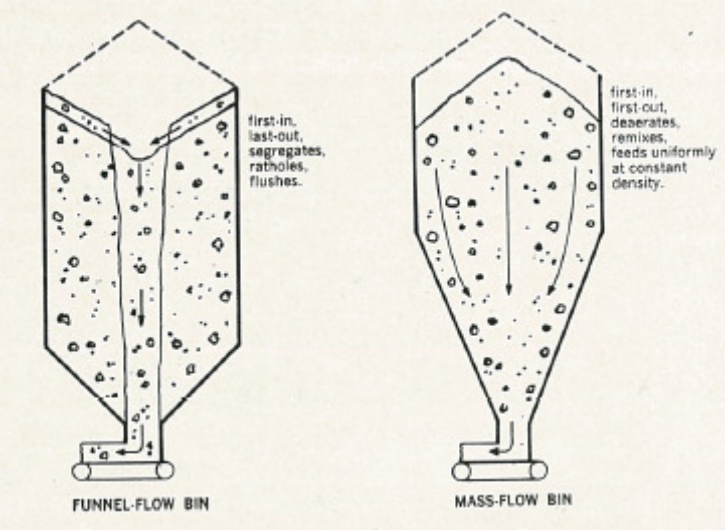

Figure 3 – The two principle types of flow from bins. From Jenike (1968).

Determining where the transition from mass to funnel flow occurs is often of great importance to the hopper designer or process engineer. However, owing to the difficulty of obtaining concise and explicit equations describing granular flow, empirical

models are often used (Jenike, 1954). In some cases, small scale test hoppers can be constructed and tested, provided they have geometric and (sometimes) dynamic and kinematic similarity. In other cases, such as the modeling of feeders, vibrations, or other moving parts, or when anisotripic granular materials are used, full scale hoppers need to be constructed (Carson et al., 2008).

The design of a hopper for a given flow regime depends on several parameters. A frequently used parameter in the design of granular hoppers is the internal friction angle of a material, φ. It is defined as the maximum amount of shear stress τ a granular material can withstand for a given normal stress σ before it begins to shear (ignoring cohesion) (Wu and Sun, 2008),

$$\tan \varphi = \frac{\tau}{\sigma} \qquad (1).$$

Determining the internal friction angle of a material can be done using a shear tester, of which there are several varieties. A common one is the Jenike shear tester, which consists of a base, ring, and lid (see figure 4). The base and ring are filled with a sample of the material to be tested, and then a vertical force is applied to the lid. Finally, a horizontal shearing force is also applied to the lid, and the applied forces divided by the cross sectional area of the shear tester gives the resultant stresses. Those stresses can be plotted on a Mohr's circle, allowing the angle of internal friction (called the yield locus by some authors) to be easily found (Schwedes, 2003). Figure 5 shows the resulting stress plot. The dashed line represents the effective angle of internal friction (or effective yield locus) of the material, and represents the inner friction of the material at steady state flow

(Schwedes, 2003). Other shear testers, such as a biaxial tester or Schulze ring tester produce similar data and have their own advantages and drawbacks (Schwedes, 2003).

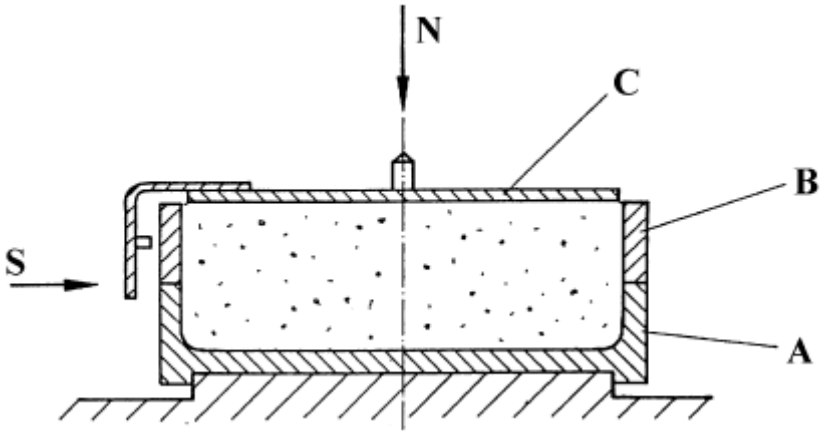

Figure 4 – Schematic of a Jenike shear cell. The cell is filled with granular material, a compressive force N is applied until the material consolidates, and then a shear force S is applied until the material fails. A: base, B: ring, C: lid. From Schwedes (2003).

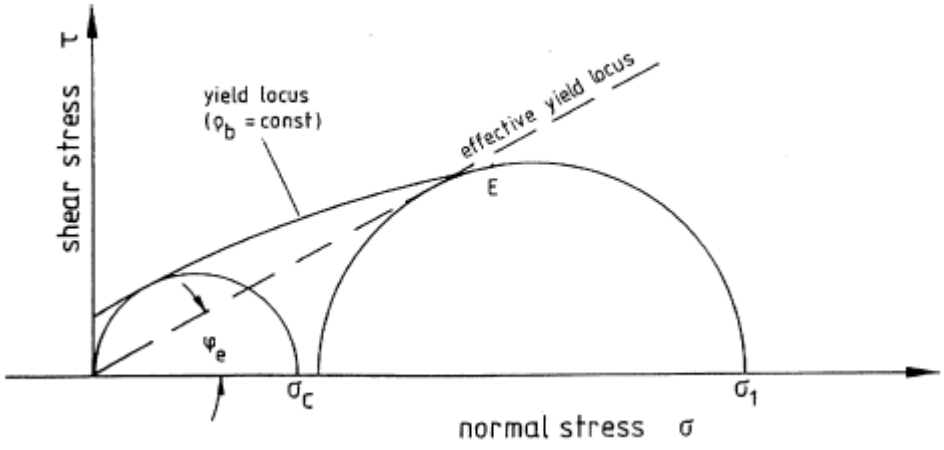

Figure 5 – Plot of shear stress versus normal stress obtained from a Jenike shear tester. From Schwedes (2003).

Another important parameter in designing hoppers for a particular flow regime is the wall friction angle. It is essentially a measure of the friction between the granular material and the wall of the hopper. It can also be measured in a Jenike shear tester or other similar device by placing a sample of the hopper wall material underneath a sample of the granular material and applying similar vertical and horizontal forces to the apparatus (Schwedes, 2003).

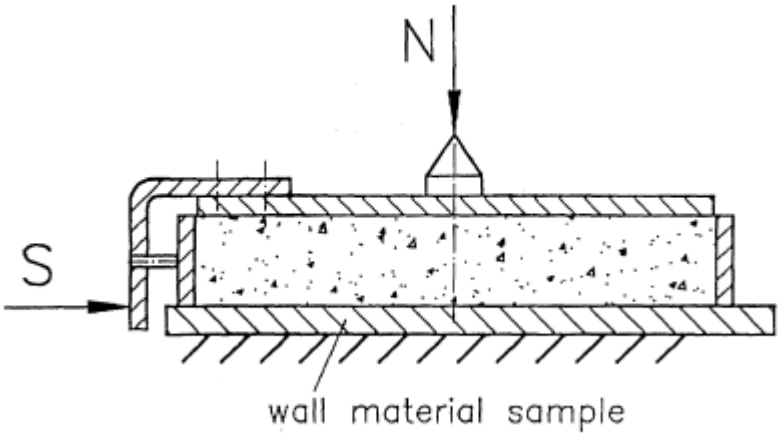

Figure 6 – Determining the wall friction with a Jenike shear tester. From Schwedes (2003).

After calculating the appropriate wall normal and shear stresses, the angle of wall friction can be found in an identical fashion to the internal friction angle, namely

$$\tan \varphi_w = \frac{\tau_w}{\sigma_w} \qquad (2).$$

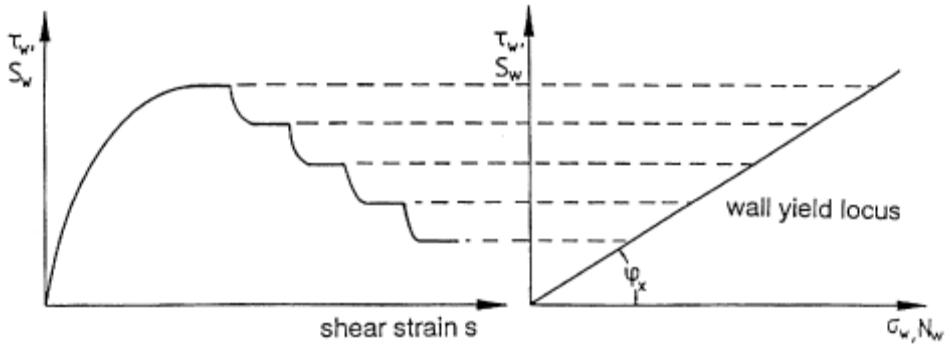

Figure 7 – Determination of wall yield locus and wall friction angle from shear test measurements. From Schwedes (2003).

One of the primary motivations for determining these friction angles is to create flow regime maps for a given hopper discharge configuration. These maps plot the bounding curves for mass flow for a given internal friction angle, wall friction angle, and angle the hopper wall itself makes with the vertical. Figure 8 shows example plots.

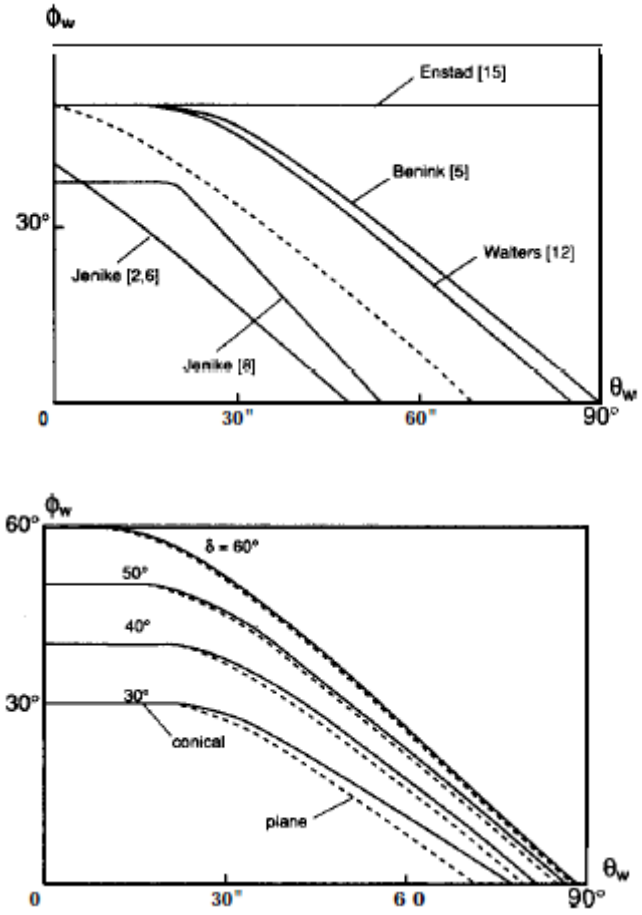

Figure 8 – Plots of mass flow bounding curves. The horizontal axis is the hopper wall angle, the vertical axis is the wall friction angle, and the individual curves correspond to a particular internal friction angle. Mass flow occurs underneath the curves. Top – flow curves by several authors. Bottom – flow curves by Walters and Clauge, showing differences in internal friction angle and hopper geometry. From Drescher (1992).

The design curves of Jenike are widely used in hopper design (Roberts, 2005). They are generated by solving the equations of radial stress in an axi-symmetric or conical hopper (Jenike and Shield, 1959, Jenike, 1964). For those hoppers, the bounds between mass and funnel flow are given by (Roberts, 2005)

$$\alpha = \frac{\pi}{2} - \frac{1}{2}\cos^{-1}\left(\frac{1-\sin\delta}{2\sin\delta}\right) - \beta \tag{3a}$$

$$\beta = \frac{1}{2}\left[\varphi + \sin^{-1}\left(\frac{\sin\varphi}{\sin\delta}\right)\right] \tag{3b}$$

where α is the hopper half angle, δ is the internal friction angle, and φ is the wall friction angle.

Figure 8 points out several important facts that should be taken into consideration during hopper design. First, as seen from the bottom part of figure 8, it can clearly be seen that increasing the internal friction angle make mass flow easier to achieve, as increasing the angle increases the area under the curve. Table gives some examples of internal friction angles for various materials.

Table 1 – Friction angles for various materials. In general, smaller, more uniform granular materials have a smaller angle of internal friction than larger, coarser materials. From Baker (1914).

Ref. No.	Kind of Material.	Tangent of Angle of Internal Friction.	Approximate Corresponding:		Authority.
			Angle.	Slope.	
1	Coal, shingle, ballast, etc.	1.423	54°	0.7 to 1	B. Baker
2	Bank sand	1.423	54°	0.7 to 1	Goodrich
3	Riprap	1.097	48°	0.9 to 1	Goodrich
4	Earth	1.097	48°	0.9 to 1	B. Baker
5	Sand, 100-up	0.895	42°	1.1 to 1	Goodrich
6	Clay	0.895	42°	1.1 to 1	B. Baker
7	Sand, 50–100	0.750	37°	1.3 to 1	Goodrich
8	Earth	0.750	37°	1.3 to 1	Steel
9	Bank sand	0.750	37°	1.3 to 1	Wilson
10	Sand, 50–100	0.549	29°	1.8 to 1	Goodrich
11	Bank sand	0.549	29°	1.8 to 1	Goodrich
12	Clay	0.474	25°	2.1 to 1	Goodrich
13	Cinders	0.474	25°	2.1 to 1	Goodrich
14	Gravel, ½-inch	0.474	25°	2.1 to 1	Goodrich
15	Gravel, ¼-inch	0.350	19°	2.9 to 1	Goodrich
16	Bank sand	0.350	19°	2.9 to 1	Goodrich
17	Sand, 30–50	0.258	14°	3.9 to 1	Goodrich
18	Sand, 20–30	0.179	10°	5.6 to 1	Goodrich

Second, also as seen from the bottom part of figure 8, the hopper geometry itself plays a role in determining the flow regime. The two hopper geometries mentioned here are the conical and plane (or wedge) hopper. These two geometries have been widely studied in hopper design. Figure 9 gives some example bounding curves for the two different hopper geometries.

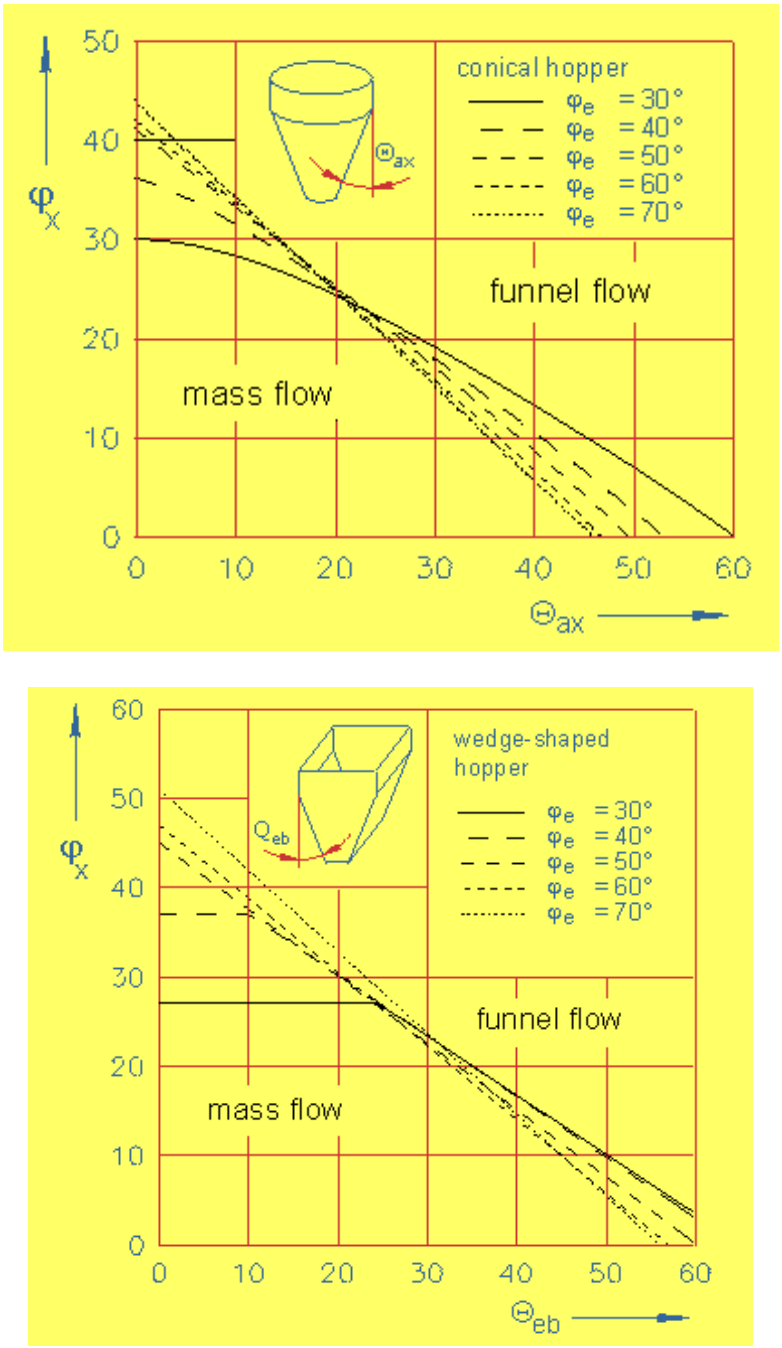

Figure 9 – Design diagrams for conical (top) and wedge (bottom) shaped hoppers. The vertical axis shows wall friction angle, the horizontal axis show hopper angle from the vertical, and the different lines correspond to different internal friction angles. From Schultze (2011).

In general, wedge shaped hoppers can have shallower sidewall angles and still achieve mass flow when compared to conical hoppers (Schultze, 2011). This means that, for a given volume of material, a wedge shaped hopper can be shorter than a conical hopper. However, a wedge shaped hopper may still be more expensive to build than a conical hopper, and the large outlet may require large or specialized unloading equipment (Marinelli, 2005).

Figure 10 shows some variations in hopper design. In general, the wedge based variants b-d will allow for the shallowest sides for mass flow, while the square outlet variants e and f will require the steepest sides.

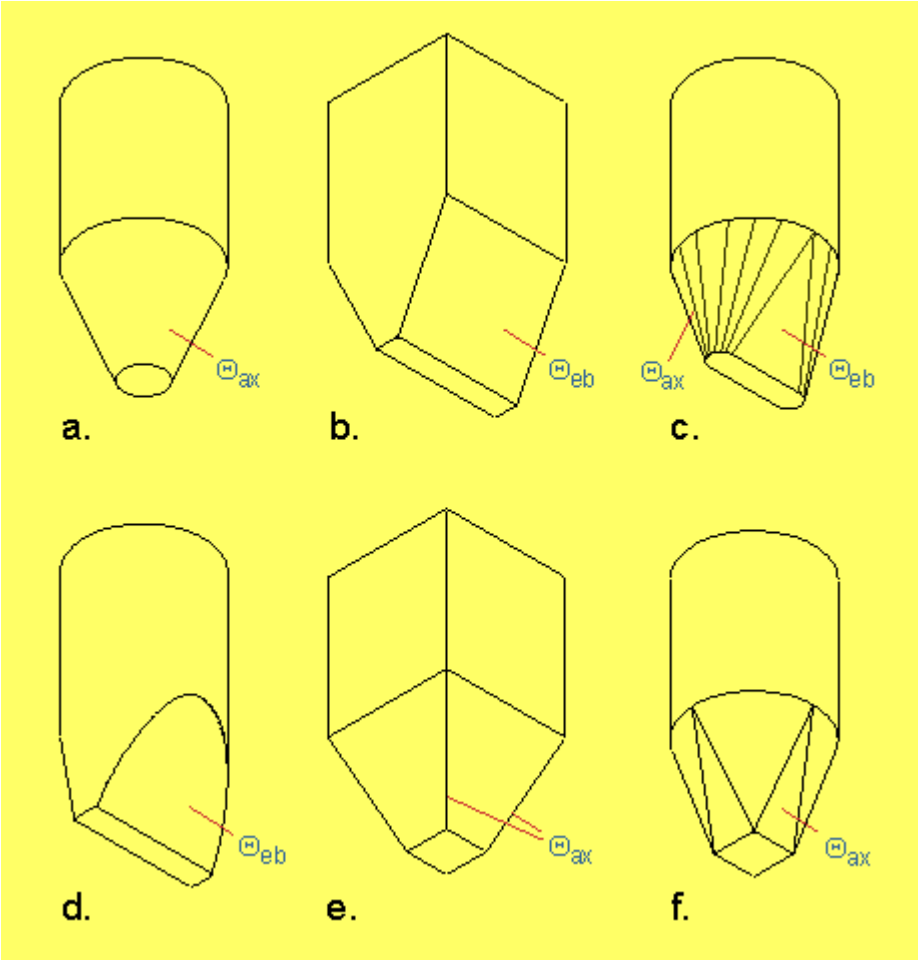

Figure 10 – Some Variations in hopper design. a. conical. b. wedge. c. transitional conical-to-wedge. d. chisel. e. pyramid. f. transitional conical-to-square. The indicated angles correspond to the location where the hopper angle should be measured to predict mass or funnel flow. From Schultze (2011).

It should be noted that the transition from mass to funnel flow might not be sudden. Marinelli and Carson (1992) note that for a conical hopper, there will be a region of uncertain flow near the transition. In this region, small variations in materials and angles can produce either mass or funnel flow, and can even lead to oscillating flows.

Marinelli and Carson also (1992) suggest that a wedge hopper design chart does not need a region of uncertainty near the flow transition area, stating that wedge hoppers are more forgiving of variations of material property and geometry. However, the results of Nguyen et al. (1980) for flows from wedge hoppers indicate that there will still be a region of uncertainty surrounding the transition zone from mass to funnel flow. Thus, if mass flow is desired, a conservative design which is well left of the bounding curve for a given material should be used.

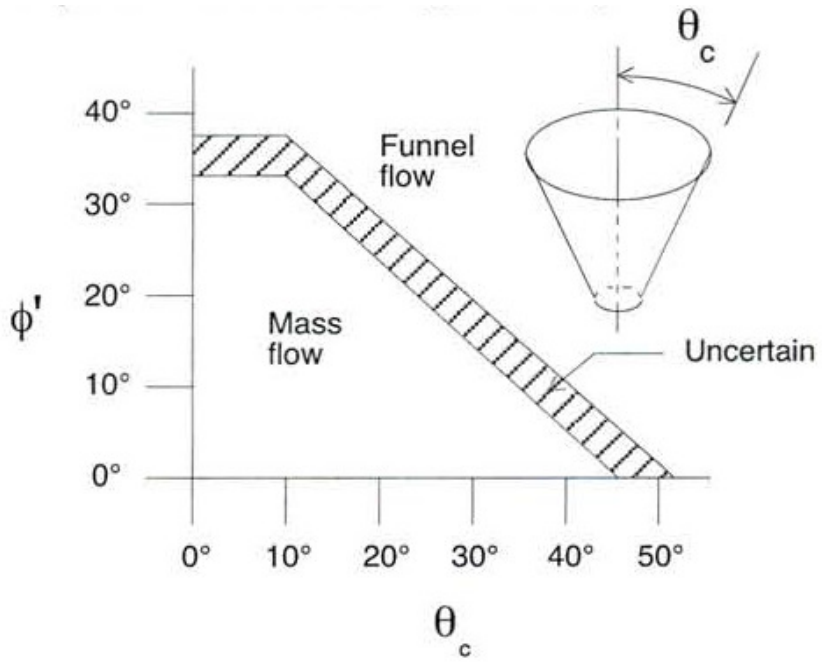

Figure 11 – Design chart for a conical hopper, showing region of uncertainty. A hopper operating in this region can develop a hybrid type of flow, or may rapidly switch between the two flow regimes. From Marinelli and Carson (1992).

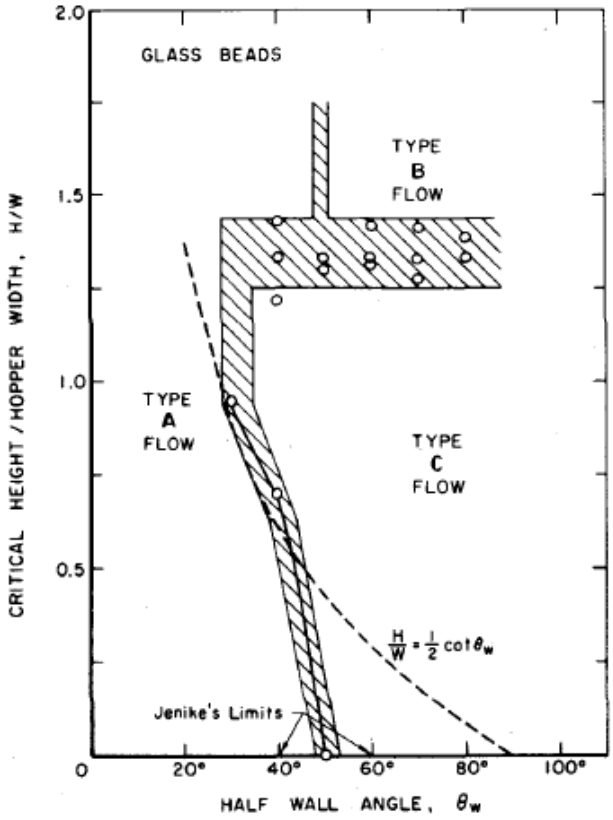

Figure 12 – Plot of height of material in hopper / hopper width versus hopper wall half angle for glass beads in a wedge hopper. The hatched area corresponds to uncertainties in the transition boundary from mass flow ("Type A") and funnel flow (" Type B" and "Type C"). The dashed line indicates flow transition for a hopper without a bin. This chart indicates that not only can the flow regime change as material drains out of a hopper (from A to C back to A), but that the addition of a vertical bin above the hopper can increase the likelihood of funnel flow. From Nguyen (1980).

In summary, this section has reviewed some of the existing literature on granular flow in hoppers, including flow regimes, how to obtain and use the pertinent material properties, and hopper design based on those properties. The internal angle of friction of a granular material, angle of wall friction between granular material and the hopper, and the angle of the hopper bottom are the most important factors in determining the flow regime observed in a granular hopper flow. The shape of the hopper was also seen to have an effect on the transition point between mass and funnel flow for a given material. This section forms the basis on which this study uses for its qualitative criteria.

2.2 - Discrete Element Method

The foundations for using the discrete element method to model particulate flows was laid by Cundall and Strack (1979), in which they described a method to track the contact forces and velocities of a number of two-dimensional discs.

In their discrete element analysis, each particle is represented by a disc with a certain mass, radius, and perhaps velocity. If the distance between the centers of two discs is less than the sum of their radii, i.e. if

$$D < R_i + R_j \tag{4}$$

then the discs are considered to be in contact.

In real collisions, two particles in contact will deform slightly. In the discrete element method, this is accounted for by allowing the particles to overlap a small amount.

This length Δn is directly proportional to the relative velocities of the particles v and some time increment Δt,

$$\Delta n = v\,\Delta t \tag{5}.$$

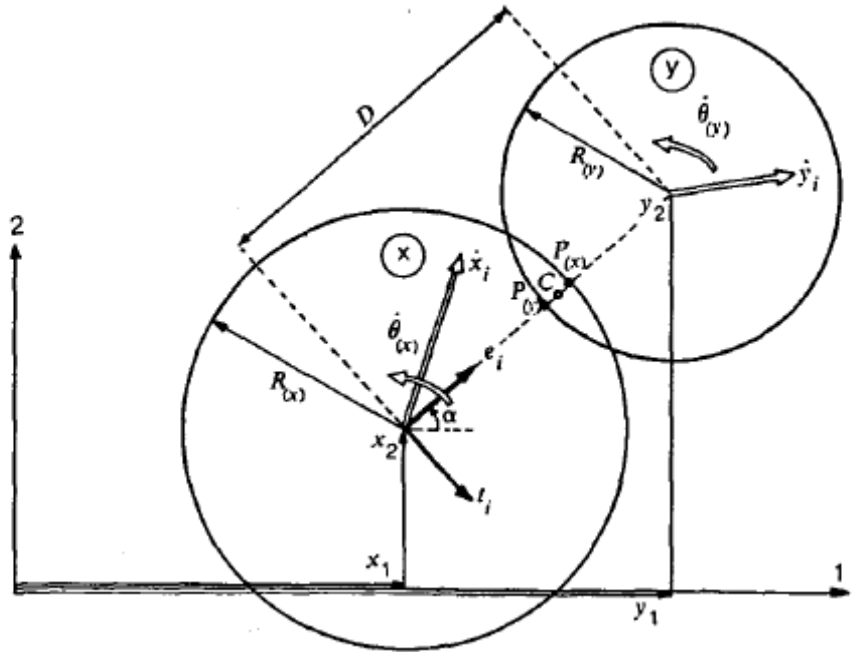

Figure 13 – Two discs in contact. Each particle has its own velocity, mass, and rotation. If the distance D is smaller than the sum of radii of the discs, then they are in contact. From Cundall and Strack (1979).

The force experienced by a particle then becomes

$$F = k\,\Delta n \tag{6}$$

where k represents the material stiffness. Then, using Newton's second law, the resulting particle acceleration becomes

$$a = \frac{F}{m} \tag{7}$$

where m is the mass of the particle. Then, assuming that the acceleration of a particle remains constant over Δt, the velocity of the particle after the time increment becomes

$$v_{t2} = (\frac{F}{m})\Delta t \tag{8}$$

where the subscript $t2$ represents the fact that this for a future time step. Finally, using this new v_{t2}, a new Δn is calculated, forces are re-calculated, and the process repeats itself for as many time steps as desired. The previous calculations describe collisions in the normal (i.e. parallel to the line connecting the particle centers) direction, but similar calculations are done for forces in the tangent direction using the tangential component of relative particle velocity and the shear stiffness k_t. By doing each of those calculations for every particle in the simulation, the resultant forces are summed up at each time step for every particle, and global position, velocity, and rotation are tracked.

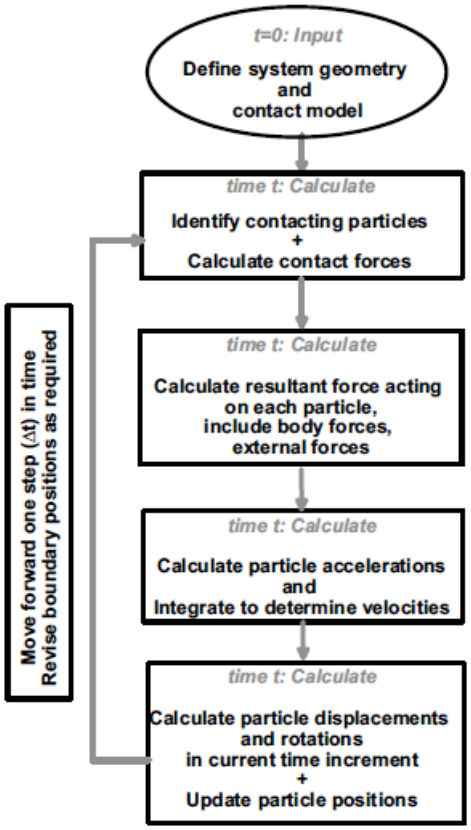

Figure 14 – Schematic of typical discrete element method calculation sequence. From Rao (2012).

In summary, this section has reviewed the theoretical background of simulating granular collisions by using a time-stepped calculation of Newton's equations of motion, known as the discrete element method.

2.3 - Modeling contact

As seen in equation (6, Cundall and Strack treated the normal force between particles as a simple linear spring. To model tangential force, they added a Coulomb-type friction incorporating interparticle friction and cohesion, giving the shear force the form

$$F_s = \min \begin{cases} k_s \Delta n \\ \tan \phi_\mu + c \end{cases} \tag{9}$$

where k_s is the shear stiffness, φ_μ is the smaller of the interparticle friction angles between the two discs and c is the smaller of the cohesions. Additionally, they modeling damping in both the normal and tangential directions using simple linear damping coefficients, giving the equations of motion the form

$$ma = \sum [F + D] - C\,v \tag{10a}$$

$$D = D_n + D_s = c_n\,n + c_s\,s \tag{10b}$$

$$c_i = \beta\,k_i \tag{10c}$$

$$C = \alpha\,m \tag{10d}$$

$$I\ddot{\theta} = \sum M - C^*\dot{\theta} \tag{11a}$$

$$C^* = \alpha I \tag{11b}$$

where D is the contact damping force, c is the contact damping coefficient, n and s are the relative particle velocities in the normal and tangential direction respectively, C is the global velocity damping coefficient, C^* is global rotational damping coefficient, and α and β are proportionality constants. Thus, D acts as a viscous dashpot between particles, while C and C^* act as dashpots between particles and ground. Therefore, Cundall and Strack model damping as a series of linear springs and dashpots. This simple and intuitive model is often called the linear model (Di Renzo, 2004).

Walton and Braun (1986) use a similar model, except that their damping is displacement based, rather than velocity based as with Cundall and Strack (Di Renzo, 2004). Walter and Braun model normal interparcticle forces as two separate springs that operate during loading and unloading separately as

$$F_n = \begin{cases} K_1 n, \text{loading} \\ K_2 (n - n_o), \text{unloading} \end{cases} \tag{12}$$

where n_o is the relative displacement distance where the force curve drops to zero.

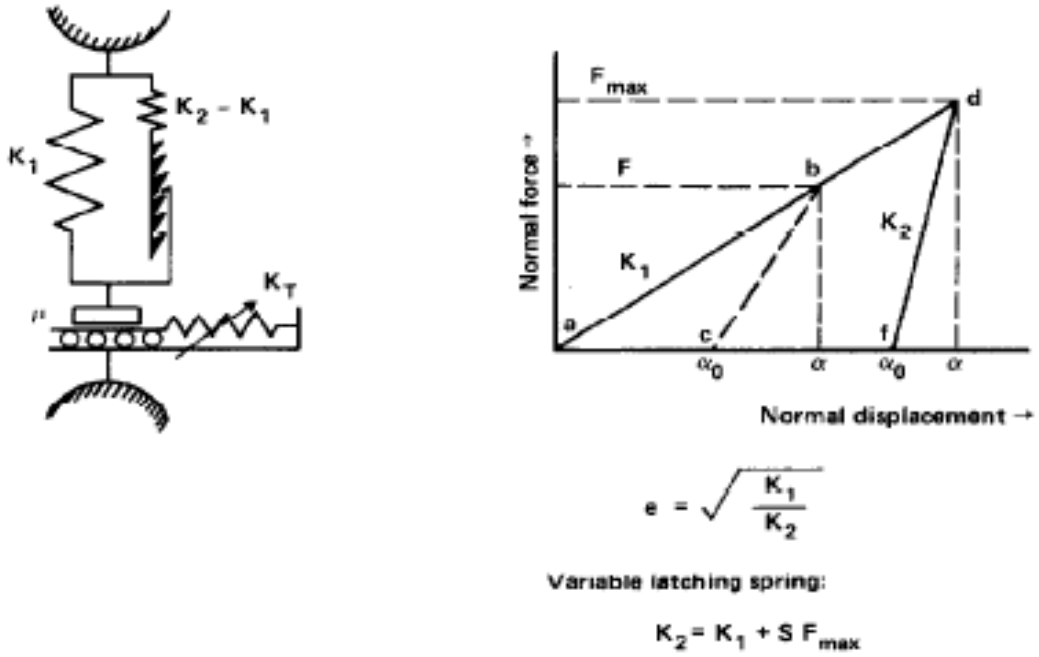

Figure 15 – Schematic showing partially latched spring model and corresponding force deflection curve used to describe inelastic normal direction forces between two colliding discs. From Walton and Braun (1986).

As seen in figure 15 force in the normal direction exhibits position dependent hysteresis described by a ratcheting action. Loading is initiated along line *ab* with slope K_1. If the loading stops at point *b*, unloading will be along line *bc*. Reloading from point *c* follows the path *cbd* until some maximum normal force is reached at point *d*, at which point unloading takes place along the path *dfca*.

Walton and Braun also employ two different models for the coefficient of restitution. In one model, the coefficient is taken as a constant, and all unloading lines (i.e. *bc* and *df*) have the same slope, K_2, and the coefficient of restitution, e, is given by

$$e = \left(\frac{K_1}{K_2}\right)^{1/2} \tag{13}.$$

In the other model, K_2 is a linear function of the maximum force achieved before unloading,

$$K_2 = K_1 + SF_{\max} \tag{14}.$$

Using this model, the coefficient of restitution becomes

$$e = (\omega_0 (Sv_0 + \omega_0))^{1/2} \tag{15}$$

where

$$\omega_0 = \left(\frac{2K_1}{m}\right)^{1/2} \tag{16}$$

and m is the mass of the particles involved in the collision. Figure 16 shows a plot of the coefficient of restitution plotted by equation (15 as well as results obtained from collision tests between brass and lead shot, showing reasonable agreement between experimental data and a model using a variable coefficient of restitution.

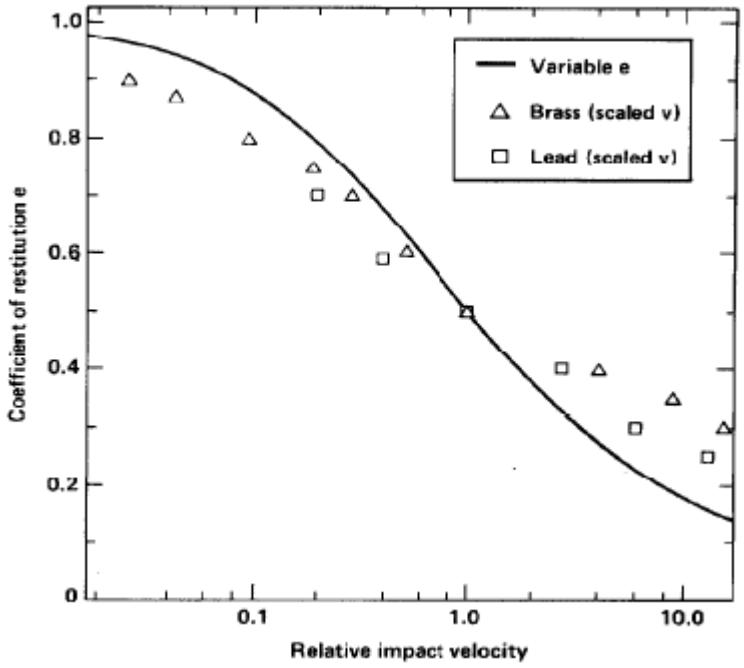

Figure 16 – Coefficient of restitution given by equation (15 and by impact tests between brass and lead shot. The velocity has been nondimensionalized so that $v = 1$ corresponds to $e = 1/2$. From Walton and Braun (1986).

Another widely used contact model is the so called Hertz-Mindlin model. It uses the work of Hertz (1881) to model contact in the normal direction, and the work of Mindlin and Deresiewicz (1953) to model contact in tangential directions. Beginning with the simplest case of a varying normal force and zero tangential force, Mindlin and Deresiewicz, by developing a set of incremental rules used to calculate the states of loading, describe the contact of two particles under various forms of normal and tangential stress.

In the simplest case of a varying normal force and zero tangential force (i.e., a collinear collision), the collision between two particles can be described by (Di Renzo, 2004)

$$p_{\max} = \frac{3f_n}{2\pi a^2} \tag{17}$$

$$a = \left(\frac{3R_{eq}}{4E_{eq}} f_n \right)^{1/3} \tag{18}$$

$$\delta_n = \frac{a^2}{R_{eq}} \tag{19}$$

$$f_n = -K_n \, \delta_n^{3/2} \tag{20}$$

$$K_n = \frac{4}{3} E_{eq} \sqrt{R_{eq}} \tag{21}$$

where p_{max} is the maximum pressure, a is the radius of the contact area, δ_n is the normal displacement, f_n is the normal force, K_n is the normal stiffness, and R_{eq} and E_{eq} are the equivalent radius and elastic modulus of two colliding spheres, given by

$$\frac{1}{R_{eq}} = \frac{1}{R_i} + \frac{1}{R_j} \tag{22}$$

$$\frac{1}{E_{eq}} = \frac{1 - v_i^2}{E_i} + \frac{1 - v_j^2}{E_j} \tag{23}$$

where v is Poisson's ratio, and the subscripts i and j refer to the different particles.

The next case considered is when the normal force is constant and the tangential force is allowed to vary. Under these conditions, the above equations remain constant, while an incremental approach is used to find the tangential force and displacement. The tangential force f_t is calculated using the previous force f_{t0} and the change in tangential displacement through an incremental tangential stiffness K_t as

$$f_t = f_{t0} + K_t (\delta_t - \delta_{t0}) \tag{24}.$$

When the normal displacement is held constant, and a tangential displacement is applied for the first time, the tangential stiffness can be calculated based on the normal displacement as

$$K_t = K_{t0}\left(1 - \frac{\frac{2}{3} K_{t0}\, \delta_t}{\mu\, f_n}\right)^{1/2} \tag{25}$$

where μ is the friction coefficient. The initial stiffness constant K_{t0} is a given by

$$K_{t0} = 8G_{eq}\left(R_{eq}\, \delta_n\right)^{1/2} \tag{26}$$

where G_{eq} is defined as

$$\frac{1}{G_{eq}} = \frac{1 - v_i}{G_i} + \frac{1 - v_j}{G_j} \tag{27}.$$

Equation (25 can also be cast in the form

$$K_t = K_{t0}\left(1 - \frac{f_t}{\mu\, f_n}\right)^{1/3} \tag{28}.$$

The limit on the maximum tangential stress is governed by Coulomb's law of friction

$$|t| \le \mu |p| \tag{29}$$

which is satisfied throughout the contact area. A condition called micro-slip occurs when equation (29 is satisfied with the equal sign. When this slip area covers the entire contact area, the condition of gross sliding occurs, and the law of friction states that

$$|f_t| = \mu |f_n| \tag{30}.$$

The above equations are used when a tangential force is first applied. The loading path is different during the unloading phase, showing a hysteretic behavior. At the onset of unloading, a "turning point" occurs, and equation (24 is used once again to calculate the tangential force, with the tangential stiffness now taking the form

$$K_t = K_{t0}\left(1 - \frac{f_t^{TP} - f_t}{2\mu f_n}\right)^{1/3} \tag{31}.$$

Following successive steps along this unloading path, it can be shown that, at a tangential displacement of $-\delta_t^{TP}$, the stress and deformation distributions are the same as in the case of first loading, but with the opposite sign, and the previous positive loading history has no more influence.

Now consider the point where reloading occurs. At this second turning point, the tangential stiffness will be

$$K_t = K_{t0}\left(1 - \frac{f_t - f_t^{TTP}}{2\mu f_n}\right)^{1/3} \tag{32}.$$

An illustration of the typical first loading-unloading-reloading path is shown in figure 17, along with the corresponding values for the tangential stiffness in each case.

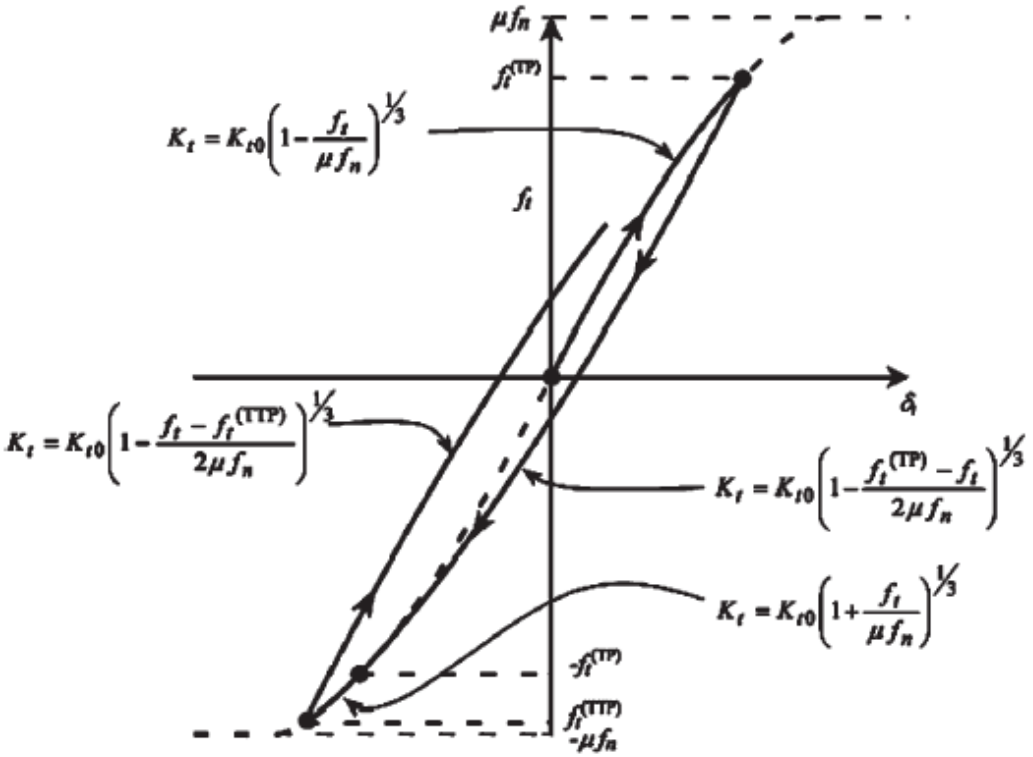

Figure 17 – Tangential stiffness constants for different branches of the f_t-δ_t curve in the case of constant normal displacement. From Di Renzo (2004).

Moving now to the case where both the normal and tangential displacements are allowed to vary, Mindlin and Deresiewicz (1953) proposed a set of rules that can be used in an incremental manner to find the required forces and displacements. Those rules are (stated much more succinctly by Di Renzo (2004)):

> "1. Circular contact area and pressure distribution [are] prescribed by Hertz Theory.
>
> 2. The change in normal displacement and the change in tangential displacement are not interconnected, i.e. the problem cab be solved by superposition of the two separate effects.

3. Each incremental step starts from a simple loading history condition... The simple loading history condition is defined as the condition in which the state of the system (δ_n, δ_t, f_n, f_t), independently of the loading path, can also be reached through a constant normal displacement (corresponding to δ_n) tangential loading curve f_t-δ_t (through a first loading/unloading/reloading path).

4. No torsion or rolling is taken into account."

Using these rules, various states of changing normal and tangential displacements can be analyzed.

As an example, take the case of increasing normal and tangential displacement (Di Renzo, 2004). In this case, loading proceeds from an initial point **0** (see figure 18). Using rule 1, the normal displacement and force can be calculated using the Hertz theory. Then, using the equations and f_t-δ_t curves previously presented, the tangential problem can be solved. The system can be described in terms of the initial normal and tangential displacements, δ_{n0} and δ_{t0} respectively.

Now the normal displacement is increased to some higher value, δ_{n1}. Due to rule 3 and the definition of simple loading history, it can be shown that the tangential force-displacement relationship is a linear one up to state **1** with slope K_{t0} (equation (26)), evaluated at δ_{n1}. It is also noted that the change in the tangential force is equal to $\mu \Delta f_n$. Putting this in terms of displacements, the minimum change in tangential displacement required to preserve the simple loading condition in rule 3 can be evaluated as

$$\left|\Delta\delta_t\right| \geq \Delta\delta_t^{SL} = \frac{\mu\left|f_n\right|}{K_{t0}} \tag{33}.$$

Thus, point **1** in figure 18 can be described by

$$f_{t1} = f_{t0} + \mu \Delta f_n \tag{34}$$

$$\delta_{t1} = \delta_{t0} + \Delta \delta_t^{SL} \tag{35}.$$

Therefore, any actual change in tangential displacement δ_t that is less than δ_{t1} will not meet the condition of simple loading history for subsequent steps required in rule 3, and the corresponding tangential force is found by

$$f_t = f_{t0} + K_{t01}(\delta_t - \delta_{t0}) \tag{36}.$$

However, if the actual tangential displacement δ_t is greater than δ_{t1}, simple loading history is maintained, and a two step calculation is required. First, state **1** is reached using equations 33 and 34. Then, state **2** is reached along the new constant normal displacement curve, and the final tangential force f_{t2} is found by

$$f_{t2} = f_{t1} + K_{t12}(\delta_{t2} - \delta_{t1}) \tag{37}$$

$$K_{t12} = K_{t01}\left(1 - \frac{f_{t1}}{\mu f_{n1}}\right)^{1/3} \tag{38}.$$

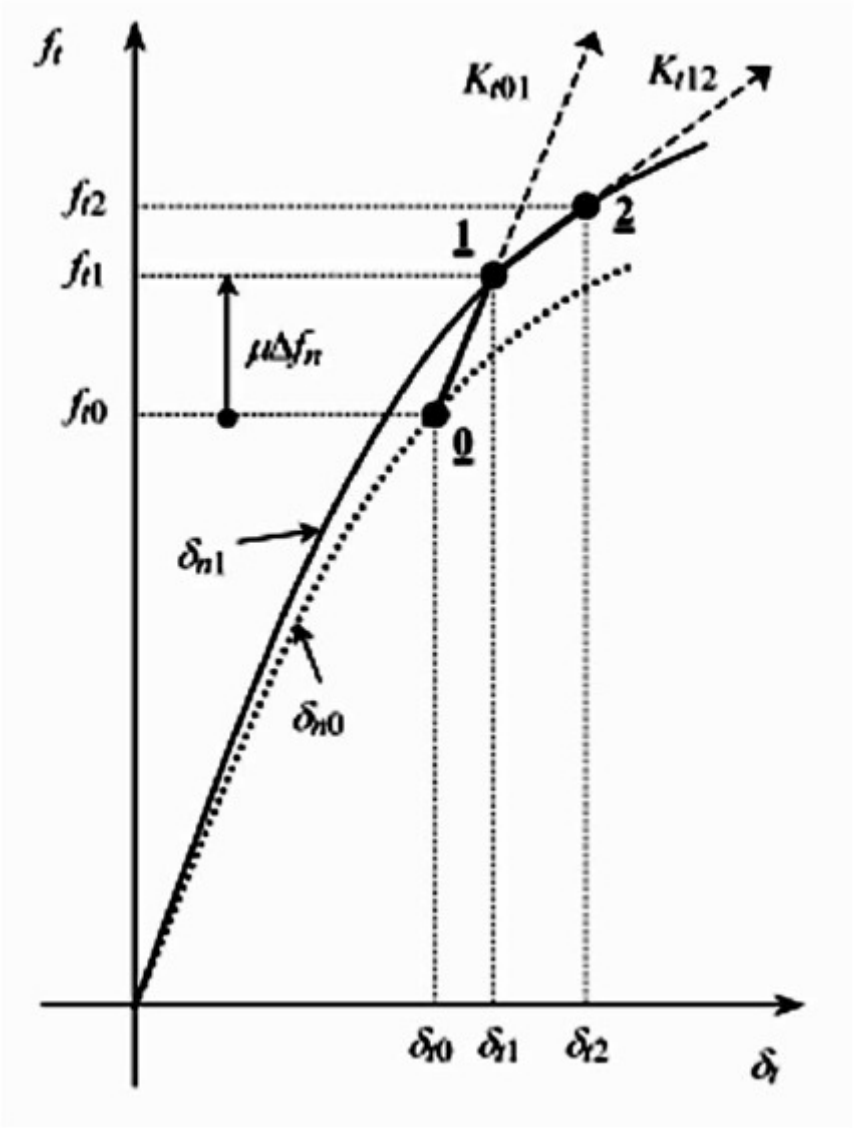

Figure 18 – Tangential loading path for the case of increasing normal and tangential displacement. The calculation of the total transformation **0**-**2** is broken into two constant normal displacement steps **0-1** and **1-2**. The f_t-δ_t curves correspond to the previous (dotted line) and the new (solid line) constant normal displacement. From Di Renzo (2004).

Now the case of both normal and tangential displacement decreasing is considered. In general, any case where the normal displacement is decreasing will always satisfy the simple loading history requirement since the final state will always lay on the new constant normal displacement curve (see figure 19).

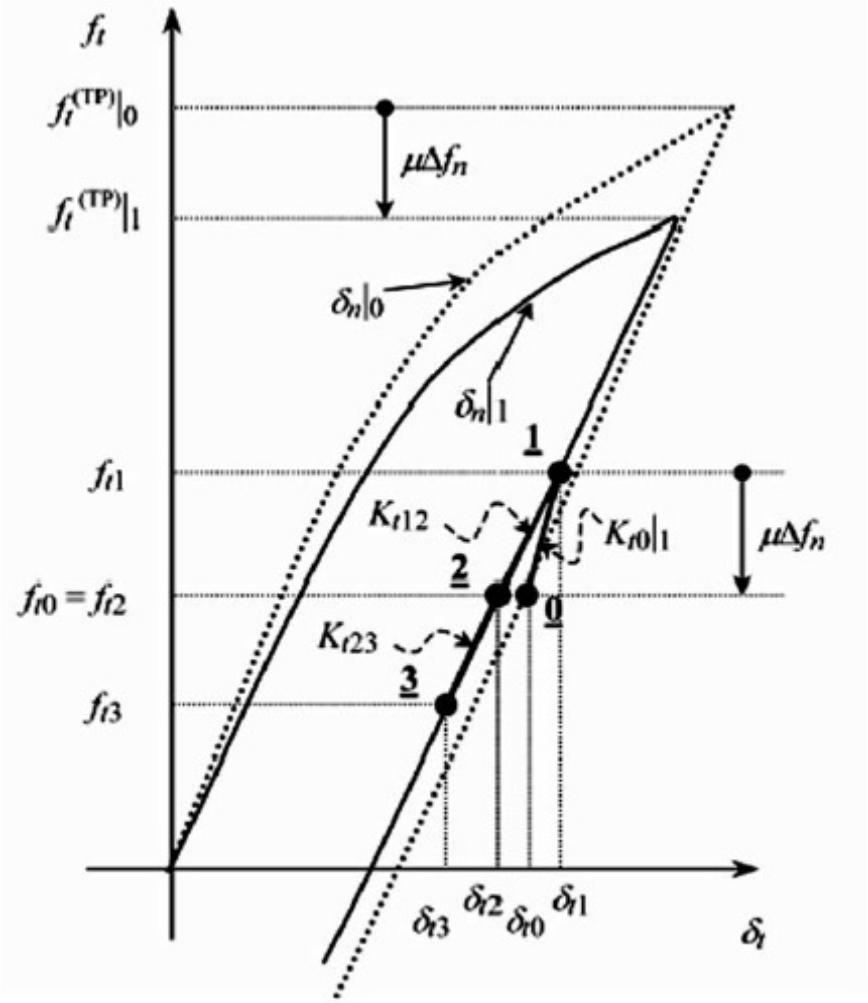

Figure 19 – Tangential loading path for the case of decreasing normal and tangential displacement. Once again, the transformation **0-3** is split into smaller constant normal displacement steps, and the f_t-δ_t curves for the corresponding previous (dotted line) and new (solid line) constant normal displacement are shown. From Di Renzo (2004).

The steps used in calculating the final state **3** from the initial state **0** are essentially identical to those just presented. State **1** is reached by traveling along a straight line of slope K_{t01}, such that the corresponding tangential force initially increases ($\Delta f_n < 0$) as

$$f_{t1} = f_{t0} - \mu \Delta f_n \tag{39}.$$

Decreasing the tangential displacement from this point will lead to a state which is lower on the displacement curve (state **3** in figure 19). To reach state **3** from state **1**, one can calculate

$$f_{t3} = f_{t1} + K_{t13}\left(\delta_{t3} - \delta_{t1}\right) \tag{40}$$

$$K_{t13} = K_{t01}\left(1 - \frac{f_{t1}^{TP} - f_{t1}}{2\mu f_n}\right)^{1/3} \tag{41}$$

$$f_{t1}^{TP} = f_{t0}^{TP} + \mu \Delta f_n \tag{42}$$

where K_{t13} is the stiffness constant used for moving from state **1** to state **3**, and f_{t1}^{TP} is the updated turning point force required because of the change in normal displacement. For better accuracy when dealing with large changes of tangential displacement, an additional intermediate state **2** can be used, such that the tangential force at state **2** is the same as at state **0**, and the additional stiffness constants are calculated in a similar manner.

As previously stated, Mindlin and Deresiewicz ignored the rotation of the discs when calculating the contact forces. However, this assumption is not always realistic. There have been several methods used to describe a torsional or rolling resistance for use in DEM simulations (Ai et al., 2011).

One of the simplest models of rolling resistance is a constant torque model. It applies a constant torque on a particle in a direction which is opposite the relative rotation between two contacting particles. It is given by

$$M_r = -\frac{\omega_{rel}}{|\omega_{rel}|}\mu_r R_r F_n \tag{43}$$

where ω_{rel} is the relative angular velocities of two particles in contact, given by

$$\omega_{rel} = \omega_i - \omega_j \tag{44},$$

R_r is the rotational radius, given by

$$R_r = \frac{r_i r_j}{r_i + r_j} \tag{45},$$

μ_r is the coefficient of rolling friction, and F_n is the normal force. A variation of this model is used by both sets of DEM software, so it is the only model that will be discussed here, but other models include viscous models in which the applied torque is proportional to the relative translational velocity between two particles, and an elastic-plastic spring-dashpot model in which the applied torque is the sum of a spring torque and a viscous damping torque.

In summary, this section has provided a brief review of some of the major methods used in modeling the contact between colliding particles in a DEM simulation, including a linear spring-dashpot model, a displacement based hysteric spring model, the so called Hertz-Mindlin model, and a constant torque model used for calculating rolling resistance in collisions. The linear spring model, Hertz-Mindlin model, and constant torque rolling resistance model form the basis for the simulations described in later sections.

Chapter 3

Lab Scale Experiments

3.1 - Experimental Apparatus

This section serves to describe the various parts of the lab scale apparatus used to record particulate flow data for various geometries and surface conditions. The goals for the lab scale testing were to provide easily recordable and repeatable particulate flow data, and to provide an experiment that was easily replicated in a computer simulation.

Lab scale flow testing was done for two different geometries: a three-dimensional (3D) inverted pyramid hopper and a quasi-3D wedge shaped hopper. The 3D hopper was a scaled down version of the hopper used in the full scale heat exchanger testing, and the quasi-3D hopper was a cross section of the 3D hopper taken at its midpoint.

Each hopper geometry was set up and instrumented in the same way, so it will only be described once here. The hopper was constructed out of thin sheets of brushed carbon steel which was cut and spot welded to make the required geometry. The hopper was supported in a Unistrut® frame which provided easy access to the top of the hopper, hopper valve, and bead collection bin. The hopper was made level by using shims where the hopper was secured to the frame.

Below the hopper, a Keli DEFY100 load cell was fixed between two large aluminum plates which served as the base for the particle collection bin. The load cell was interfaced to an Agilent 34970A/34972A data scanner. Data was recorded by a computer connected to the Agilent data scanner and running Benchlink Data Logger 3

software. Above the hopper, a Casio Exilim camera was mounted on a tripod to record high speed images of the surface of the marbles.

In summary, this section has described the apparatus used to measure the flow of granular material from two different hopper configurations in a lab setting.

Figure 20 – Lab scale hoppers used in flow testing. Left – quasi-3D wedge hopper. Right – 3 dimensional tetragonal hopper.

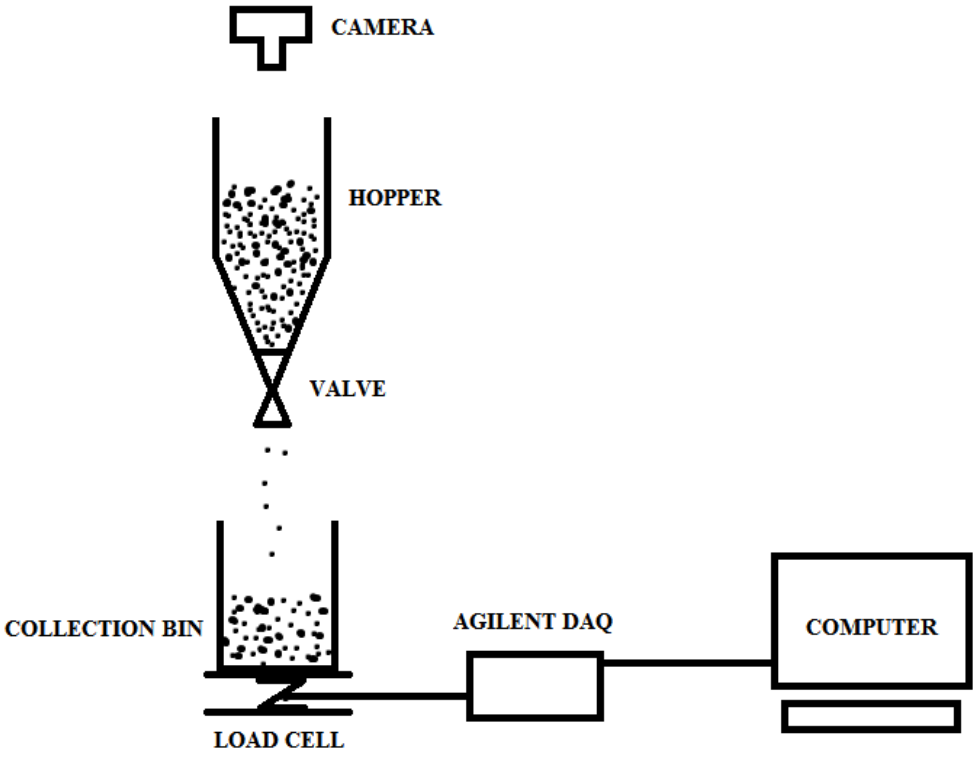

Figure 21 – Schematic of flow measurement apparatus as seen in figure 20.

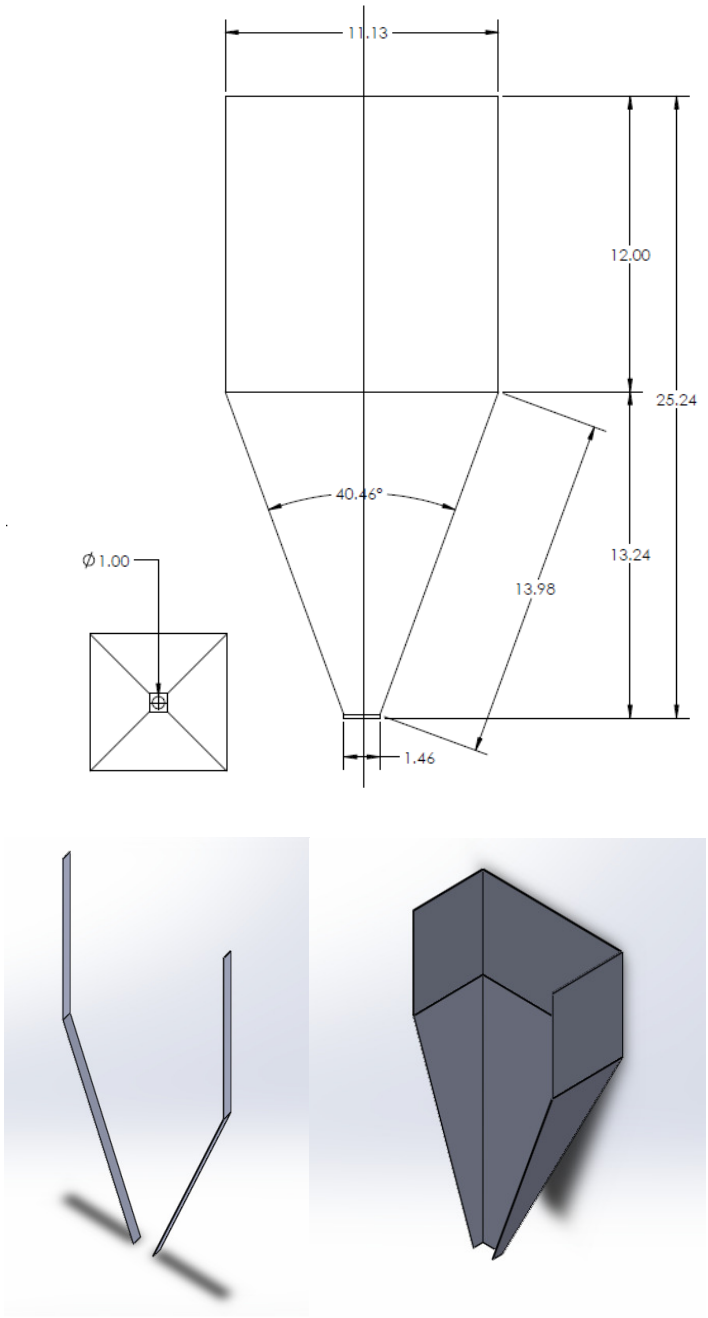

Figure 22 – (top) Drawings used in the construction and modeling of the hoppers. (bottom) AutoCAD models used in the computer simulations. Note that, when testing marbles in the 3 dimensional hopper, the hopper outlet opening was increased to the full size of the square intersection of the sloped sides, as the one inch hole was too small to flow the marbles without bridging.

In summary, this section has described an experimental apparatus that was used to measure the mass flow rate of small glass spheres from two different hopper configurations.

3.2 - Experimental Procedure

This section describes the steps that went into performing lab scale particulate flow testing. . The goals for the lab scale testing were to provide easily recordable and repeatable particulate flow data, and to provide an experiment that was easily replicated in a computer simulation. Data was collected for two different hopper geometries with two different wall conditions each. However, the procedure was identical for each combination.

To ensure accurate correlation between the output of the load cell in mV and the corresponding weight in the particle bin, the load cell was calibrated using the following procedure:

1. Twelve clay bricks were each individually numbered and weighed using an Ohaus GT8000 scale. The weight of each brick was recorded in kg.
2. Starting with an empty base with no bin, the data scanner began recording data at (intervals), which was the output of the load cell in mV.
3. One by one, bricks were placed on the load cell platform. There was a delay of several seconds between bricks to ensure that any vibrations in the base plate or swaying of the growing tower of bricks was minimized. The order in which the bricks were placed on the base plate was recorded.

4. In a similar fashion, bricks were removed from the base plate, waiting several seconds to ensure that system oscillations were minimized. The order in which the bricks were removed was recorded.
5. The output of the load cell in mV was plotted against time which produced a stair stepped plot. This data was compared to the known weight of bricks on the load cell at each step. Using linear interpolation, a calibration equation was generated which was weight in kg on the load cell as a function of load cell output in mV.

To begin an experimental run, glass beads were loaded into the top of a hopper with the valve closed. A Casio Exilim camera was attached to a tripod, positioned above the hopper, and aimed down at the top surface of the beads. A portable spotlight was also aimed into the top of the hopper from above to ensure adequate lighting.

Then, in succession, the camera started recording video, the data logger started scanning, and the hopper valve was opened. The hopper was allowed to drain into the bin until the hopper was totally empty. Then, after a few seconds of settling time, the data logger and camera were stopped.

Because the 3 dimensional hopper shared the same geometry in the lab and in the computer, the mass flow rates can be directly compared. To compare mass flow rates for the quasi 3D hopper, the overall mass flow rate of the lab scale hopper was divided by the ratio of the overall hopper widths to get a consistent mass flow per periodic structure width.

To estimate the values for particle-to-wall and particle-to-particle friction that were used in the computer simulations, a “sled” was constructed using a small piece of

scrap wood and three glass marbles. The marbles were glued to the piece of scrap wood in a triangular pattern. The sled was then placed on the sample surface, which was either a bare piece of the metal used in the hopper construction, the same metal covered in sand paper, or a smooth piece of pyrex glass. The surface was initially horizontal. The inclination between the surface and the horizontal was gradually increased until the sled began to slide. It can be shown that the value for static friction between the glass beads and the respective surface is the tangent of the angle formed between the surface and the horizontal as

$$\mu = \tan \varphi \qquad (46).$$

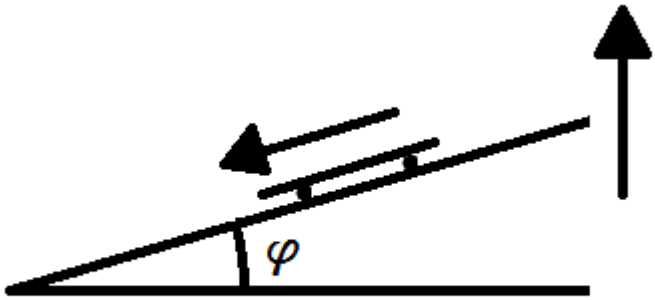

Figure 23 – (top) Picture of method used to measure friction values. (bottom) Schematic of method used to determine friction values. The surface angle was increased until the sled began to slip. This angle was used to find the coefficient of static friction used in DEM simulations.

This is similar to the method used by Li et al. (2005) to determine the sliding friction coefficients between the various particles and various surfaces used in their study. Several authors (for example, Ketterhagen et al. (2009)) have suggested that there may be relationship between the values of sliding friction (commonly used in DEM simulations) and friction angles (commonly used in hopper design charts) of various material interfaces. Figure 24 gives examples of such relationships for rotating and non-rotating particles.

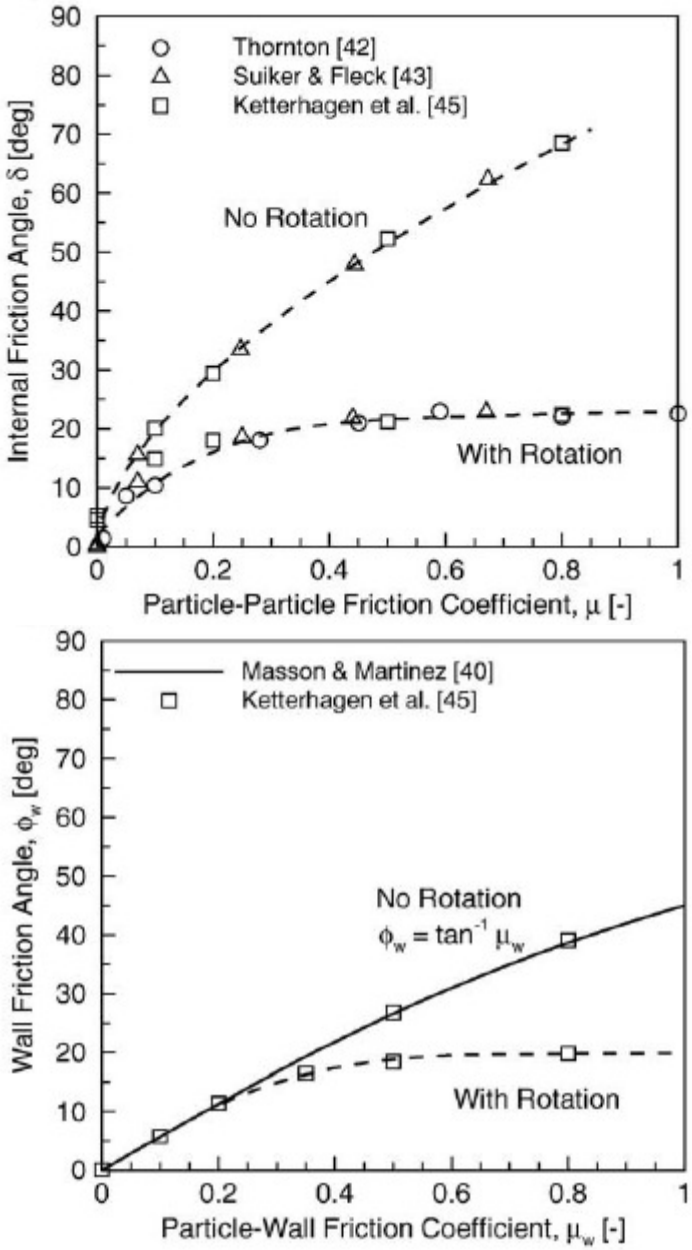

Figure 24 – Some correlations between friction coefficients used in DEM simulations and friction angles used in hopper design charts. From Ketterhagen (2009).

Additionally, several authors (for example, Zhou et al. (2009) and Ghazavi et al. (2008)) have suggested that there may be relationships between the angle of repose of particles – the angle formed between the surface and the horizontal of a pile of unconfined particles – and various frictional values. Such a relationship would have the advantage that the angle of repose for a material is fairly easy to measure. However, the observed angle of repose of the particles used in this study was zero (i.e. they would not form a pile in an unconfined state). Thus, in DEM simulations, rolling friction values were set to either be identical to the measured sliding friction values, or were set to low values that were of the same magnitude as used in previous studies (for example, see Zhou et al. (2002)).

Two variations of this friction test were performed with sleds of different weights used. The follwing table summarizes the friction results obtained and used for simulations when applicable. In each case, several readings were taken. Only the average is reported here.

Table 2 – Sliding friction coefficients for experimental sled on various surfaces.

Surface material	Sled mass (g)	
	756	101
Glass	.320	.122
Steel	.236	.364
Sandpaper	.669	.799

In summary, this section has described an experimental apparatus consisting of a hopper suspended above a load cell which, by taking load cell measurements at specified intervals, can be used to calculated the mass flow rate of small glass beads from the hopper to a collection bin. It also describes how a small sled consisting of three small

glass beads glued to a wooden platform and allowed to slide along various surfaces at various angles of inclination were used to calculate the coefficients of sliding friction used in later computer simulations.

Chapter 4

Computer Simulations

4.1 – General Simulation Procedure

DEM simulations were performed using two software packages: EDEM® by DEM Solutions Ltd., and LIGGGHTS, an open source DEM software.

In general, a simulated run was performed using the following steps:

1. A computer model of the hopper geometry was built using Solidworks® software, and then imported into the DEM software. The fully 3 dimensional hopper was created with the drawings seen in figure 22. The quasi-3D hopper was created from a cross section of that drawing at the minimum hopper angle from vertical – i.e. a cross section orthogonal between faces and through the centerline of the full model, as opposed to a section between opposite corners. To determine the thickness of the quasi-3D hopper, Ketterhagen et al. (2009) suggests that a hopper depth of greater than 2.1 particle diameters is sufficient to ensure that the discharge is not effected by the narrow geometry. Therefore, the hopper was made 15.98 mm in depth to go beyond the 2.1 particle diameters.
2. Various material properties are defined for both the hopper walls and the particles themselves. These included density, Young's modulus, Poisson's ratio, and the various values of sliding and rolling friction for the different material-to-material interactions. Friction values were obtained by the measurement previously described. In the absence of experimental data, other material parameters were taken from Rao (2012) to enable direct comparisons with previous work.

3. The particles were defined in the DEM software. They were given the same material properties as those used in the lab scale flow experiments (namely, they were given the same properties as 7 mm spherical glass beads).
4. The overall simulation environment was defined. This included the definition of vector that defined gravity, as well as the extent of the simulation "box." The hopper geometry was inserted into the simulation environment at this time.
5. Starting with an empty hopper, the DEM software would generate a stream of particles that would fall into and thus fill up the hopper geometry. This was done by either specifying how fast particles were to be generated and then specifying how many particles in total to generate, or by specifying the same values by mass. The quasi-3d simulations used 5340 particles, while the full 3 dimensional simulations used 53400 particles. After the specified number of particles was generated, particle creation was stopped, and the particles were briefly allowed to settle.
6. Starting with the previously saved state, the hopper valve was "opened," allowing the particles to drain out. The DEM software tracked the total mass of particles in the simulation environment. Thus, as particles left the overall simulation box, the total mass in the simulation decreased. This was used to calculate the mass flow rate.

This general procedure was used for both simulation platforms, with only minor adjustments being used to accommodate the specific input requirements of each software package.

Both EDEM and LIGGGHTS calculate the forces between colliding particles in the following way (DEM Solutions, 2013; Kloss et al. 2012). In general, forces between particles are calculated by the formula

$$F = F_n + F_t \tag{47}$$

where the subscripts *n* and *t* denote the normal and tangential components respectively.

Each component has a stiffness and damping component. When using the Hertzian contact model, the normal stiffness components are given by equations (20) and (21), while the normal damping term is given by

$$F_n^d = -2\sqrt{\frac{5}{6}}\,\beta\sqrt{S_n\, m_{eq}}\, v_n \tag{48}$$

$$S_n = 2\, Y_{eq}\sqrt{R_{eq}\,\delta_n} \tag{49}$$

$$\beta = \frac{\ln(e)}{\sqrt{\ln^2(e)+\pi^2}} \tag{50}$$

where v_n is the relative normal velocity between the particles, e is the coefficient of restitution between the particles, Y_{eq}, R_{eq}, and G_{eq} are calculated as before, and m_{eq} is found by

$$\frac{1}{m_{eq}} = \frac{1}{m_i} + \frac{1}{m_j} \tag{51}.$$

The tangential damping term is given by

$$F_t^d = -2\sqrt{\frac{5}{6}}\,\beta\sqrt{S_t\, m_{eq}}\, v_t \tag{52}$$

$$S_t = 8\, G_{eq}\sqrt{R_{eq}\,\delta_n} \tag{53}.$$

When using the linear spring contact model (called the Hooke model by LIGGGHTS), the normal force is calculated by

$$F_n = k_n \delta_n + c_n \dot{\delta}_n \tag{54}$$

where k and c represent the stiffness and damping components of the spring and dashpot model used by Cundall and Strack (1979), and $\dot{\delta}_n$ is the normal overlap velocity.

The spring stiffness k is found by

$$k_n = \frac{16}{15}\sqrt{R_{eq}}\, E_{eq}\left(\frac{15 m_{eq} V^2}{16\sqrt{R_{eq}}\, E_{eq}}\right)^{1/5} \tag{55}$$

where V is the typical impact velocity of particles in a simulation. Unless otherwise noted, this study assumed a characteristic velocity of 1 m/s.

The coefficient of damping c is found by

$$c_n = \sqrt{\frac{4 m_{eq} k}{1+\left(\frac{\pi}{\ln e}\right)^2}} \tag{56}.$$

The tangential force can be found in a way similar to equation (9), but adding a tangential damping component and ignoring cohesion

$$F_t = \min\begin{cases} k_t \delta_t + c_t \dot{\delta}_t \\ \mu F_n \end{cases} \tag{57}.$$

Both EDEM and LIGGGHTS treat the values of k_t and c_t as equal to the values of k_n and c_n when using the linear spring model.

In the basic Hertz-Mindlin contact model as employed by EDEM, rolling friction is accounted for on a per particle basis as

$$\tau_i = -\mu_r F_n R_i \omega_i \tag{58}$$

where μ_i is the coefficient of rolling friction and ω_i is the angular velocity of the particle at the contact point. LIGGGHTS the model described by Ai et al. (2011) and employs equations (43) - (45),. EDEM can also employ a rolling friction model based on the relative rotational velocities, but it was not used in this study.

As seen from the above equations, EDEM and LIGGGHTS requires material properties in addition to friction values in order to run a simulation. Those required properties are the Young's modulus, Poisson's ratio, particle mass, and the coefficient of restitution between materials. EDEM used the shear modulus of a material in place of the Young's modulus, which are related by

$$G = \frac{E}{2(1+\nu)} \tag{59}.$$

The following table summarizes the values of those parameters used in the DEM simulations.

Table 3 – Values of material properties used in DEM simulations. Values are from Rao (2012).

Parameter	Value	
	Glass	Steel
Poisson Ratio	0.25	0.3
Shear Modulus (GPa)	44	79.3
Young's Modulus (Gpa)	110	206
Density (kg/m^3)	2500	8000
Coefficient of Restitution		
Glass-Glass	0.9	
Glass-Steel	0.5	

In summary, this section has described the basic procedure for setting up and running a DEM simulation in a computer environment. It has also described the methods used by the computer programs to describe the interactions between particles, and detailed some of the global material properties used in those simulations.

4.2 - EDEM

EDEM is a discrete element modeling software produced by DEM solutions (DEM 2013). The standard EDEM suite comes with 3 core components: the creator, simulator, and analyst. These allow complete pre-processing, simulation, and post-processing in one package. EDEM runs on both Windows and Linux platforms, and can run on shared memory parallel computing platforms. It can also be used with EDEM Application Programming Interface (API), a C++ based scripting language, and can be coupled with both external field data and computational fluid dynamics (CFD) software.

EDEM uses a graphical user interface (GUI) to input data and output results. This makes using it much more intuitive for a user migrating over from typical Windows based applications. However, due to licensing costs, all of the simulations performed in this study using EDEM were done on a single personal computer running Windows 7.

The fact that EDEM was using only a single CPU resulted in simulations that would last several days just for the draining of the quasi-3D hopper. Therefore, no full 3 dimensional hopper simulations were performed with EDEM.

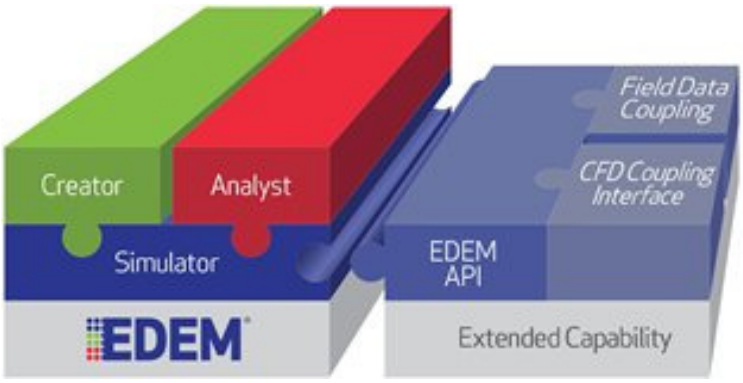

Figure 25 – Graphical representatoin of core EDEM modules and extended capabilities. From DEM Solutions (2013).

Due to the limited amount of software license time available for work with EDEM, most of the simulations were aimed at being extensions of the work done by Rao (2012). Some of the extra variables used in these simulations include the used of frictionless particles, and the use of particles of with artificially enlarged moments of inertias, almost totally eliminating particle rotation. The effect of particle rotation has been studied by Ketterhagen et al. (2009) and has been shown to have significant effects on granular flow.

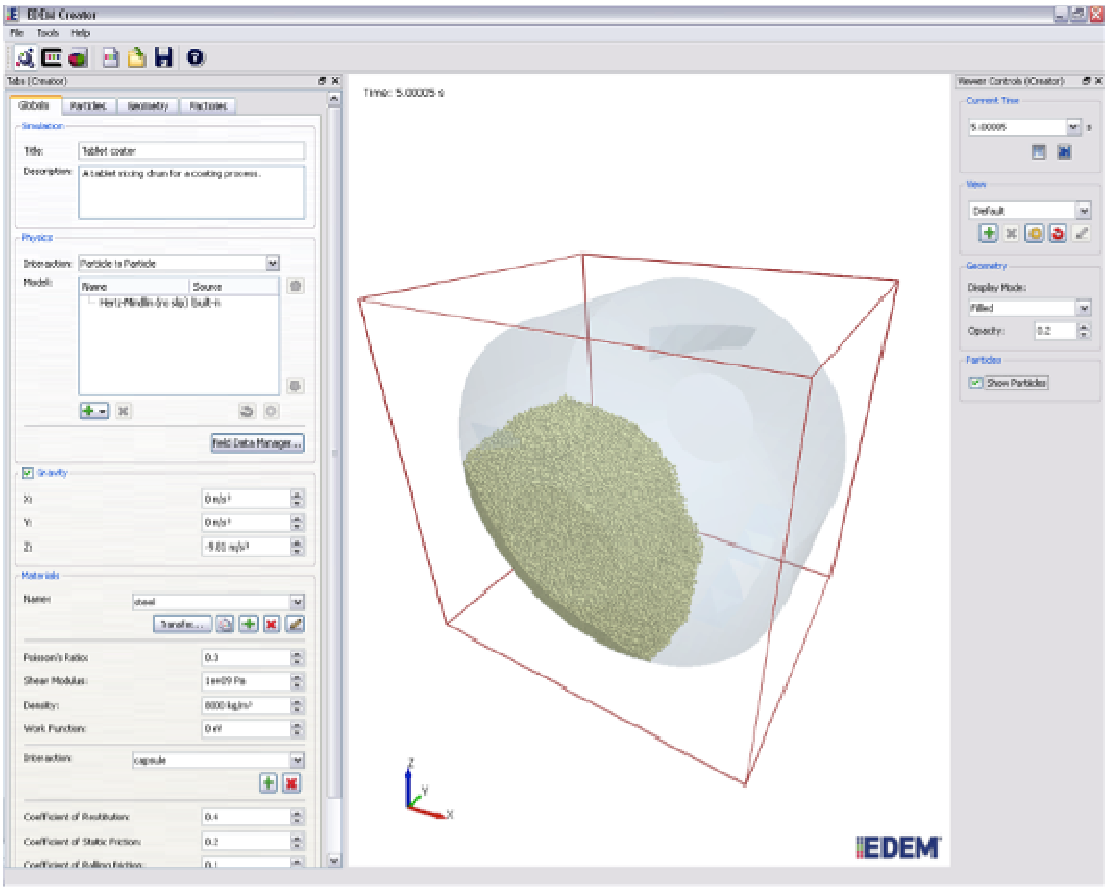

Figure 26 – Typical input screen for the EDEM creator module. From DEM Solutions (2013).

4.3 - LIGGGHTS

LIGGGHTS is an open source DEM code developed by Kloss et al. (2012). LIGGGHTS stands for LAMMPS Improved for General Granular and Granular Heat Transfer Simulations. LAMMPS stands for Large-scale Atomic/Molecular Massively Parellel Simulator. It is a classical molecular dynamics simulator developed by Plimpton (1995).

LIGGGHTS is a Linux based program which uses command line interface (CLI) to input data and output results. It is capable of pre-processing and simulation, but needs to have data output to other programs for true post processing. Its open source architecture enables modification by end users.

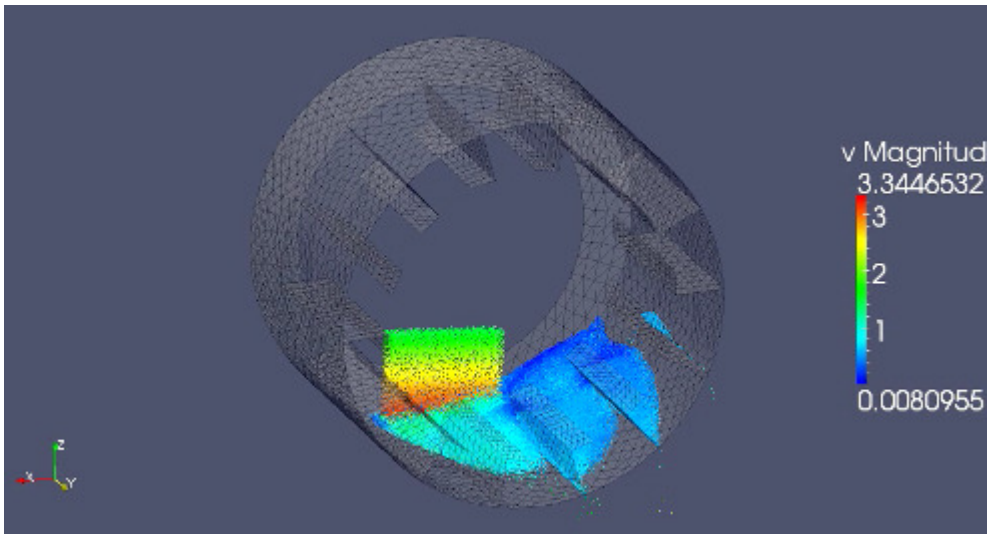

Figure 27 – Example of LIGGGHTS output of a rotating drum dryer. As the particles fall onto the drum, the drum rotates, lifting the particles with the scoops and eventually dumping them out. Post processing, including combined geometry/particle visualization, animation, and coloring were done in PARAVIEW, a separate program. PARAVIEW was not used in this study. From www.liggghts.com (2013).

All of the simulations done with LIGGGHTS were run on Georgia Tech's Partnership for an Advanced Computing Environment (PACE) system. PACE uses a Moab scheduler to run jobs in batch mode on open computer clusters (interactive "real time" jobs can be scheduled as well) (Georgia Tech, 2013). While using LIGGGHTS over multiple processors provided greatly improved simulation times (as did using lower values for Young's modulus; see results section), it did have the drawback of only being able to perform computations when cluster availability allowed.

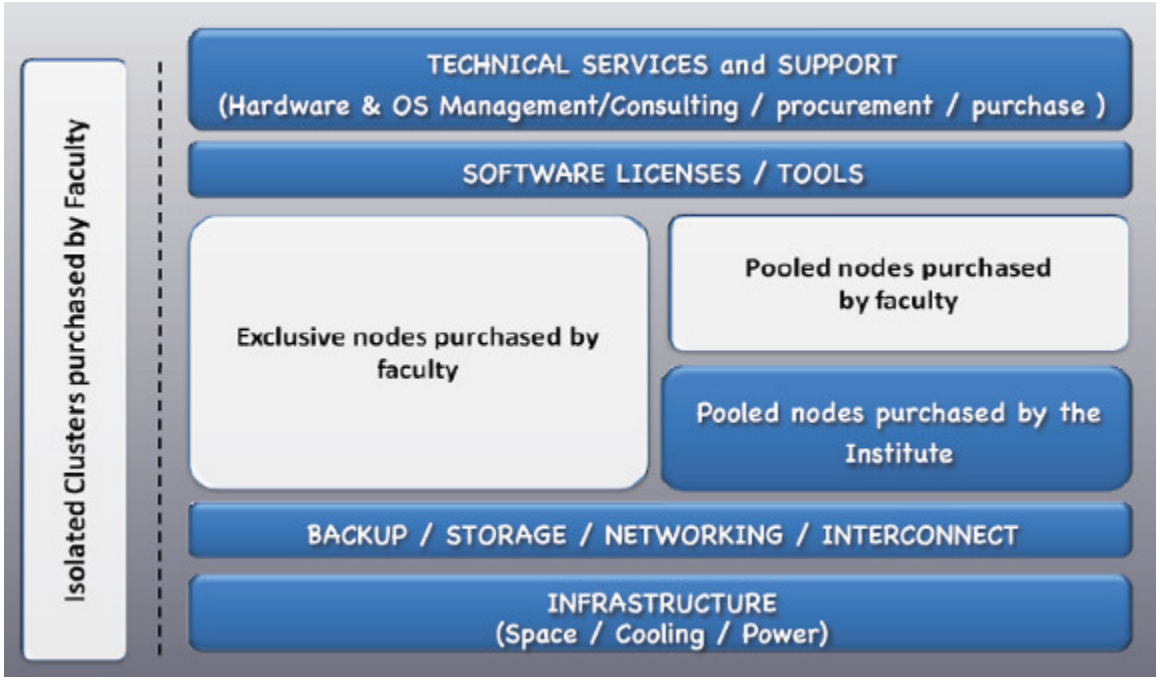

Figure 28 – Graphical representation of PACE structure. Boxes in blue represent Institute dollars, while boxes in grey represent faculty dollars. The isolated clusters box to the left of the dotted line is not supported by PACE. From Georgia Tech (2013).

In summary, this section has reviewed some of the features of EDEM, a commercially available DEM software package, and LIGGGHTS, an open source DEM software package. It also briefly described the use of LIGGGHTS inside The Georgia Institute of Technology's PACE advanced computing network. It has described how a 3 dimensional Solidworks drawing is imported into a computer simulation, and then by using various material and other physical parameters taken from measurements or pertinent literature, DEM simulations are performed. In general, the LIGGGHTS simulations ran faster, but were subject to PACE cluster availability and had a less intuitive interface, while the EDEM simulations, while run on a typical Windows based PC with a GUI interface, were much slower.

Chapter 5

Results and Discussion

5.1 – Quasi-3D hopper

In general, for the quasi-3D hopper, both DEM programs were capable of producing reasonable quantitative and qualitative agreement with the lab scale experiments, as can be seen in the following tables and figures.

Table 4 – Mass flow rates for the lab scale quasi-3D hopper. The bottom row is the average.

Rough walls	Smooth walls
mass flow rate (kg/sec)	mass flow rate (kg/sec)
0.458	0.558
0.455	0.613
0.449	0.567
0.454	**0.579**

The EDEM data suggests that, in general, extremely low friction values can mask other factors that influence granular flows. Simulations that have a "High MOI" comment next to them used particles that had artificially inflated values for the moment of inertia (100000 kg m^2 instead of the nominal value of 2.20 x 10^{-9} kg m^2) in an attempt to prevent the particles from rotating. However, with such low value for both sliding and rolling friction, it is difficult to know how much of an effect the high moment of inertia had.

Table 5 – Mass flow rates for the quasi-3D EDEM simulations – low wall friction.

Linear contact model	Sliding friction		Rolling Friction			
	Particle-Particle	Particle-Wall	Particle-Particle	Particle-Wall	Mass flow rate (kg/sec)	Comments
	0	0.2	0.01	0.01	0.815	
	0	0.2	0.01	0.01	0.819	High MOI
	0	0.5	0.01	0.01	0.815	
	0.1	0.2	0.01	0.01	0.603	High MOI
	0.1	0.2	0.01	0.01	0.606	
	0.12	0.36	0.01	0.01	0.574	
Hertz Contact model	Sliding friction		Rolling Friction			
	Particle-Particle	Particle-Wall	Particle-Particle	Particle-Wall	Mass flow rate (kg/sec)	Comments
	0	0.2	0.01	0.01	0.817	
	0.1	0.5	0.01	0.01	0.593	
	0.1	0.1	0.01	0.01	0.657	High MOI
	0.12	0.36	0.01	0.01	0.571	

Table 6 – Mass flow rates for the quasi-3D EDEM simulations – high wall friction.

Linear contact model	Sliding friction		Rolling Friction			
	Particle-Particle	Particle-Wall	Particle-Particle	Particle-Wall	Mass flow rate (kg/sec)	Comments
	0	0.8	0.01	0.01	0.817	
	0	0.8	0.01	0.01	0.815	High MOI
	0.1	0.8	0.01	0.01	0.592	
	0.1	0.8	0.01	0.01	0.589	High MOI
Hertz Contact model	Sliding friction		Rolling Friction			
	Particle-Particle	Particle-Wall	Particle-Particle	Particle-Wall	Mass flow rate (kg/sec)	Comments
	0	0.8	0.01	0.01	0.814	
	0.01	0.8	0.01	0.01	0.795	
	0.1	0.8	0.01	0.01	0.591	High MOI
	0.12	0.8	0.01	0.01	0.566	
	0.3	0.8	0.01	0.01	0.443	
	0.15	0.8	0.15	0.15	0.334	

Table 7 – Mass flow rates for the 2 dimensional LIGGGHTS simulations.

Hertz	Sliding friction		Rolling Friction		
Rolling resistance on	particle-particle	particle-wall	particle-particle	particle-wall	mass flow rate (kg/sec)
	0.122	0.799	0.122	0.799	0.330
	0.32	0.669	0.32	0.669	0.279
	0.122	0.364	0.122	0.364	0.503
	0.32	0.236	0.32	0.236	0.415
	0.122	0.799	0	0	0.746
	0.32	0.669	0	0	0.549
	0.122	0.364	0	0	0.752
	0.32	0.236	0	0	0.540
Rolling resistance off					
	0.122	0.799	0.122	0.799	0.362
	0.32	0.669	0.32	0.669	0.340
	0.122	0.364	0.122	0.364	0.540
	0.32	0.236	0.32	0.236	0.534
Hooke					
Rolling resistance on					
	0.122	0.799	0.122	0.799	0.318
	0.32	0.669	0.32	0.669	0.277
	0.122	0.364	0.122	0.364	0.482
	0.32	0.236	0.32	0.236	0.412
	0.122	0.799	0	0	0.728
	0.32	0.669	0	0	0.536
	0.122	0.364	0	0	0.731
	0.32	0.236	0	0	0.565
Rolling resistance off					
	0.122	0.799	0.122	0.799	0.352
	0.32	0.669	0.32	0.669	0.333
	0.122	0.364	0.122	0.364	0.527
	0.32	0.236	0.32	0.236	0.515

Table 7 suggests that, in this simulation, the presence or absence of coefficient of rolling friction rather than the presence or absence of a particular rolling friction model has a larger effect on particle motion. This could indicate that, in this simulation, the effect of rolling resistance is small, as particle rotation is expected to only be a major form of motion near the hopper walls. Table 8 provides some direct comparisons between the two different DEM software packages. In general, for the same values of sliding and rolling friction, LIGGGHTS predicts a higher mass flow rate than DEM. This could possibly be explained by the slight difference each software set calculated rolling resistance between particles. It could also be explained by the difference in material stiffness used by each DEM software package. EDEM used the same shear modulus used by Rao (2012) in his work. Essentially, these were realistic values on the order of gigapascals. LIGGGHTS used Young's modulus values that were orders of magnitude lower, as seen in table 8. This was done to speed up simulations. In a DEM model, the critical time step of a simulation is defined as (Cundall and Strack, 1979)

$$t_{crit} = 2\sqrt{\frac{m}{k}} \tag{60}$$

where k is the stiffness from equation (21). The critical timestep is related to the length of time for collisions between two particles, so a time step that is a small fraction of this value is used for the actual simulation. Thus, as the Young's modulus of a material increases, the value of t_{crit} decreases. It has been suggested by Di Renzo (2004) that the velocities of particles are relatively independent of the material stiffness, meaning that velocity trajectory calculations, such as those used for this simple mass flow rate simulation, should be unaffected.

Table 8 – A Comparison of some different simulations between EDEM and LIGGGHTS.

Linear contact model	Sliding friction		Rolling Friction			
	Particle-Particle	Particle-Wall	Particle-Particle	Particle-Wall	Mass flow rate (kg/sec)	Comments
EDEM	0.1	0.8	0.01	0.01	0.592	E~10^{12}
LIGGGHTS	0.1	0.8	0.01	0.01	0.742	E~10^{6}
LIGGGHTS	0.1	0.8	0.01	0.01	0.690	E~10^{7}
Hertz Contact model						
EDEM	0.15	0.8	0.15	0.15	0.334	E~10^{12}
LIGGGHTS	0.15	0.8	0.15	0.15	0.468	E~10^{6}
LIGGGHTS	0.15	0.8	0.15	0.15	0.426	E~10^{7}
EDEM	0.12	0.36	0.01	0.01	0.571	E~10^{12}
LIGGGHTS	0.122	0.364	0.01	0.01	0.719	E~10^{6}
LIGGGHTS	0.122	0.364	0.01	0.01	0.661	E~10^{7}

The Young's modulus was given the orders of magnitude of 10^6 and 10^7 because suggestions from both the EDEM and LIGGGHTS development teams have suggested (by way of their respective online forums) that a Young's modulus on the order of 10^7 is near the smallest one should use when performing such slow speed, mass flow based simulations. Table 8 shows that the mass flow rate predicted by LIGGGHTS begins converging towards the values predicted by EDEM as the values for Young's modulus converge towards each other. It should be noted that this modification can only be made when forces and stresses at the particle level are not important, as those variables depend explicitly on the material stiffness.

Figures 29 and 30 gives a comparison of the mass flow rates form each method in graphical form. In general, the low friction models produced the closest match of mass

flow rates. When rolling friction was turned off or was set to a very low level, both EDEM and LIGGGHTS produced mass flow rates that are uniformly higher than measured in the lab.

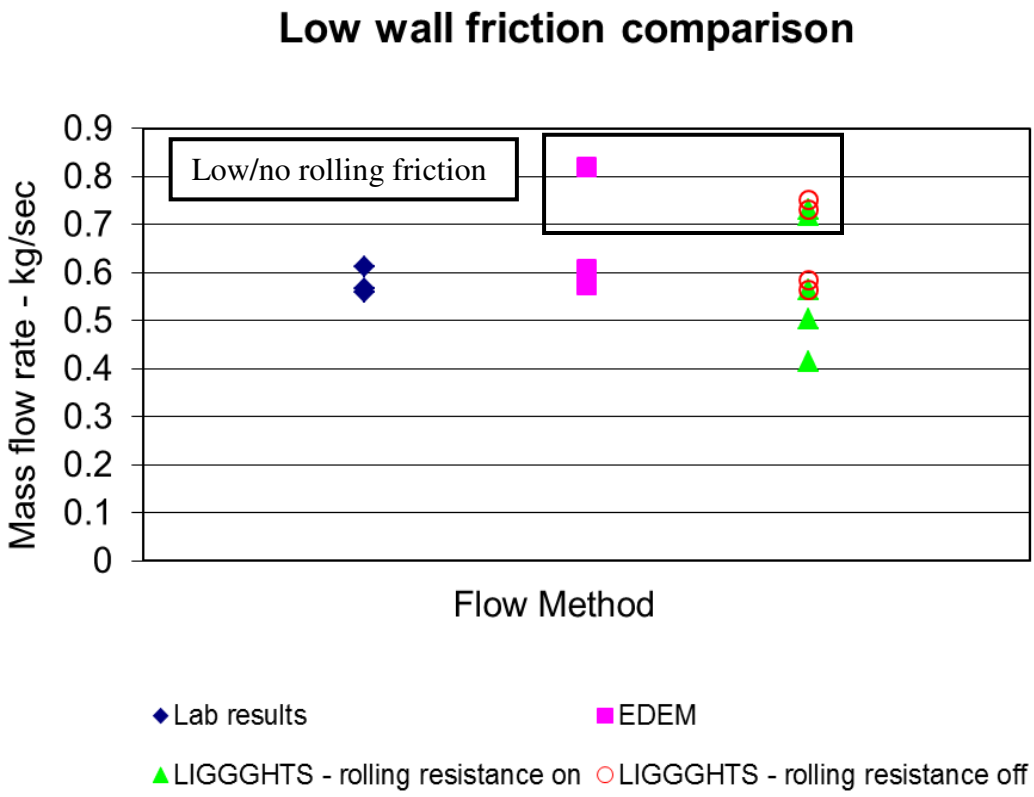

Figure 29 – A graphical comparison between the three methods for the smooth walled hopper.

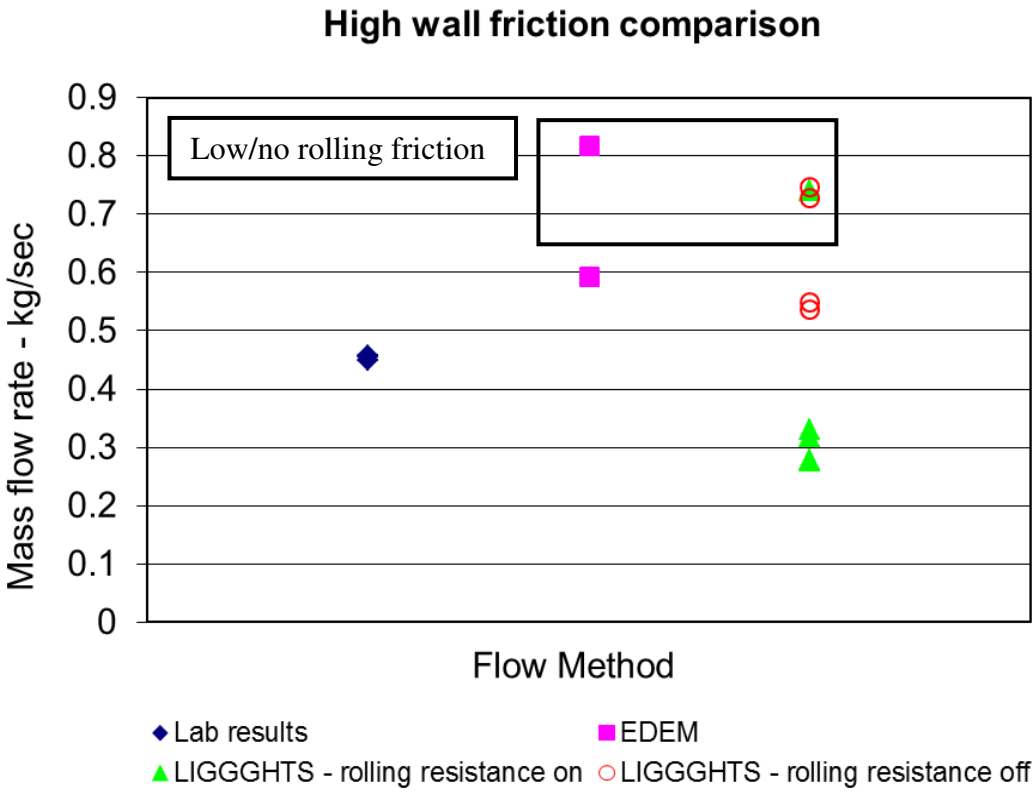

Figure 30 – A graphical comparison between the three methods for the rough walled hopper.

Figures 31 through 36 give a comparison of the qualitative aspects of all three methods. In general, EDEM appeared to more closely match the behavior of the lab scale flow tests than LIGGGHTS, although LIGGGHTS could perform nearly identically to EDEM and the lab scale flow tests under the right parameters. It is believed that the differences in rolling friction and the differences in material stiffnesses are the main cause of the discrepancies.

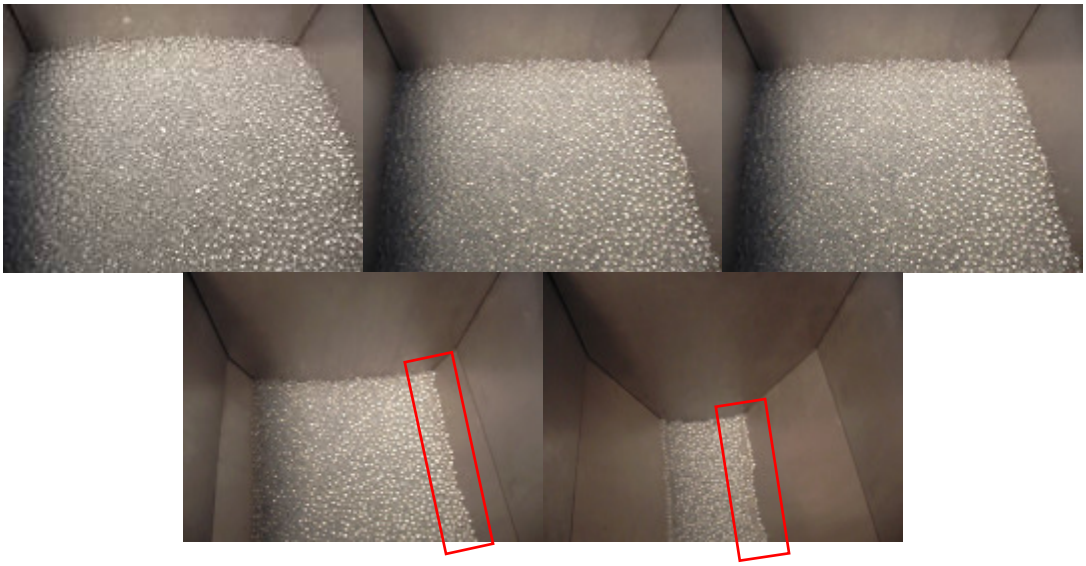

Figure 31 – Series of screenshots from a high speed video of beads draining from the quasi-3D hopper with smooth walls. Top surface of the beads stays essentially constant until near the hopper outlet, where a 3-5 bead think, single bead deep layer forms on the angled walls (see inset box). These results are typical.

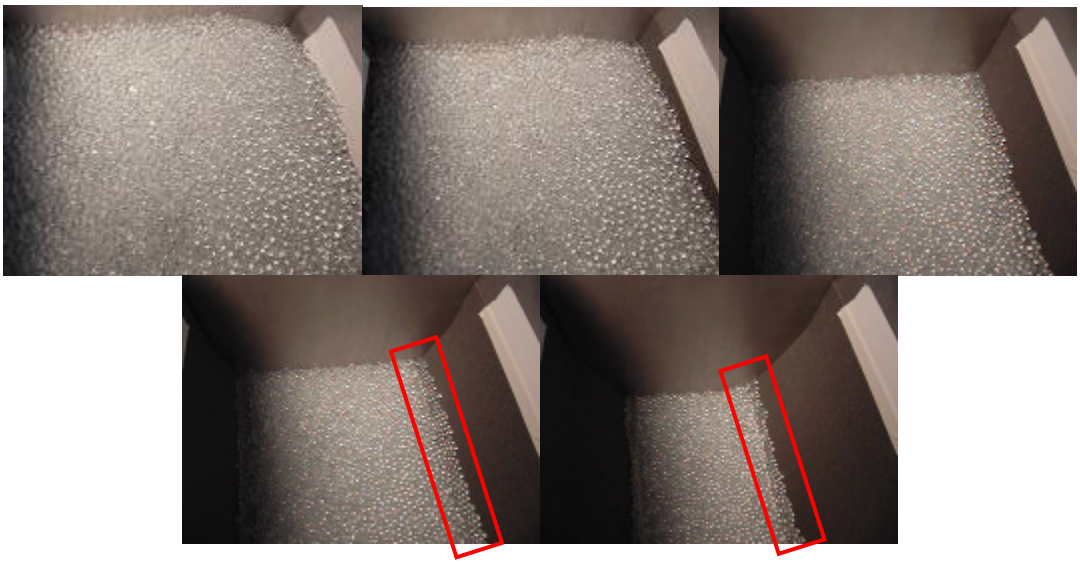

Figure 32 – Series of screenshots from a high speed video of beads draining from the quasi-3D hopper with rough walls. The single layer of beads on the side walls forms much higher in the funnel, and is a few beads larger (5-7 beads long, see inset box). However, the top surface is still overwhelmingly horizontal. These results are typical.

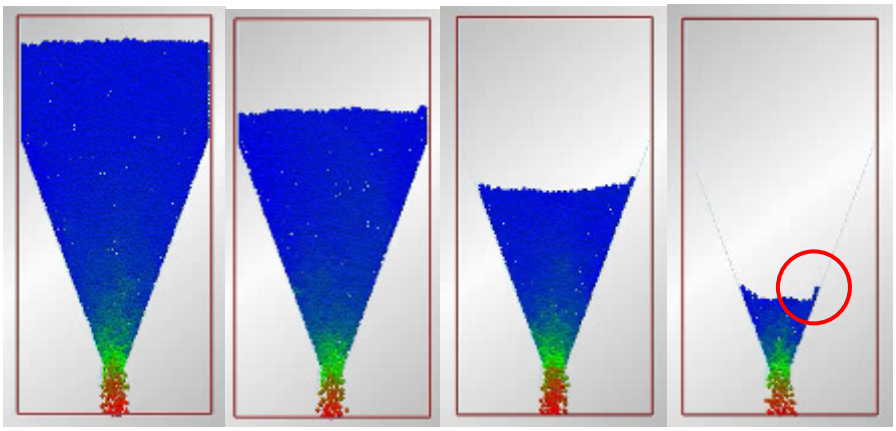

Figure 33 – Series of screen shots from an EDEM simulation running a Linear contact model simulation with high wall friction

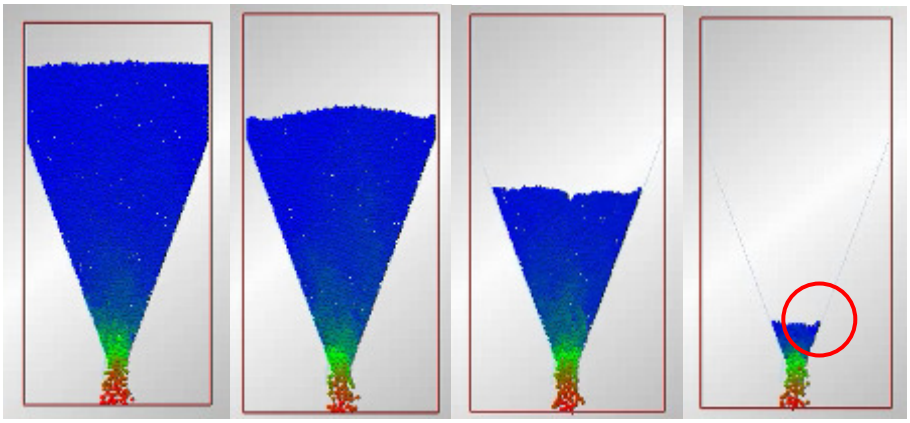

Figure 34 - Series of screen shots from an EDEM simulation running a Linear contact model with low wall friction.

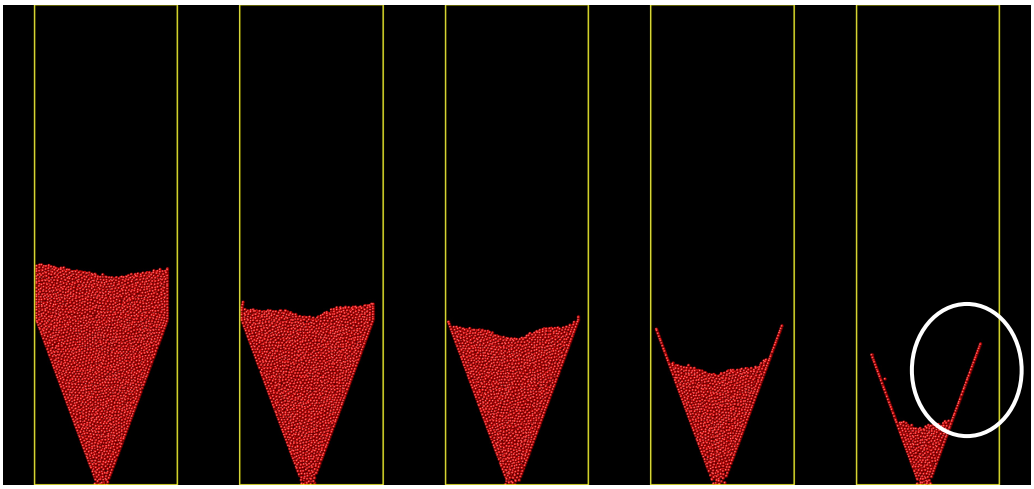

Figure 35 – Series of screen shots from a LIGGGHTS simulation running a Hertz-Mindlin contanct model with rolling friction on.

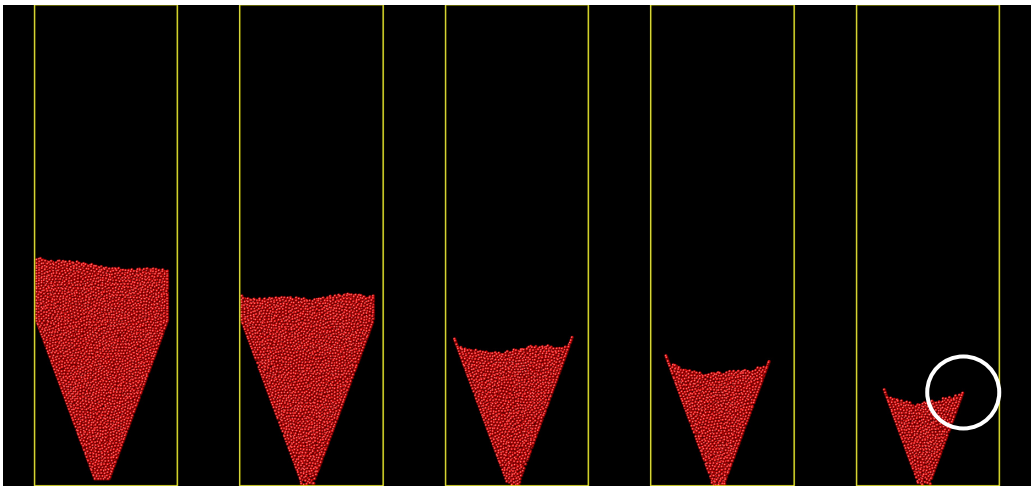

Figure 36 – Series of screen shots from a LIGGGHTS simulation running a Hertz-Mindlin contanct model with rolling friction off.

In general, the LIGGGHTS data is in good agreement with the lab scale experiments. The differences are probably due to the relatively high values for rolling friction used in the LIGGGHTS simulations. Figure 35 exhibits an exaggerated layer of marbles forming on the sides of the hopper near the discharge. This is most likely due to the exaggerated rolling resistance. Figure 36 shows a simulation with the rolling resistance turned off completely. Qualitatively, it is a much more accurate simulation of the lab scale flow, although it doesn't provide as accurate of a result for the mass flow rate.

In summary, this section has given qualitative and quantitative results of quasi-3D hopper flows using three different methods - a lab scale hopper, EDEM, and LIGGGHTS – and shows them to be in general agreement. Both LIGGGHTS and EDEM are capable

of producing results that agree with the results obtained by experimentation. The source of the discrepancies is believed to be the mismatch of material properties – especially rolling friction values and material stiffness – between the lab scale flow experiments and the DEM simulations.

5.2 – Full 3 dimensional hopper

Tables 9 and 10 summarize the mass flow rates obtained by experiment and simulation in the full 3D hopper. The results of the 3 dimensional experiments and simulations show stark quantitative differences in contrast to the results obtained in the quasi-3D case. The most obvious difference is the fact that the smooth walled lab scale flow tests had a lower mass flow rate than the rough wall lab scale flow tests, as seen in table 9. This was not predicted by DEM simulation, nor was it expected in the lab. There appear to be two likely candidates for this discrepancy. Figures 37 and 38 present the same information graphically.

Table 9 – Mass flow rates for the lab scale 3 dimensional hopper. The bottom row is the average.

rough walls	smooth walls
mass flow rate (kg/sec)	mass flow rate (kg/sec)
0.718	0.609
0.728	0.617
0.689	0.605
0.715	0.600
0.715	0.606
0.708	0.587
0.713	0.604

Table 10 – Mass flow rates for the 3 dimensional LIGGGHTS simulations.

	Sliding friction		Rolling Friction		
	particle-particle	particle-wall	particle-particle	particle-wall	mass flow rate (kg/sec)
Hertz	0.122	0.799	0.122	0.799	0.335
	0.32	0.669	0.32	0.669	0.332
	0.122	0.364	0.122	0.364	0.508
	0.32	0.236	0.32	0.236	0.473
Hooke	0.122	0.799	0.122	0.799	0.325
	0.32	0.236	0.32	0.236	0.474
	0.32	0.669	0.05	0.05	0.499
	0.32	0.669	0.01	0.05	0.527
	0.122	0.236	0.122	0.236	0.500*

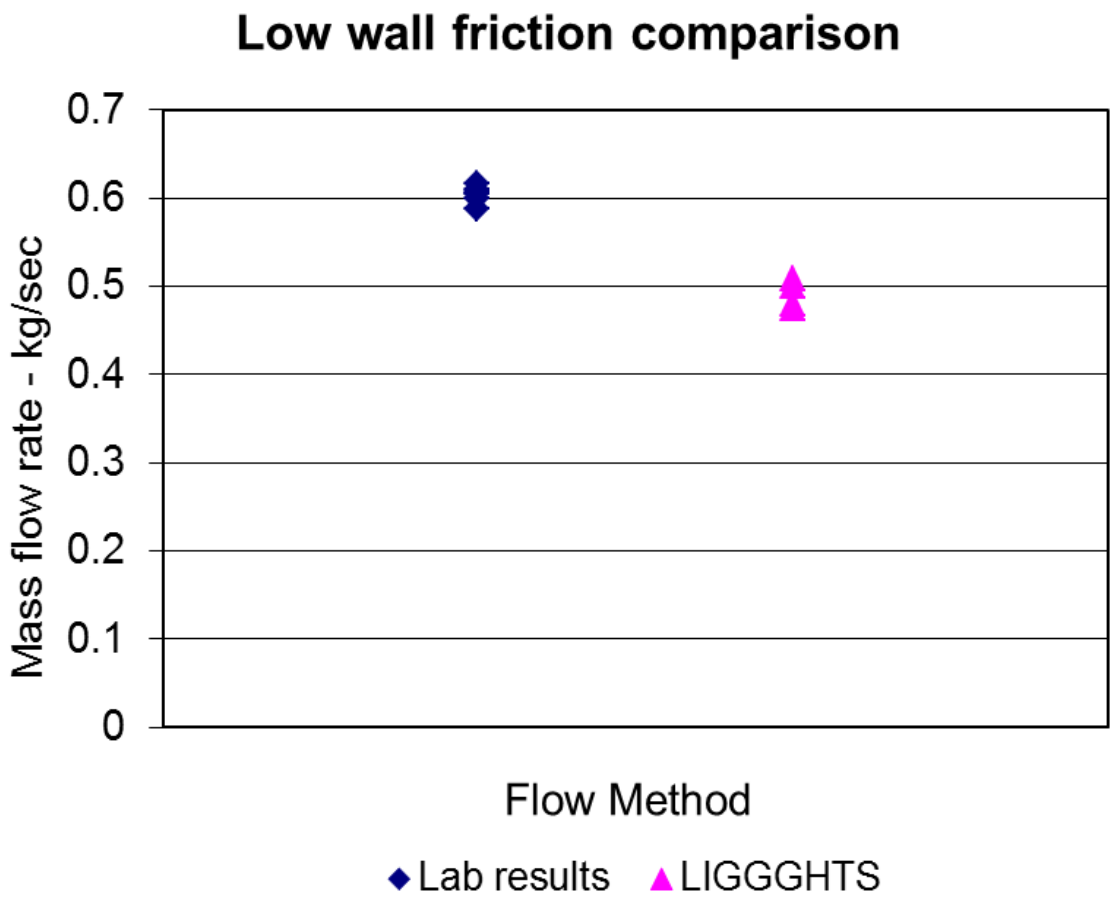

Figure 37 – A graphical comparison between the two methods for the smooth walled hopper.

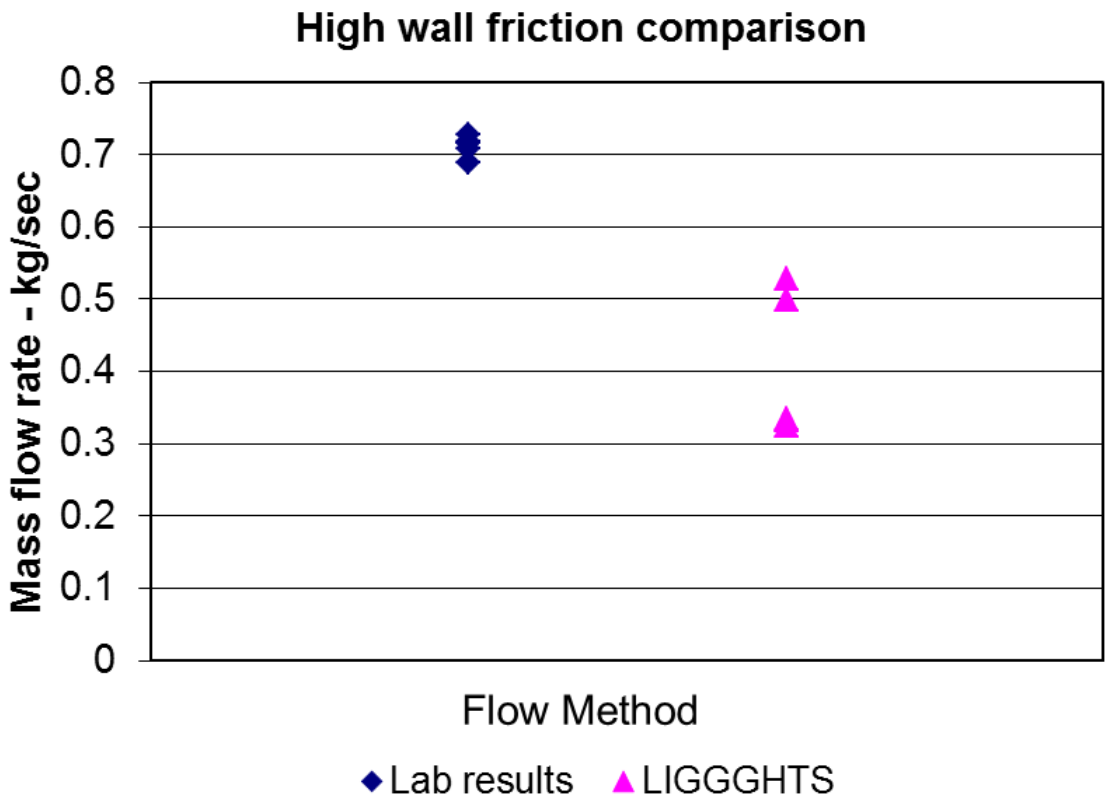

Figure 38 – A graphical comparison between the two methods for the rough walled hopper.

Figures 39 through 42 show some of the qualitative differences between the lab scale flow tests and LIGGGHTS. Although the higher rolling friction settings in LIGGGHTS could lead to behavior that was not observed in the lab scale flow tests, using lower friction values produced more realistic looking simulations. The qualitative discrepancy was observed with every rolling friction value tested (see figures 37 and 38).

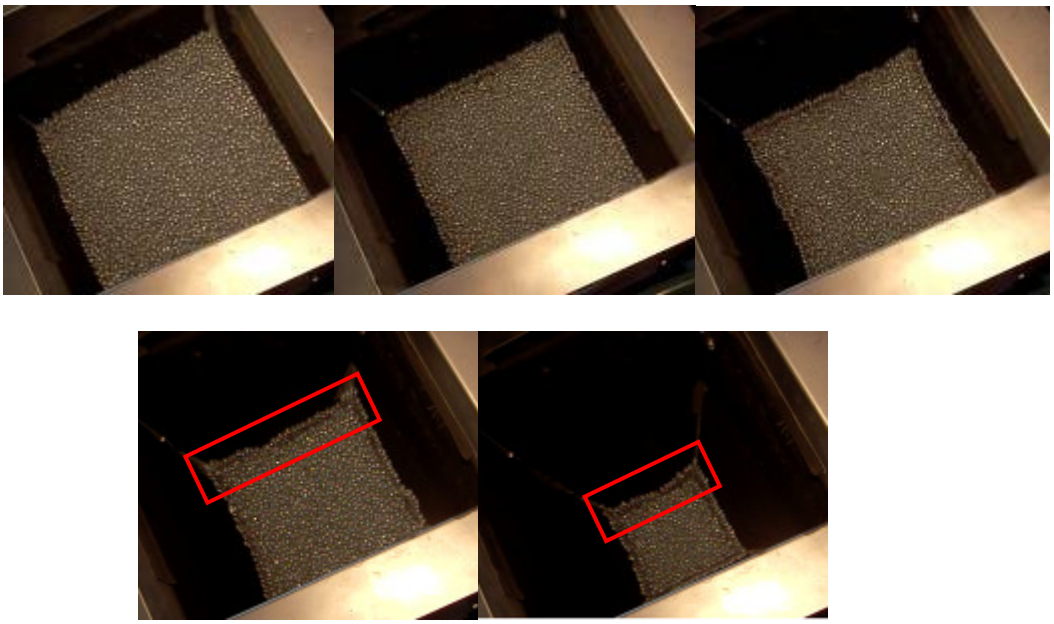

Figure 39 – Series of screenshots from a high speed video of beads draining from the 3D hopper with rough walls. A single layer of beads forms on the sloped walls nearly as soon the beads reach that level (see inset box). Marbles on top surface move towards center before moving downwards. This may be a sign of near funnel (or transitional) flow. These results are typical.

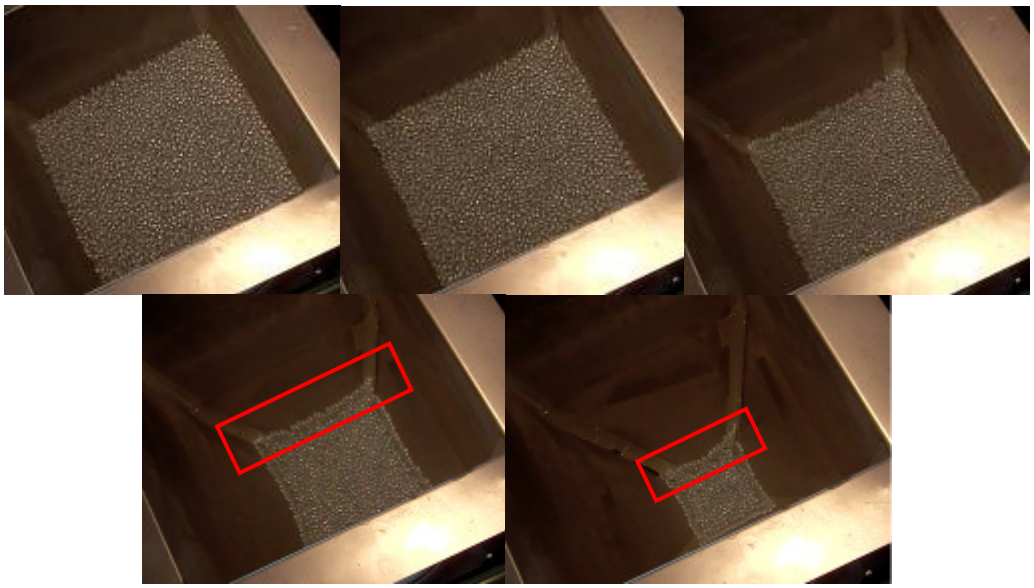

Figure 40 - Series of screenshots from a high speed video of beads draining from the 3D hopper with smooth walls. The results are nearly identical to those obtained with rough walls, with perhaps more marbles forming a layer on the sloped hopper walls (see inset box). These results are typical.

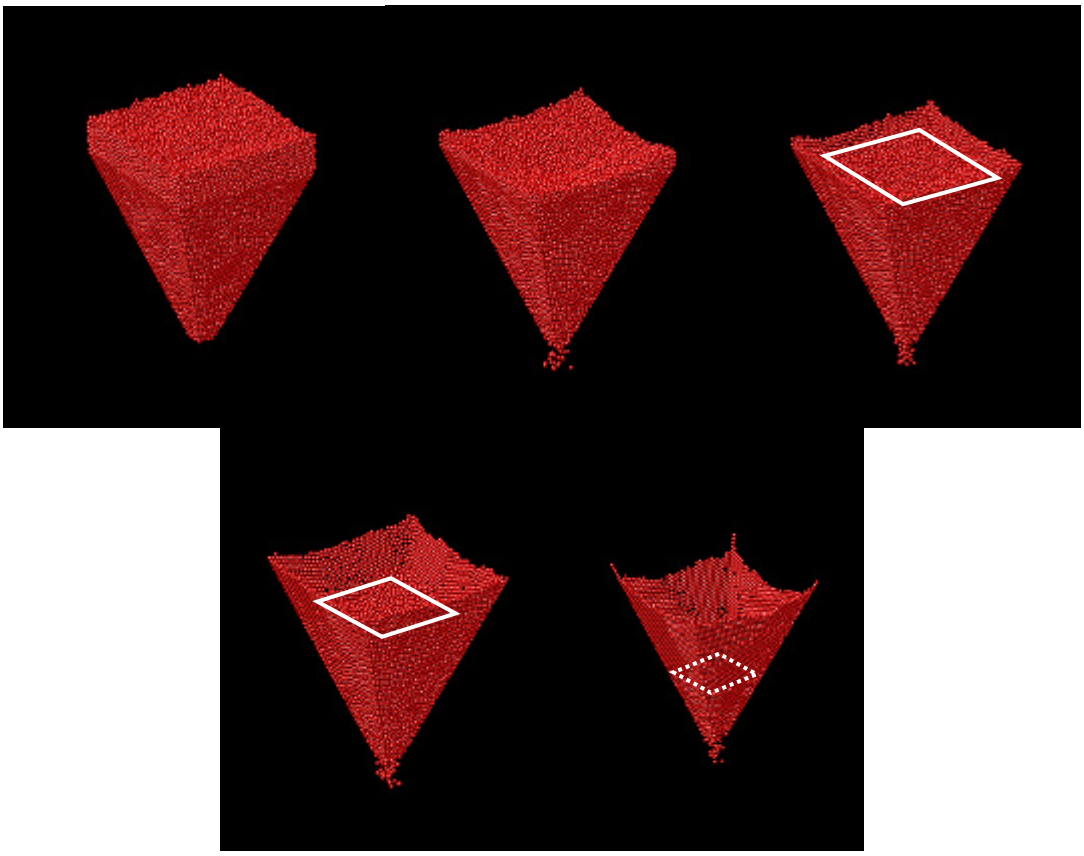

Figure 41 – Series of images from a 3D LIGGGHTS simulation running a linear contact model with high wall friction. In the last image, the top surface of the particles is hidden by the large shroud of particles along the sidewall. White diamond shows approximate level of top surface.

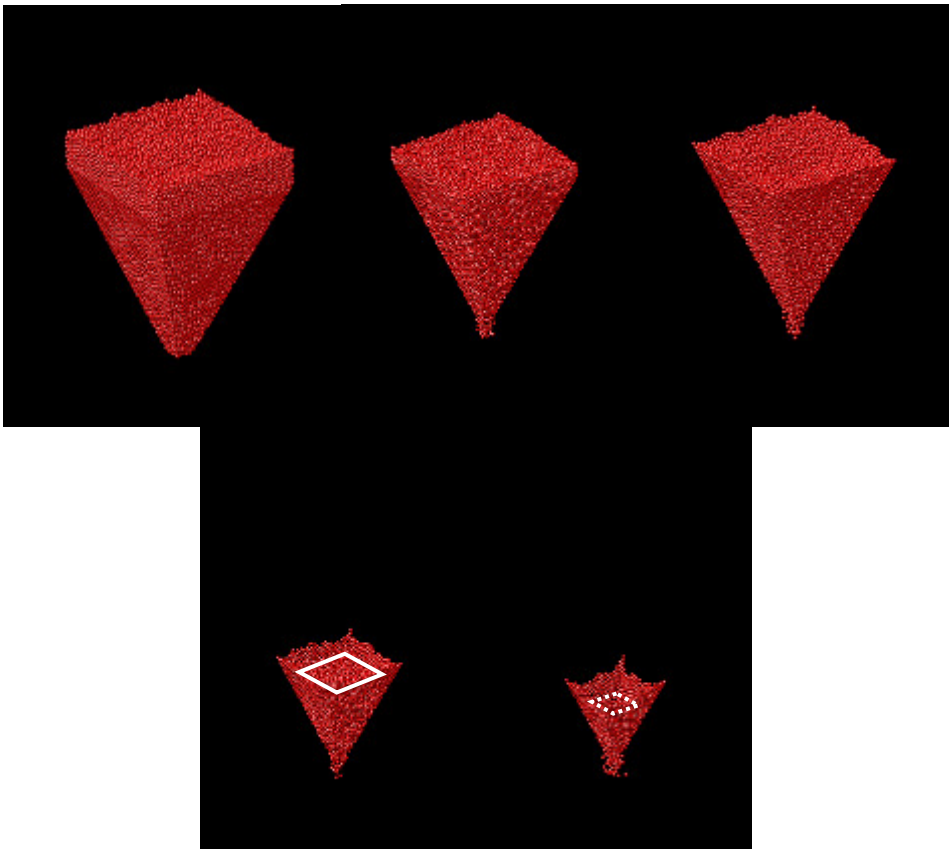

Figure 42 - Series of images from a 3D LIGGGHTS simulation running a Hertz-Mindlin contact model with low wall friction. These images more closely match the images taken from the lab scale flow tests, including the preferential corner flow. The amount of particles rolling down the sidewall is still somewhat exaggerated. White diamond shows approximate level of top surface.

There are a few possible explanations for the observed discrepancy in mass flow rates. The first explanation could be due to the presence of a buildup of a static electric charge during flow testing. It was noted that, at times, a build up static charge could be felt on the marbles after being discharged from the hopper in both hopper geometries. It could be possible that, if enough static charge were induced in the marbles, it could tend to act as a cohesive force between marbles and between the marbles and the hopper walls. This might explain why the effect wasn't noticed when running flow experiments using sand paper, as it may have acted as an insulator between the marbles and the walls. If this were the case, both LIGGGHTS and DEM have the ability to add a cohesive force between particles, which was not done in this study due to the fact that the cohesive force is unknown. This may also explain why LIGGGHTS tended to overestimate the mass flow rate for the smooth walled quasi-3D hopper. If that hopper were experiencing the same effect, but was still far enough to the left of its design curve, it would still experience overall mass flow but at a slower rate than expected. Experiments with steel balls or some other conducting material may be able to confirm or deny this effect.

Another possibility is that a given hopper geometry may have a smaller mass flow rate when experiencing mass or transitional flow as opposed to funnel flow. This funnel had been used in previous studies to determine if a selectively perforated baffle could change the flow regime of sand from funnel flow to mass flow. While that was indeed possible (a current approach used by industry is to insert small plates or cones near the outlet of a funnel flow hopper, converting it to mass flow; see figure 43), many of the perforated baffles that produced mass flow had lower mass flow rate than the original hopper experiencing funnel flow, even though the open area of the baffle was greater

than the open area of the hopper discharge (i.e., the baffle should not have been restricting flow).

Figure 43 - BINSERT® hopper insert system used to convert a funnel flow hopper to a mass flow hopper. Material flows both through and around the small interior cone. From Jenike.com (2013).

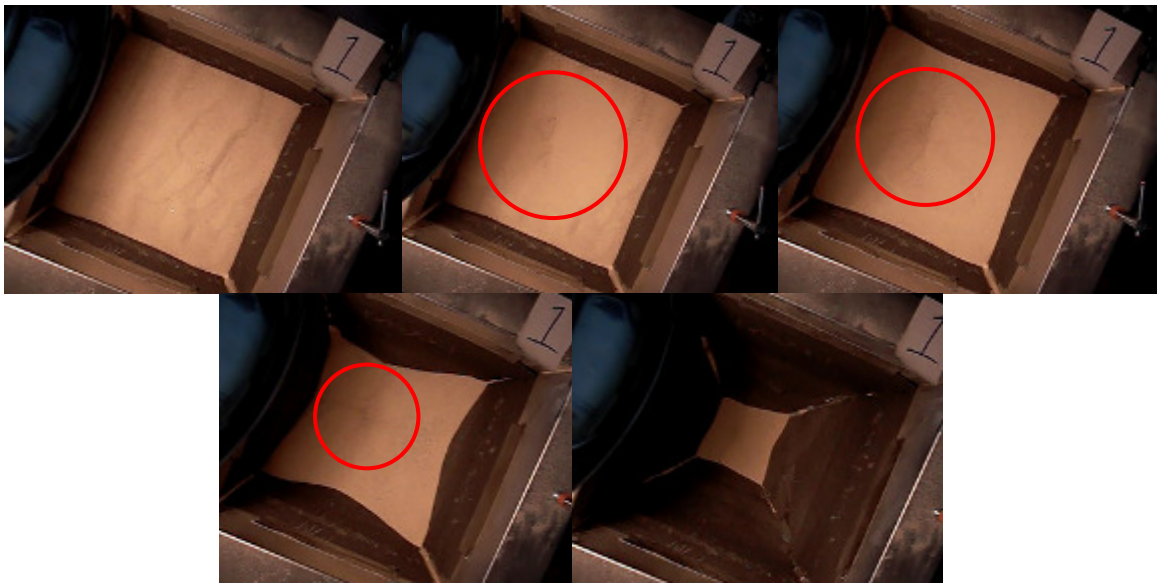

a.

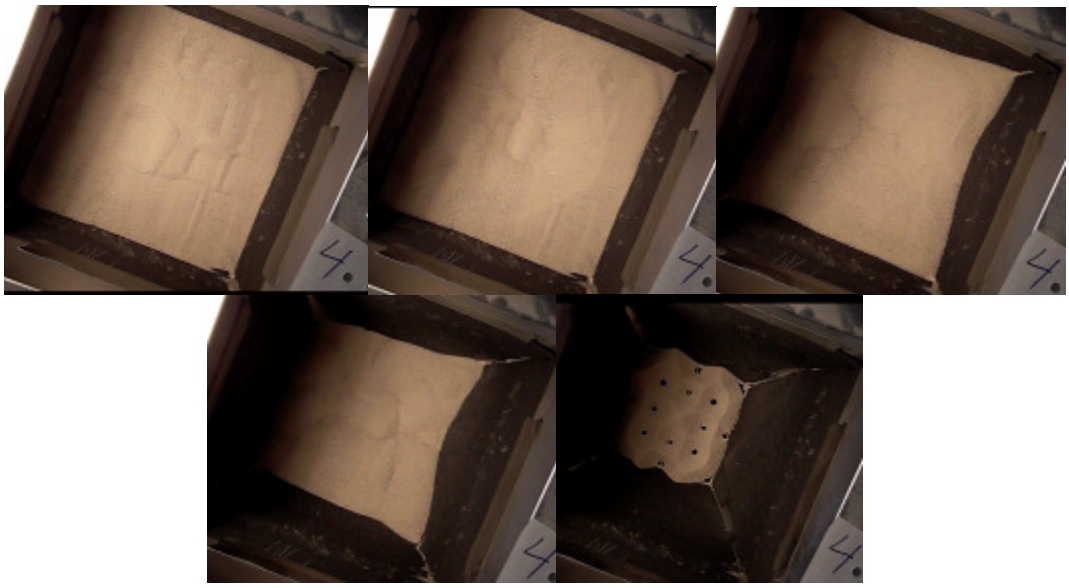

b.

Figure 44 – a. 3D hopper experiencing funnel flow with sand. Mass flow rate is .209 kg/sec. b. 3D hopper with perforated baffle inserted halfway up the angled hopper section. Flow appeared to change to mass flow, but slowed down to .1915 kg/sec.

This agrees somewhat with Bates (2008), who says that a mass flow hopper will flow slower than a funnel flow hopper of the same outlet geometry. This is because the overall mass flow rate of a hopper is determined by the velocity of the material through the outlet (see also Aguirre et al., 2010, who asserts that granular flow from a hopper is independent of pressure but directly proportional to the flow velocity). In the most extreme case of funnel flow, mass is discharged from the highest point in the hopper, leaving with the highest velocity attainable by material from anywhere in the bin. In contrast, material leaving the hopper in a mass flow design is always exiting from just above the outlet. Flow testing with altered hopper geometry may be able to confirm or deny this effect.

It was also noticed, during the course of flow testing, that the 3 dimensional hopper's geometry did not match up exactly with the geometry used in the LIGGGHTS simulations. Specifically, the physical hopper had steeper sides (roughly 18˚ in the lab compared to 20.2˚ in the simulation) and a slightly larger opening (a 3.81 cm by 3.81 cm square in the lab compared to a 3.18 cm by 3.18 cm square in the simulations). A new model was constructed which more closely matched the as measured dimensioned found in the lab. The mass flow results (the last row of data in Table **Error! Reference source not found.**, marked with an asterisk *) appear to show that the difference in geometry had a small effect on mass flow rates, but not enough to make up the previously observed difference. There are still probable geometry differences between the lab scale hopper and the computer generated model that are harder to account for, such as hopper wall flexing, a non-constant hopper outlet geometry, and other dynamic changes that happen

in the lab but not in the simulation. The construction of a more robust model, with tighter tolerances, may be able to confirm or deny these effects.

The most likely explanation as to the reason LIGGGHTS did not predict the reduced mass flow in a smooth walled hopper was because of the difference in material properties, especially the friction values, used in the simulation as compared to those present in the lab. As measured, the internal angle of friction of a material is the result of many particles in a sample tester forming stress chains through contact, while the friction measurement in this study only measured the angle of slip between a surface and three non-rotating particles. This could account for the greater discrepancy between lab results and simulated results from the full 3D hopper as compared to the quasi-3D wedge hopper, as the greater amount of particle chains that can be formed could amplify the effects of different friction values. Also, as noted by Ketterhagen (2009) in figure 24, the functional relationship between angle of friction and coefficient of friction are quite different between rotating and non-rotating particles.

González-Montellano et al. (2011) encountered a similar problem which they solved by an iterative process of updating the friction components in their simulations until acceptable predictions were made. This would also agree somewhat with the hopper design chart presented in figure 11. There are large areas of the chart where mass flow or funnel flow are possible, but it takes a certain combination of hopper geometry and material properties to produce a flow regime that is on the transition line, or even in the area of uncertainty. Therefore, reproducing such conditions in a computer simulation should be a more difficult task than simply simulating a hopper that is experiencing pure mass or funnel flow.

The most likely cause for the overall under prediction of LIGGGHTS for the mass flow rate of the 3D hopper is also due to improper friction values used in the simulations, especially rolling friction values. The results of the quasi-3D simulations show that LIGGGHTS, when employing a constant directional torque model of rolling resistance, can produce significantly lower predictions for mass flow rate than with it turned off.

In summary, this section has given qualitative and quantitative results of full 3D hopper flows using two different methods - a lab scale hopper and LIGGGHTS – and has provided some direct comparisons. In general, LIGGGHTS has under-predicted the observed mass flow rate from the lab scale flow testing, and did not predict the increase in mass flow rate observed in the lab when using a smooth walled hopper. The most likely explanations for this discrepancy are static charge buildup on the glass beads, differences between the lab scale hopper model and the computer model used in the simulations, and the fact that a given hopper geometry can have a higher mass flow rate if it is experiencing funnel flow as opposed to mass flow. It is thought that more testing in the lab could confirm or deny any of these effects.

5.3 – Uncertainty analysis

This section serves to provide the details used in the estimation of the uncertainty in the measurement of the mass flow rate of the lab scale experiments. In general, the sources of uncertainty in an experiment are from bias errors B and random errors P (Wheeler, 1996)

$$U_{total}^2 = B^2 + P^2 \tag{61}.$$

The bias error B is usually found from manufacturers statements about the limits of precision on their instruments, while the random error P is usually determined by statistical methods.

There were three sources of bias error in this study: the measurement of mass, the measurement of voltage, and the measurement of time. The measurement of mass and voltage produced errors in the calibration curves, while the measurements of voltage and time produced errors in the flow rate experiments themselves. Thus, the bias error B can be calculated as

$$B_{\dot{m}}^2 = \left(\dot{\mathrm{V}} \times U_{calibration}\right)^2 + \left(b_{calibration} \times U_{\dot{\mathrm{V}}}\right)^2 + \left(\frac{\partial \dot{m}}{\partial m} \times U_{mass}\right)^2 \tag{62}$$

where V is the voltage output, $U_{calibration}$ is the uncertainty in the slope of the calibration curve, $b_{calibration}$ is the slope of the calibration curve, m is mass, U_{mass} is the uncertainty in the mass measurement, and the over dot indicates the time rate of change of a variable.

$\dot{\mathrm{V}}$ is determined by performing a linear regression on the voltage output of a given set of flow test data. $U_{calibration}$ is associated with the random error of the slope of the calibration curve, $b_{calibration}$, and is found by

$$U_{calibration} = t \times S_{calibration} \tag{63}$$

where t is the Student's t variable associated with the given degrees of freedom and confidence level, and $S_{calibration}$ is the standard error of the slope of the calibration curve $b_{calibration}$ and is determined by statistical methods. $U_{\dot{\mathrm{V}}}$ is the uncertainty in the measurement of the rate of change of the voltage, and will be discussed in the proceeding

paragraphs. $\frac{\partial \dot{m}}{\partial m}$ is calculated as $\frac{\partial \dot{\mathrm{V}} \times b_{calibration}}{\overline{m}}$, where $\overline{m}$ is the average calculated value of mass for a given set of flow data. U_{mass} is found from the scale manufacturers stated limits of precision on the scale.

$U_{\dot{\mathrm{V}}}$ is found by

$$U_{\dot{\mathrm{V}}}^2 = \left(\frac{\dot{\mathrm{V}}}{\overline{\mathrm{V}}} U_{\mathrm{V}}\right)^2 + \left(\frac{\dot{\mathrm{V}}}{\bar{t}} U_t\right)^2 \tag{64}$$

where V and t refer to voltage and time respectively, and the over bar represents an average value for the variable. Both U_{V} and U_t are found from manufacturers' data.

U_{V} is the uncertainty in the measurement of voltage and has two sources: the Keli load cell, and the Agilent data acquisition system. Thus, U_{V} can by found by

$$U_{\mathrm{V}} = U_{Keli} + U_{Agilent} \tag{65}.$$

The load cell uncertainty is simply a percentage of the full scale of the output, while the Agilent uncertainty has components of both the full scale and the actual reading. Detailed calculations and tables will be presented in appendix C.

Using the calibration data from figure A.4 and the flow data from figure A.5(a), the total uncertainty in the measurement of the mass flow rate is .00255 kg/sec, or .355 % of the calculated mass flow rate. This was split fairly evenly between the overall bias and precision errors, which were .00164 kg/sec and .001952 kg/sec respectively.

In summary, this section has identified and analyzed some of the possible sources of error in the measurement of the mass flow rate for the lab scale flow tests. Using one set of data from the lab scale flow tests, it was shown that the error in the mass flow rate

measurement was less than 1 %. This implies that not only are the measured values for mass flow rates fairly accurate, but that any discrepancies between mass flow rates as measured in the lab and calculated in a simulation can not be accounted for by experimental uncertainty.

Chapter 6

Conclusions and Future Work

This research has given a motivation for the study and simulation of granular flows. Then, it gave a review of some of the fundamentals of both the flow of granular materials in hoppers and the discrete element method. Then, an experimental apparatus for the measurement of mass flow rates from a quasi-3D hopper and a 3 dimensional pyramidal hopper was described. Then, the basic procedure used for simulating granular flows by the use of two different discrete element modeling software packages, EDEM and LIGGGHTS, was described. Finally, the results were compared across platforms and discrepancies were discussed.

In general, the discrete element can be used to effectively model the flow of granular materials at the lab scale, assuming that accurate material properties are known. The main limitations of its adoption over experimental studies are intensive computational requirements (especially for full scale simulations), the ability to accurately determine the macroscopic flow properties of the materials in question, and the determination of whether a small scale experiment or simulation can accurately represent the physics of a full scale granular flow (Carson et al., 2008). If each of those criteria can be met satisfactorily, then the discrete element method should be considered for the study of granular flows.

The difference between DEM software packages as far as simulating granular flows appears minor. Both DEM software packages were able to produce results that

were very similar to each other, both qualitatively and quantitatively. The choice of DEM software should be based on desired features, not simulation accuracy.

Going forward, with the geometric models already built, more accurate data for the flow properties of the materials in question could be gained from more experimentation or from published sources, leading to more accurate simulations. Both EDEM and LIGGGHTS offer the capability to insert particles that follow a distribution of sizes, which can be used to study the effects of the different sizes of particles expected to be encountered in practice. Both software packages have the ability to model non-spherical particles, also enhancing the accuracy of the simulation. Both software packages have the ability to insert multiple types of particles into a simulation, with each type having its own specified size and material properties.

In what could be a potentially important aspect of modeling as far as thermal energy storage is concerned, both EDEM and LIGGGHTS (and the discrete element method in general) can be used to model heat conduction in granular flows. This could be used to study the flow of a granular material over a heated surface, such as a heat exchanger tube (to study heat transfer and heat exchanger design) or through a chute or orifice (to study heat related stresses and failures in such components). Examples of DEM based conductive heat transfer studies have been performed by Vargas and McCarthy (2001), who concluded that bulk conductivity in a granular material is related to stress levels within the material, and by Kruggel-Emden et al. (2006) who performed heat transfer studies of granular flows similar to those presented in the current study.

Both software packages also offer the ability to couple granular flow calculations using the discrete element method to more general field calculations using the finite

element method. This could be used to model the flow of granular material through a solar receiver (coupling a radiation field and convection effects with the discrete element flow) or through a heat exchanger section (coupling convection inside the heat exchanger with the granular flow outside the heat exchanger). A study by Simsek et al. (2009) provides an example of such a coupled simulation. While the computational cost for such coupled simulations is expected to be extremely high, the ability to study what happens at the particulate level could provide ample motivation for continued research.

Appendix A

Detailed lab scale results

The following figures show the data collected in the lab scale experiments, as well as the calibration data.

A.1 – Quasi 3D data

Note that the reported mass flow rate in figures A.2 and A.3 is for the entire length of the lab scale hopper. To get the results listed in table 4, the length of the lab scale hopper was divided by the width of the hopper used in the simulations.

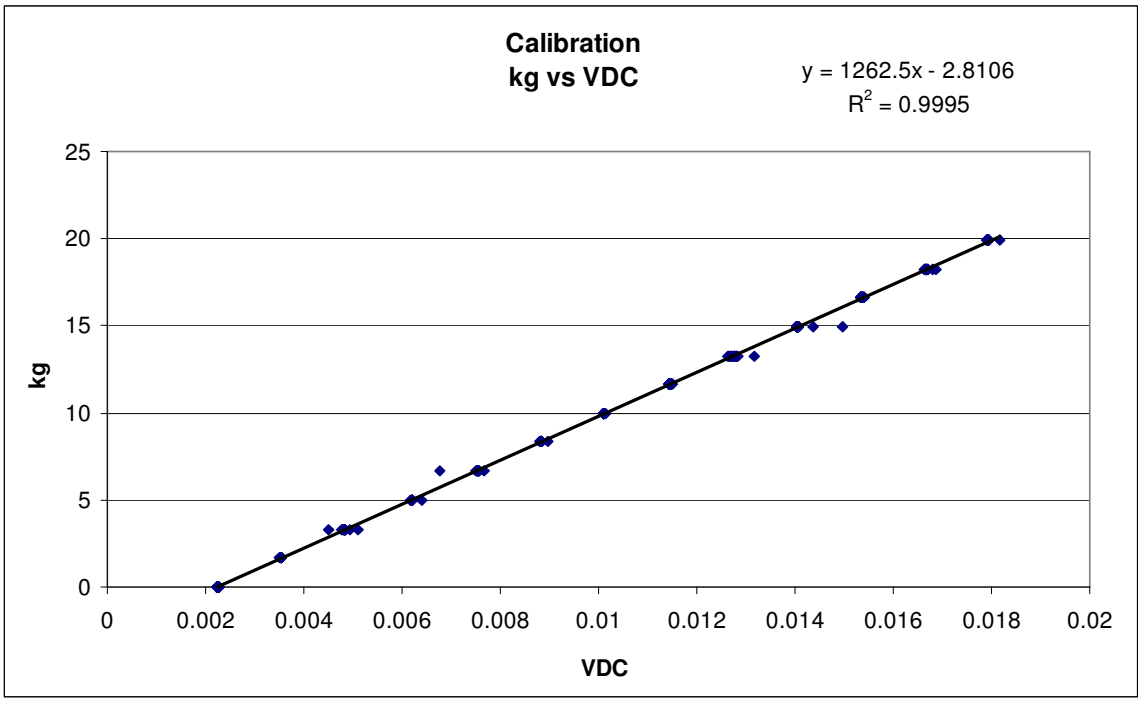

Figure A.1 – Calibration data for the quasi-3D data collection.

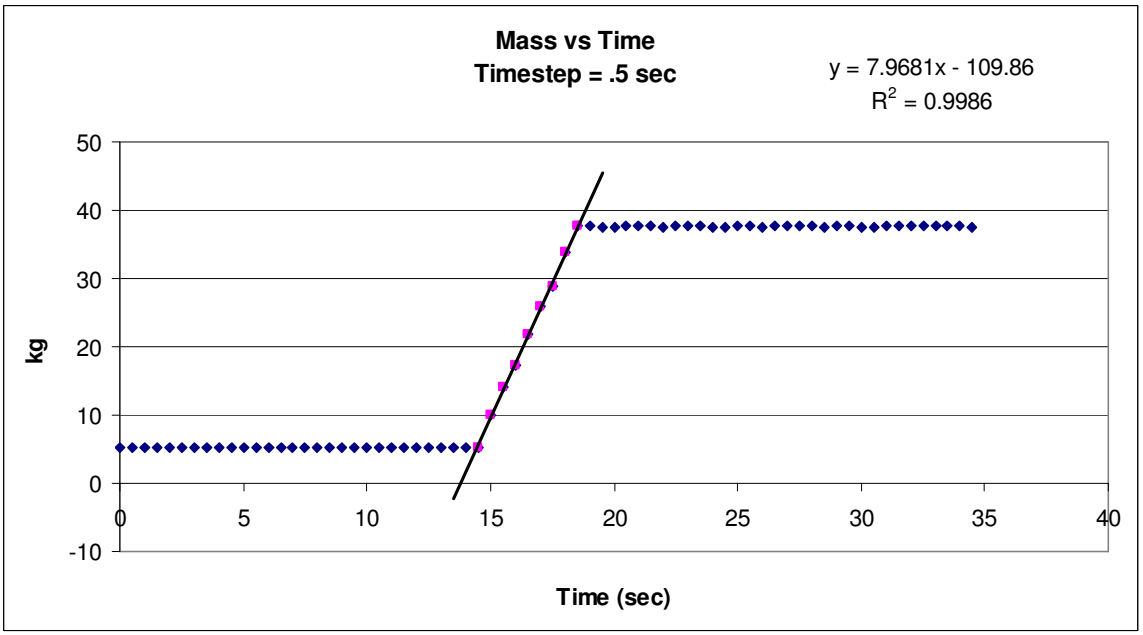
Mass vs Time
Timestep = .5 sec
y = 7.9681x - 109.86
R2 = 0.9986
kg
Time (sec)
50
40
30
20
10
0
-10
0
5
10
15
20
25
30
35
40

a.

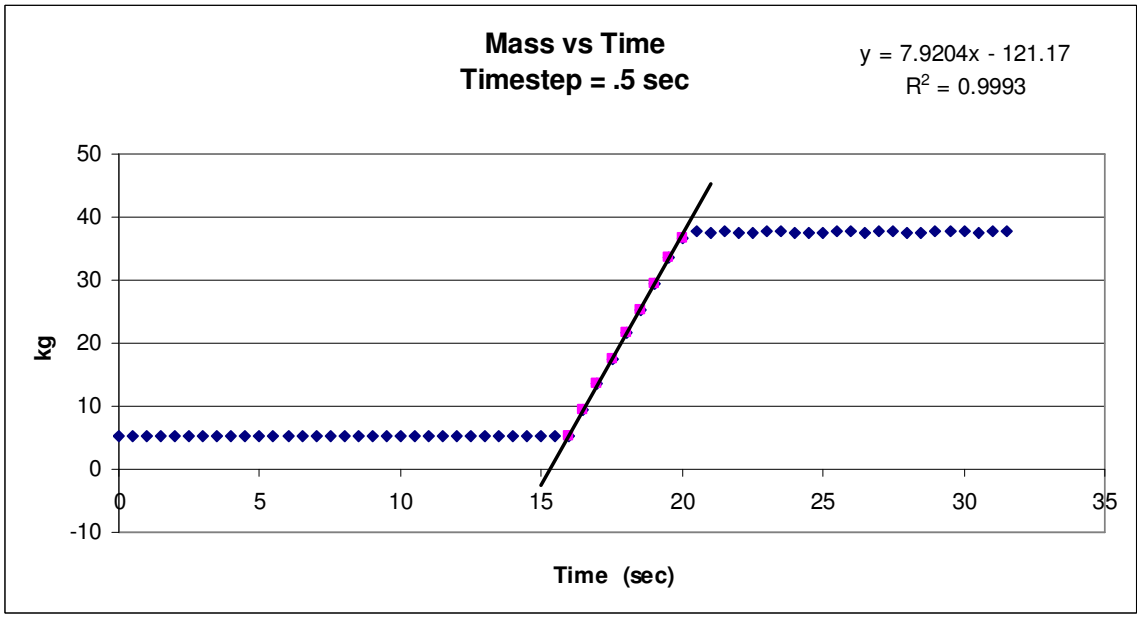
Mass vs Time
Timestep = .5 sec
y = 7.9204x - 121.17
R2 = 0.9993
kg
Time (sec)
50
40
30
20
10
0
-10
0
5
10
15
20
25
30
35

b.

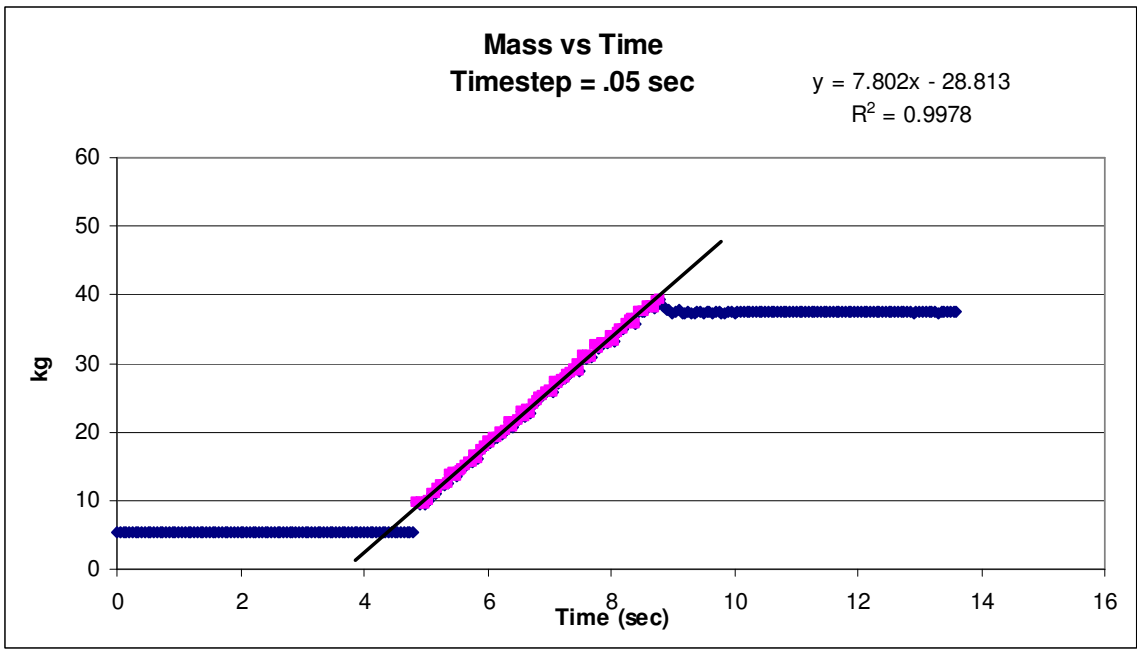

c.

Figure A.2 (a-c) - Data from lab scale quasi-3D hopper with rough walls. Slope of equation is the mass flow rate in kg/sec. Blue marks are collected data, purple marks represent data used to calculate the mass flow rate, and the solid black line is the mass flow rate equation in the top right. Time step used varied between .5 and .05 seconds.

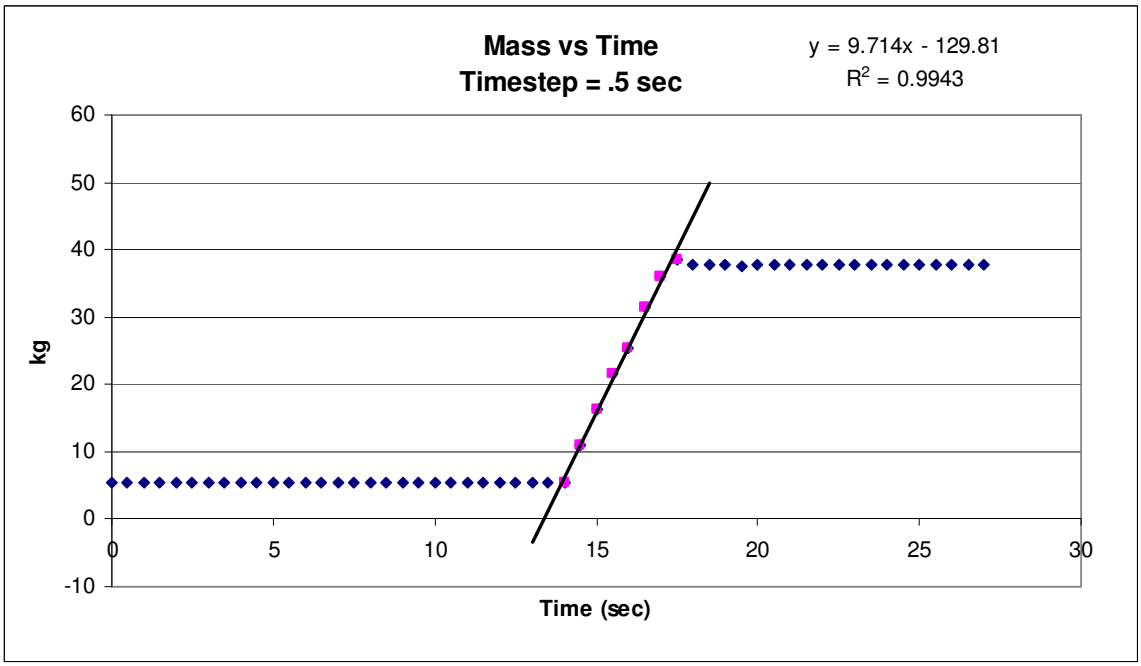
Mass vs Time
Timestep = .5 sec
y = 9.714x - 129.81
R2 = 0.9943
kg
Time (sec)
60
50
40
30
20
10
0
-10
0
5
10
15
20
25
30

a.

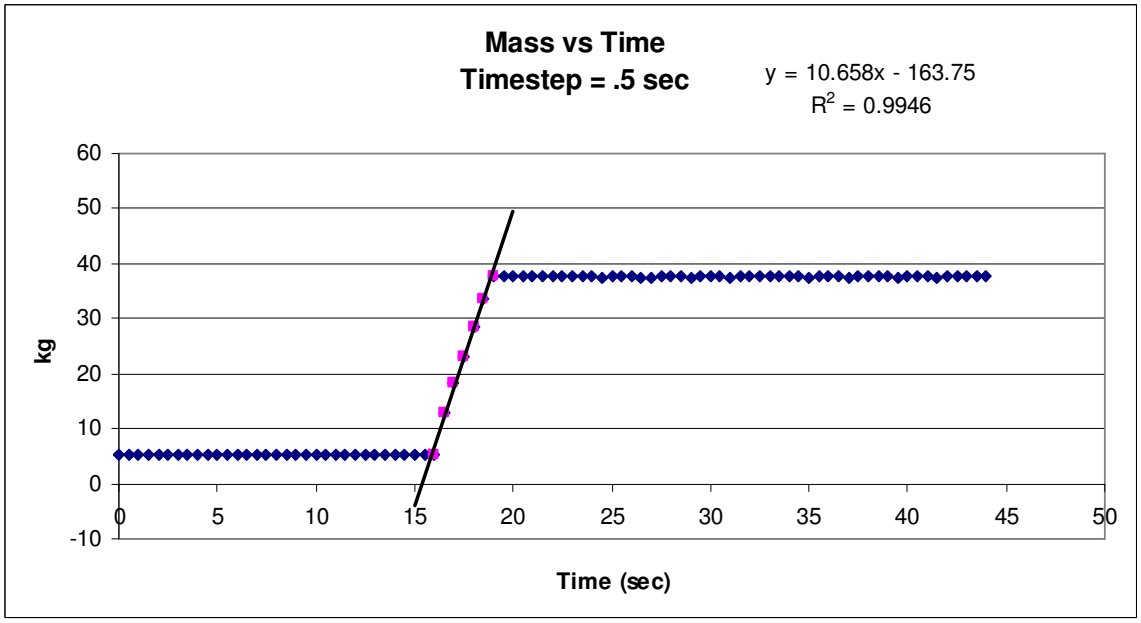
Mass vs Time
Timestep = .5 sec
y = 10.658x - 163.75
R2 = 0.9946
kg
Time (sec)
60
50
40
30
20
10
0
-10
0
5
10
15
20
25
30
35
40
45
50

b.

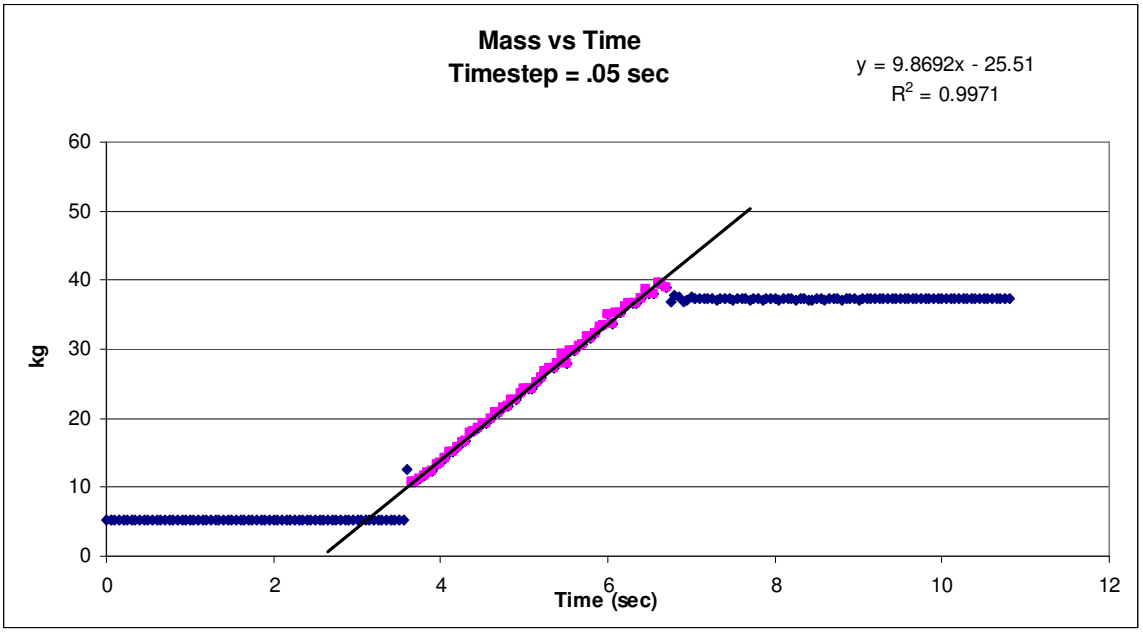

c.

Figure A.3 (a-c) - Data from lab scale quasi-3D hopper with smooth walls. Slope of equation is the mass flow rate in kg/sec. Blue marks are collected data, purple marks represent data used to calculate the mass flow rate, and the solid black line is the mass flow rate equation in the top right. Time step used varied between .5 and .05 seconds.

A.2 – Full 3 dimensional data

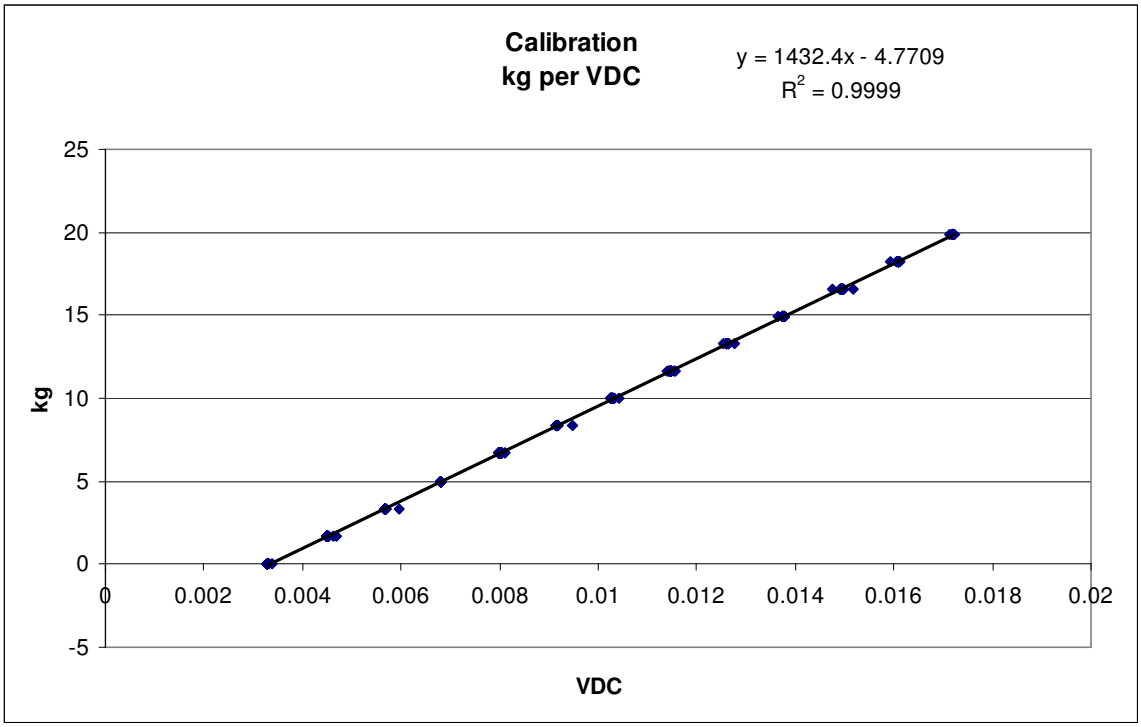

Figure A.4 – Calibration data for 3 dimensional data collection. The outlying marks are either due to improper grouping (i.e., the assumed voltage is paired with the incorrect weight), or a reading was taken while a brick was being added or taken off of the load cell platform.

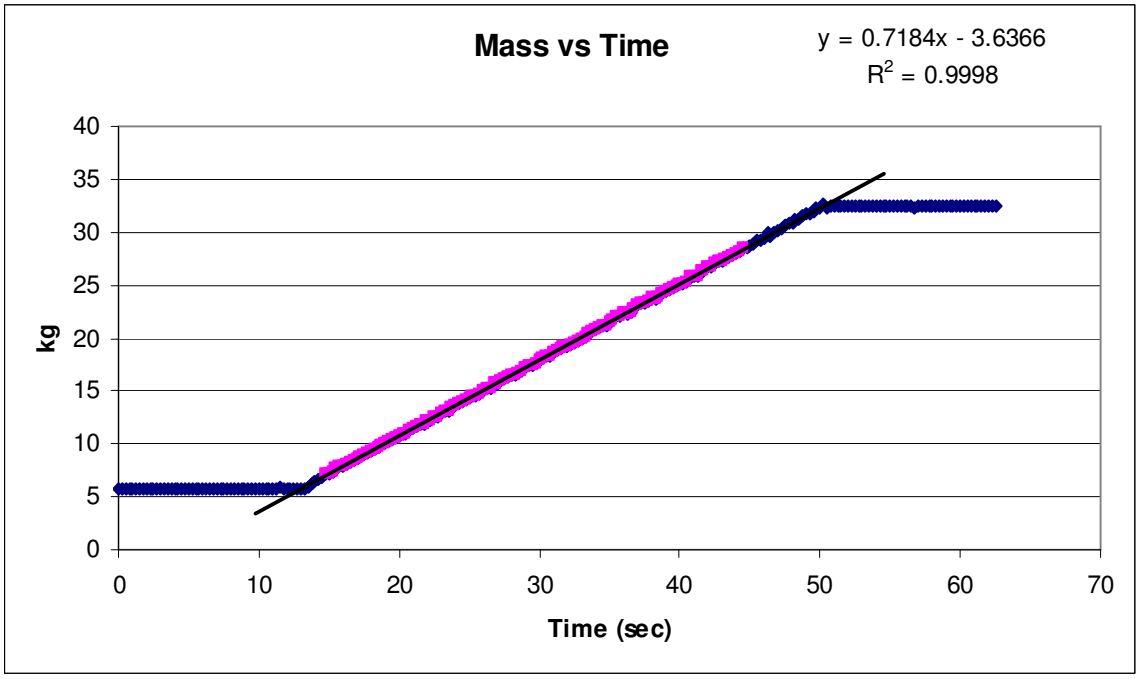
Mass vs Time
y = 0.7184x - 3.6366
R2 = 0.9998
kg
Time (sec)
0
5
10
15
20
25
30
35
40
0
10
20
30
40
50
60
70

a.

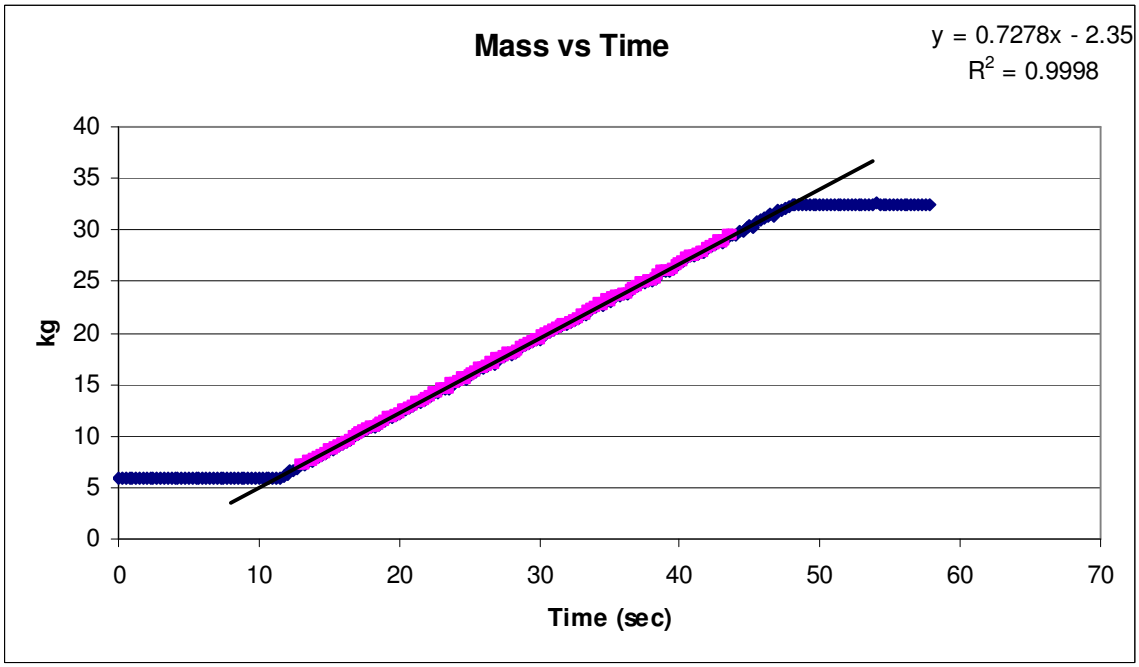
Mass vs Time
y = 0.7278x - 2.35
R2 = 0.9998
kg
Time (sec)
0
5
10
15
20
25
30
35
40
0
10
20
30
40
50
60
70

b.

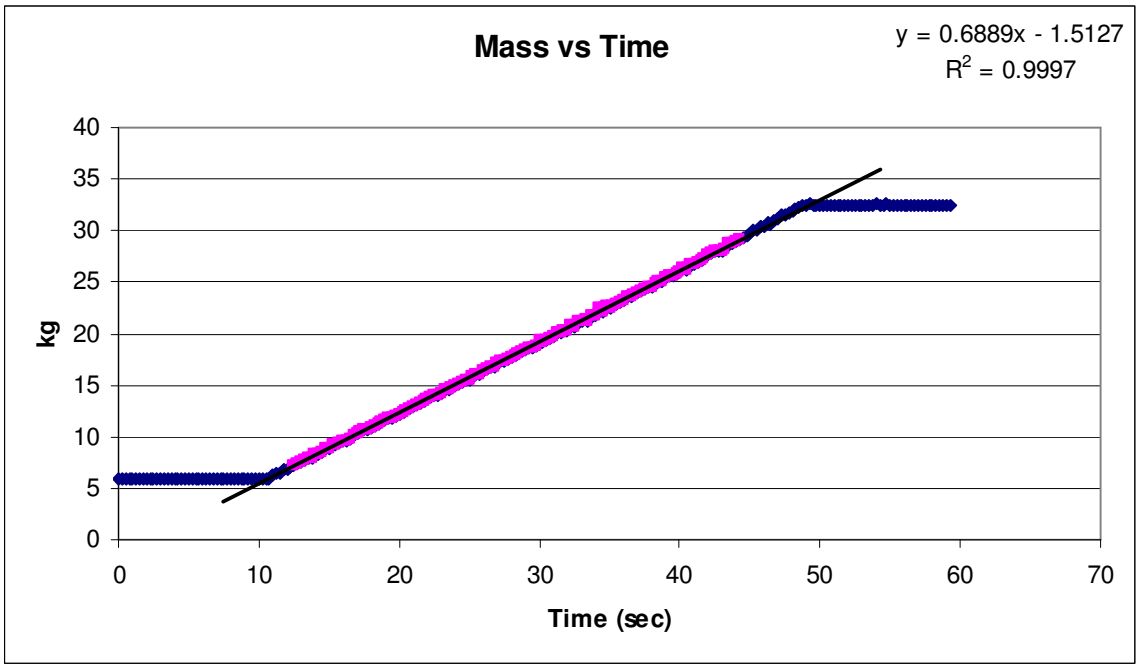
Mass vs Time
y = 0.6889x - 1.5127
R2 = 0.9997
kg
Time (sec)
0
5
10
15
20
25
30
35
40
0
10
20
30
40
50
60
70

c.

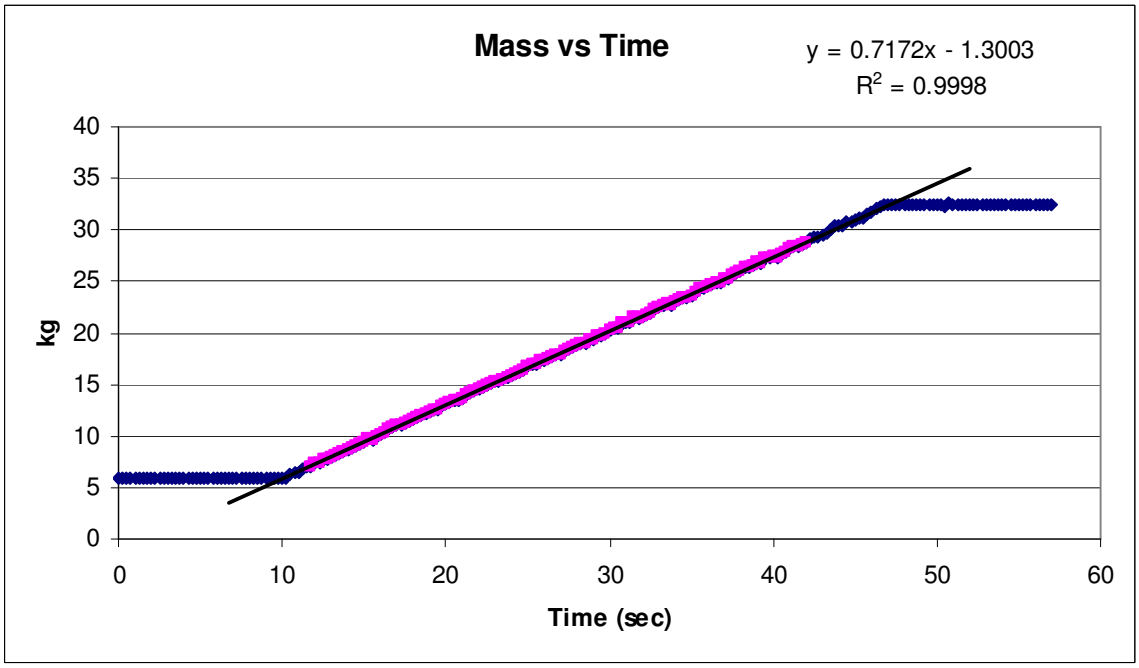
Mass vs Time
y = 0.7172x - 1.3003
R2 = 0.9998
kg
Time (sec)
0
5
10
15
20
25
30
35
40
0
10
20
30
40
50
60

d.

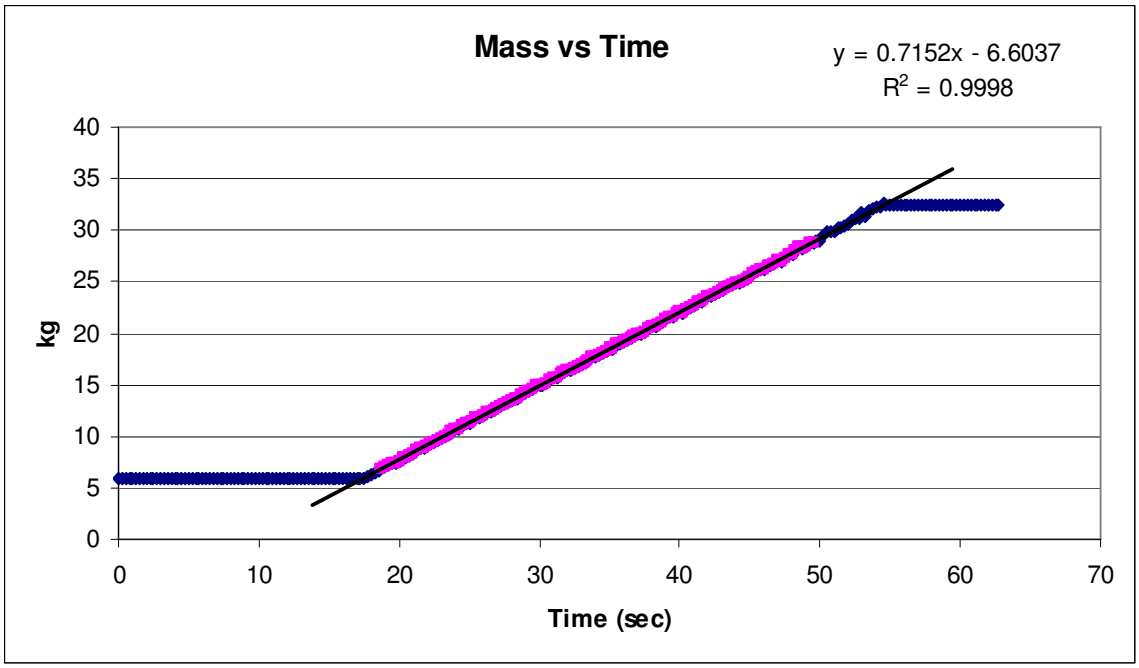

e.

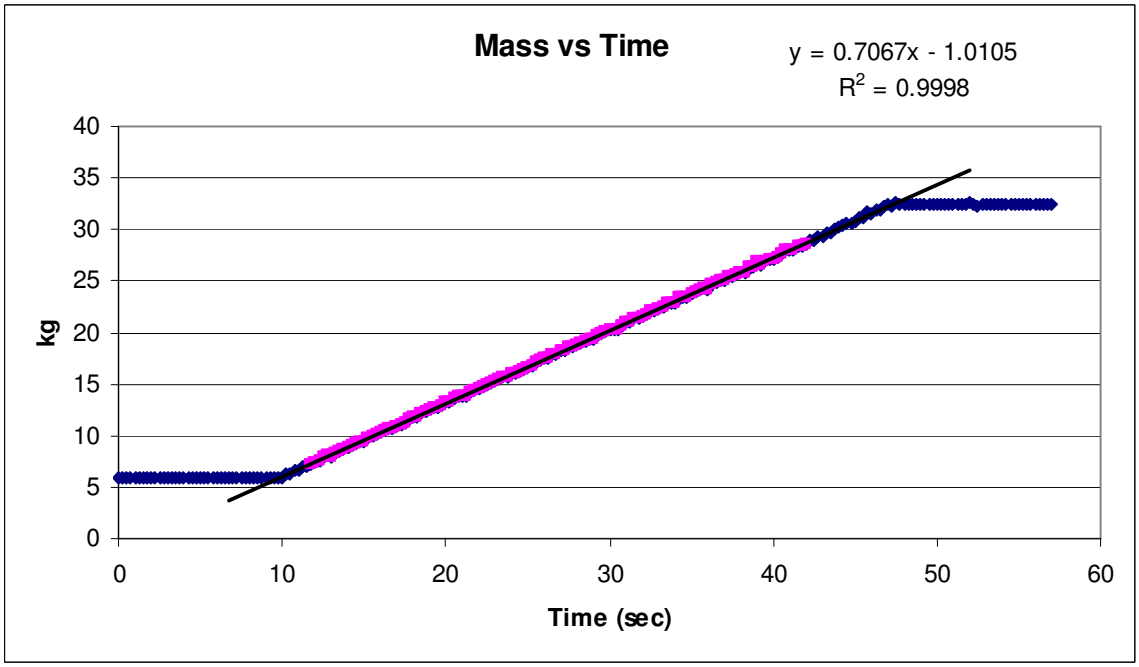

f.

Figures A.5 (a-f) – Data from lab scale 3 dimensional hopper with rough walls. Slope of equation is the mass flow rate in kg/sec. Blue marks are collected data, purple marks represent data used to calculate the mass flow rate, and the solid black line is the mass flow rate equation in the top right. Time step used was .25 seconds.

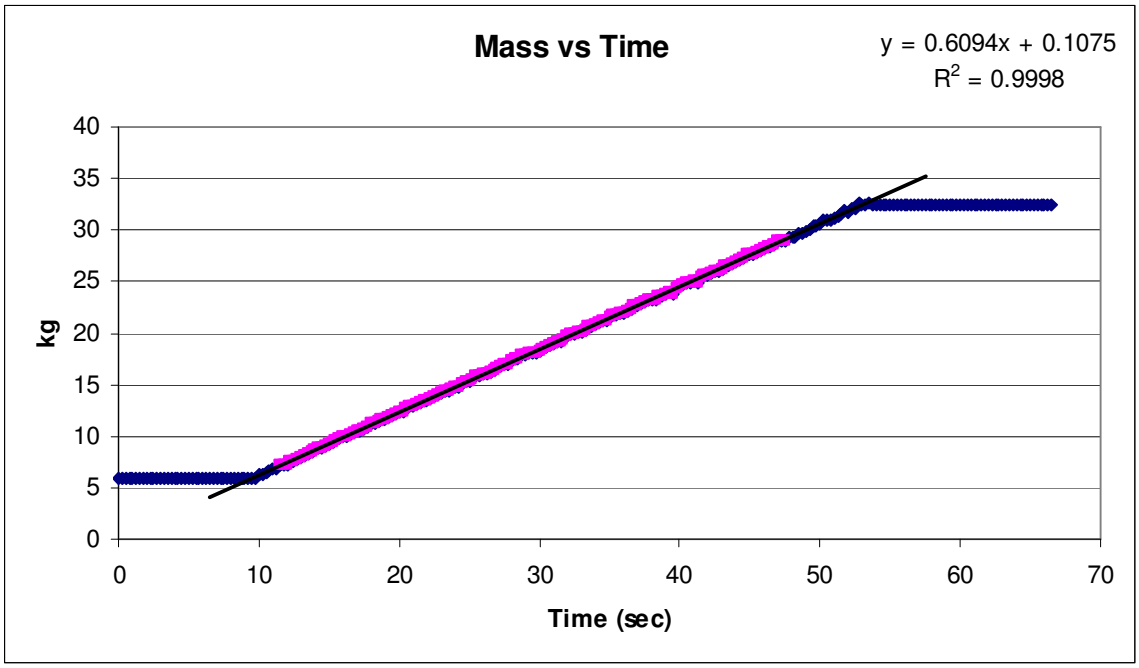
Mass vs Time
y = 0.6094x + 0.1075
R2 = 0.9998
kg
Time (sec)
0
5
10
15
20
25
30
35
40
0
10
20
30
40
50
60
70

a.

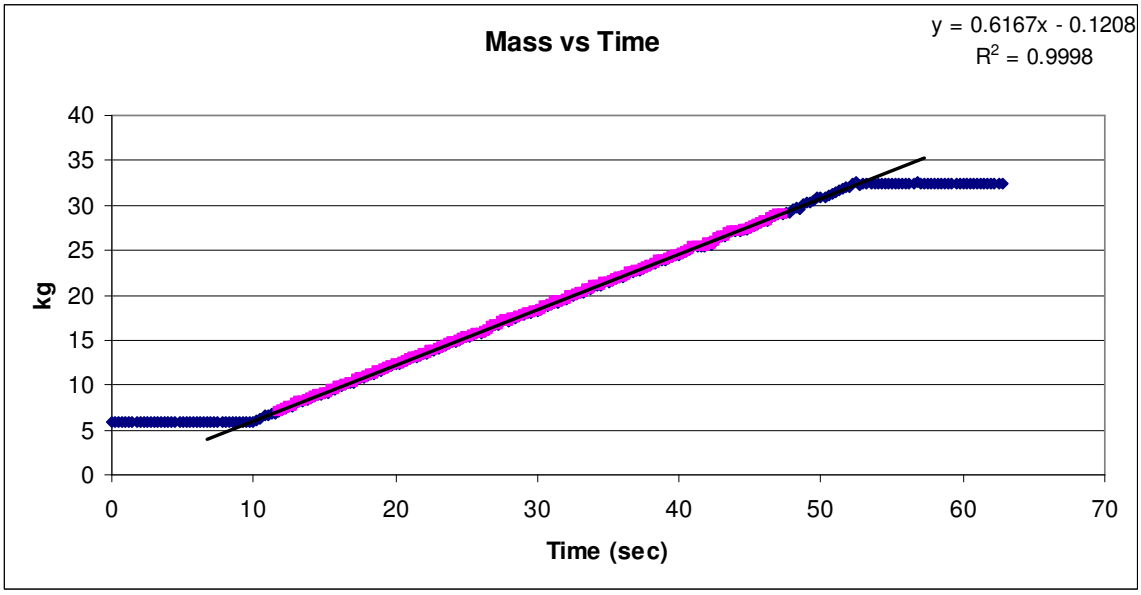
Mass vs Time
y = 0.6167x - 0.1208
R2 = 0.9998
kg
Time (sec)
0
5
10
15
20
25
30
35
40
0
10
20
30
40
50
60
70

b.

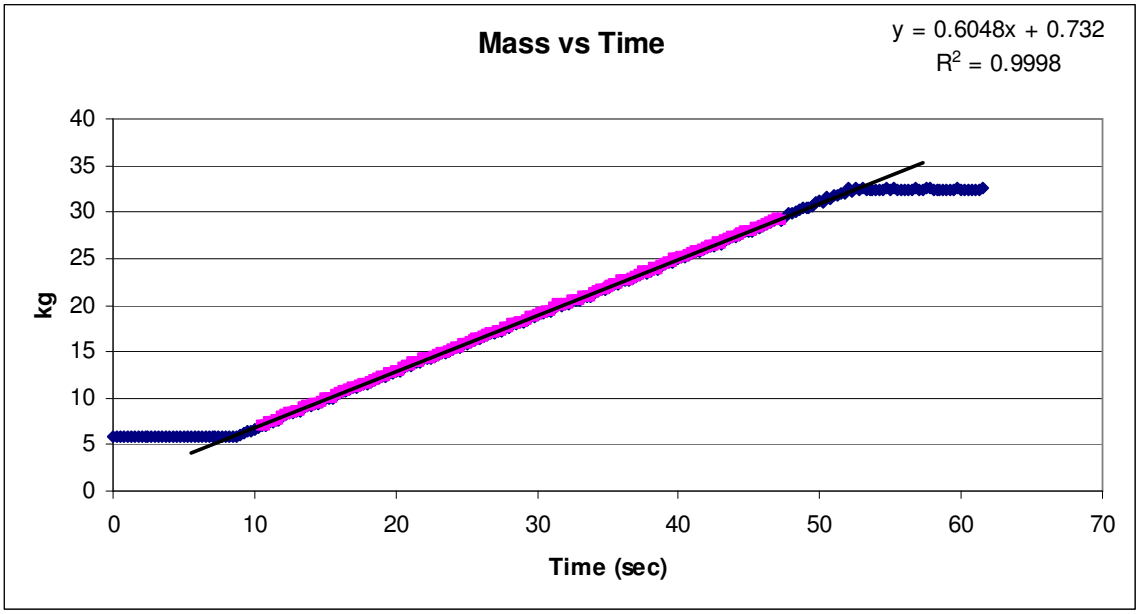
Mass vs Time
y = 0.6048x + 0.732
R2 = 0.9998
kg
Time (sec)
0
5
10
15
20
25
30
35
40
0
10
20
30
40
50
60
70

c.

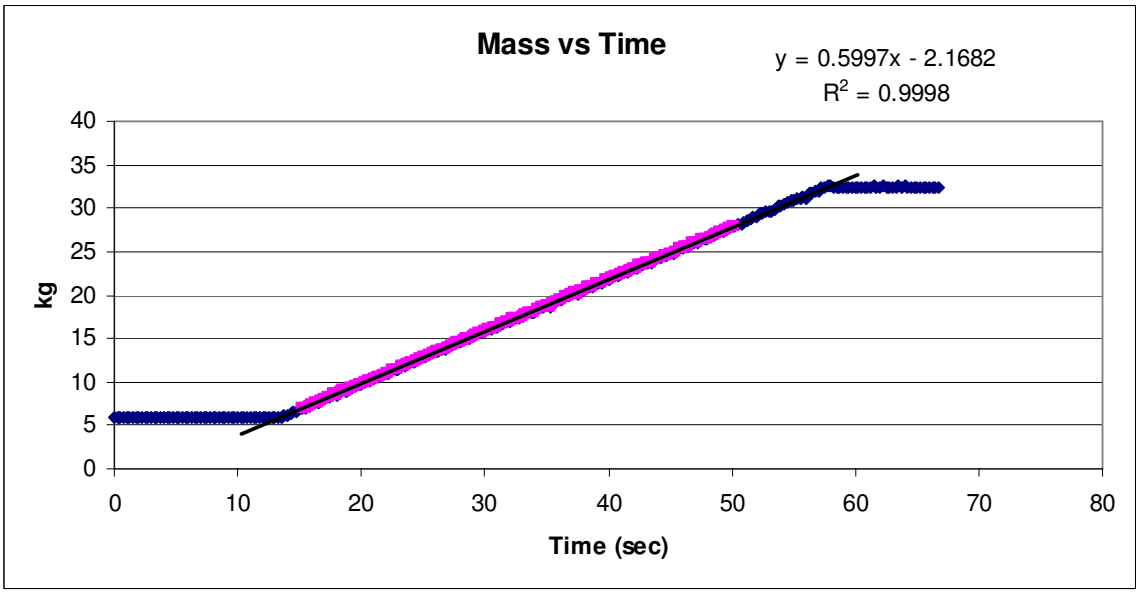
Mass vs Time
y = 0.5997x - 2.1682
R2 = 0.9998
kg
Time (sec)
0
5
10
15
20
25
30
35
40
0
10
20
30
40
50
60
70
80

d.

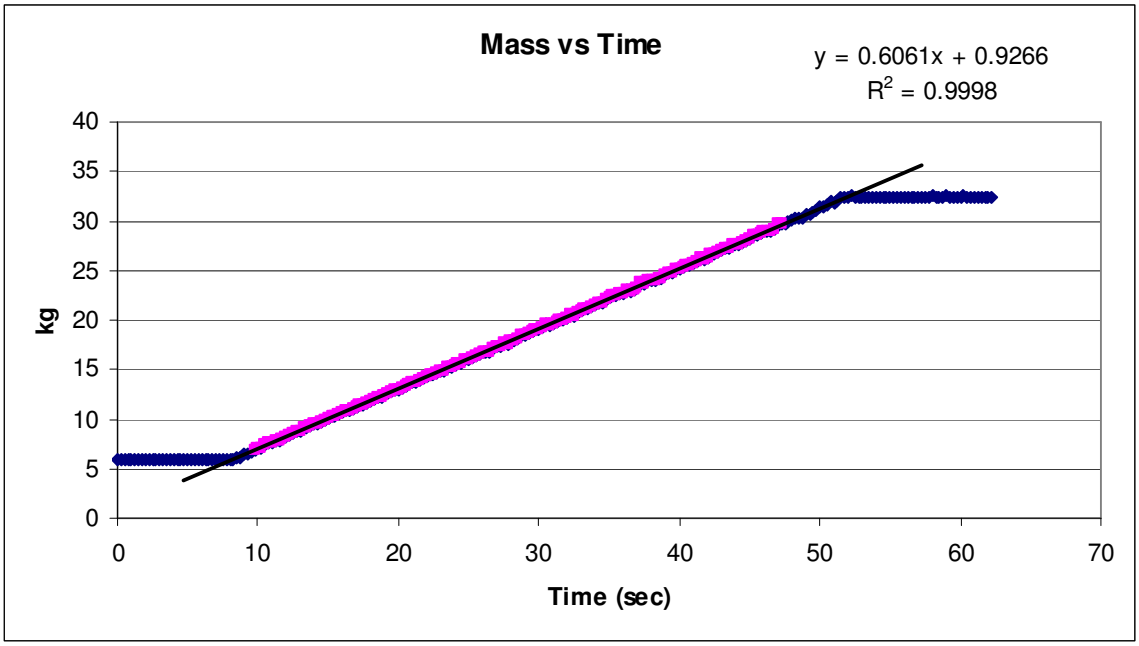

e.

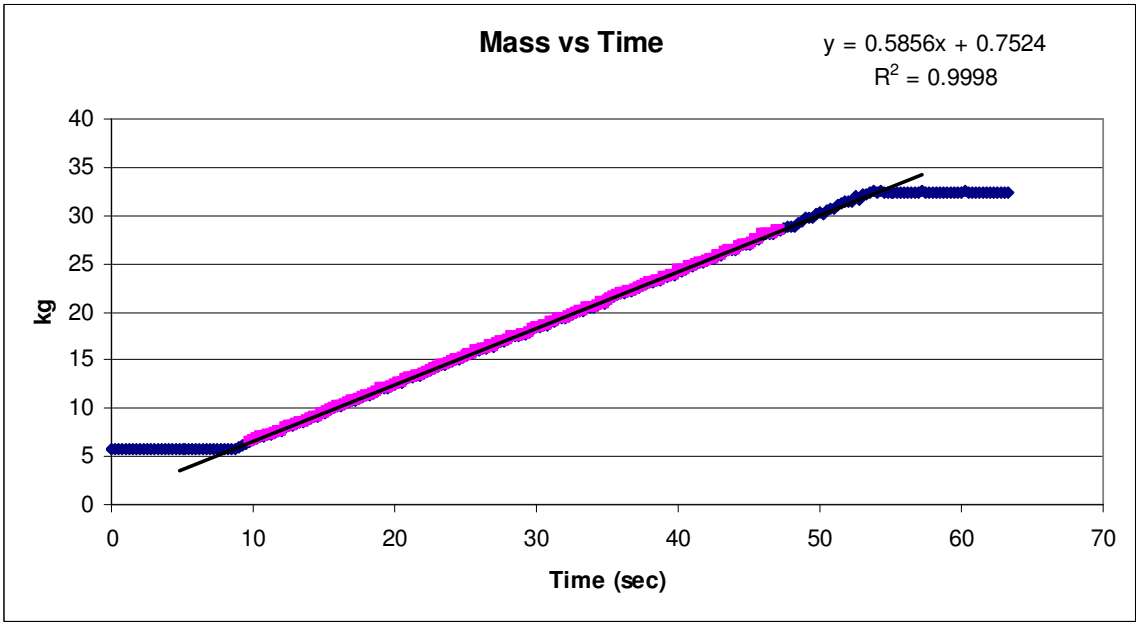

f.

Figure A.6 (a-f) – Data from lab scale 3 dimensional hopper with smooth walls. Slope of equation is the mass flow rate in kg/sec. Blue marks are collected data, purple marks represent data used to calculate the mass flow rate, and the solid black line is the mass flow rate equation in the top right. Time step used was .25 seconds.

Appendix B

Sample LIGGGHTS code

LIGGGHTS is a DEM simulation code that uses a command line interface style of input to run simulations. Thus, while getting a simulation up and running can take some trial and error, a running program can be changed to a completely different simulation just by altering a few variables. Below is an example script used to run a DEM simulation. While it contains values that are specific to this particular file, this is a very typical input script used for this study. Note that some lines which appear wrapped in this appendix are not wrapped in the original code.

```
#example liggghts code
#<----this denotes a comment; line is ignored

#setup - general world variables
atom_style granular
boundary   p f f
atom_modifysort  0 0
newton           off
communicatesingle vel yes
units      si

#region
region           box block 0 .016 0 .201 -.01 1 units box

create_box 2 box

neighbor   0.001 bin
neigh_modify     delay 0

#Material properties required for new pair styles

#Variables to define friction values
#These are varied between simulations
variable   fpp equal .122 #particle to particle friction
variable   fpw equal .799 #particle to wall friction
variable   rpp equal .122 #particle to particle rolling friction
variable   rpw equal .799 #paricle to wall rolling friction
```

```
fix        m1 all property/global youngsModulus peratomtype 1.1e6
2.16e6
fix        m2 all property/global poissonsRatio peratomtype 0.25
0.30
fix        m3 all property/global coefficientRestitution
peratomtypepair 2 0.9 0.5 0.5 0.5
fix        m4 all property/global coefficientFriction
peratomtypepair 2 ${fpp} ${fpw} ${fpw} ${fpw}
fix        m5 all property/global coefficientRollingFriction
peratomtypepair 2 ${rpp} ${rpw} ${rpw} ${rpw}


#This particular simulation uses the Hertz-Mindlin contact model
with rolling resistance off
pair_style gran/hertz/history rolling_friction off #Hertz without
cohesion
pair_coeff * *

timestep   0.00005

fix        1 all nve/sphere
fix        2 all gravity 9.81 vector 0.0 0.0 -1.0

#Material names/types
group      sand type 1
group      steel type 2


#This is where .stl files are imported into the simulation
#Changing these files determines if simulation is quasi or full
3D
#import hopper
fix        hopper all mesh/surface file hopper_open_2.stl type 2
curvature 0

#use hopper as wall
fix        granwalls all wall/gran/hertz/history mesh n_meshes 1
meshes hopper rolling_friction off

#insertion face
fix        inface steel mesh/surface/planar file
hopper_insert_2.stl type 1 move 0 0.05 .65

#valve
fix        valve all mesh/surface file valve.stl type 2 move 0
.07 0 curvature 0

#valve as wall
fix        granvalve all wall/gran/hertz/history mesh n_meshes 1
meshes valve rolling_friction off
```

```
#distributions for insertion
fix        pts1 sand particletemplate/sphere 1 atom_type 1
density constant 2500 radius constant 0.0035
fix        pdd1 sand particledistribution/discrete 1.  1 pts1 1.0

#group           nve_group region box

#particle insertion
fix        ins sand insert/stream seed 330 distributiontemplate
pdd1 &
                maxattempt 20 nparticles 5340 particlerate 2000
overlapcheck yes all_in no vel constant 0. 0. -1.0 &
                insertion_face inface extrude_length 0.1

#computations
fix        time all check/timestep/gran 100 .2 .2
thermo_style     custom step atoms
thermo           1000

variable   m equal mass(all,box)
variable   t equal step*dt
#variable  delta equal dt
fix        data all print 1000 "${t}, ${m}, ${fpp}, ${fpw},
${rpp}, ${rpw}" file
post/test_hertzhighfpp${fpp}fpw${fpw}rpp${rpp}rpw${rpw}.csv title
"time, mass, fpp, fpw, rpp, rpw"


#dump stl files and jpgs
#write out images, data files, and current .stl data if desired
dump       dmpics all image 10000
hertzhighcdtoff/dump*.hertzhighcdtoff6fpp${fpp}fpw${fpw}rpp${rpp}
rpw${rpw}.jpg type type adiam .007 view 90 0 center s .5 .5 .5
zoom 2 box yes .2 size 1500 3500
fix        data all print 1000 '${t}, ${m}, ${fpp}, ${fpw},
${rpp}, ${rpw}' append
hertzhighcdtoff/hertzhighcdtoff6fpp${fpp}fpw${fpw}rpp${rpp}rpw${r
pw}.csv title 'time, mass, fpp, fpw, rpp, rpw'


run        53400 upto

#stop particle insertion
unfix      ins

run        70000 upto

#open valve
unfix      granvalve

run        200000 upto
```

Appendix C

Error Analysis

The following tables show the values used in estimating the uncertainty of the measurement of mass flow rate using equations (61) through (65).. In general, bias errors are calculated using instrument manufacturers data on instrument precision, while random errors are calculated by statistical means.

Table C.1 – Uncertainty data from instruments used in measurement of mass flow rate.

Instrument	Relative uncertainty	Absolute uncertainty
Keli DEFY100 load cell	±0.03% full scale	1.079e-5 V
Agilent 34970A/34972A data scanner	±(.005 + .004)% of reading and range	4.37e-6 V
		.001 sec
Ohaus GT8000 scale		5e-5 kg

Table C.2 – Uncertainty data calculated by statistical methods from data in figures A.4 and A.5(a).

Measurement	Standard error	*t* factor
Calibration (kg/V)	0.6943	2
Mass flow rate (kg/sec)	9.76E-04	2
dV/dt (V/sec)	1.04E-06	2

References

Abengoa. "Abener Receives Asica Award for the PS20 construction." Abengoa press room archives. November 2009. Online: http://www.abengoa.com/web/en/noticias_y_publicaciones/noticias/historico/2009/11_noviembre/abe_20091126_1.html.

Aguirre, M. A., J. G. Grande, A. Calvo, L. A. Pugnaloni, J. –C. Geminard. "Granular Flow Through an Aperture: Pressure and Flow Rate are Independent" Physical Review E 83, 061305. 2010.

Ai, J., Chen, J-F., Rotter, J. M., and Ooi, J. "Assessment of Rolling Resistance Models in Discrete Element Simulations." Powder Technology, 206, pp. 269-282. 2011.

Baker, I. "A Treatise on Masonry Construction." 10th ed. John Wiley and Sons, Inc. New York. 1914.

Bates, L. "Case Studies." In "Introduction to Particle Technology" edited by Rhodes, M. 2nd edition. John Wiley and Sons Ltd. West Sussex, England. 2008.

Carson, J. W., Troxel, T. J., and Bengston, K. E. "Scaling Up Solids Handling Processes and Equipment: Limits of Theory and Scale Modeling." Jenike & Johanson, Inc, Tyngsboro, MA, United States. 2008.

Cundall, P. A., and Strack, O. D.. "A discrete numerical model for granular assemblies." Géotechnique 29, No. 1, pp. 47-65. 1979.

DEM Solutions Ltd. www.dem-solutions.com. 2013.

Di Renzo, A., and Di Maio, F. P. "Comparison of contact-force models for the simulation of collisions in DEM-based granular flow codes." Chemical Engineering Science, 59, pp. 525-541. 2004.

Drescher, A. "On the Criteria for Mass Flow in Hoppers." Powder Technology, 73, pp. 251-260. 1992.

Ghazavi, M., Hosseini, M., and Mollanouri, M. "A Comparison Between Angle of Repose and Friction angle of Sand." The 12th International Conference of International Association for Computer Methods and Advances in Geomechanics. pp. 1272-1275. 2008.

González-Montellano, C., Ramírez, A., Gallego, E., and Ayuga, F. "Validation and Experimental Calibration of 3D Discrete Element Models for the Simulation of the Discharge Flow in Silos." Chemical Engineering Science, 66, pp. 5116-5126. 2011.

Hertz, H. “On the Contanct of Elastic Solids.” Journal für die reine und angewandte Mathematik, 92, pp. 156-171. 1881.

Jenike, A. “Steady Gravity Flow of Frictional-Cohesive Solids in Converging Channels.” Journal of Applied Mechanics, 31, pp. 5-11. 1964.

Jenike, A. W. “Better Design for Bulk Handling.” Chemical Engineering, 61, pp. 175-180. 1954.

Jenike, A. W. “Principles of Flow of Solids in Bins.” Mining Engineering, 20, pp. 67-68. 1968.

Jenike, A., and Shield, R. “On the Plastic Flow of Coulomb Solids Beyond Original Failure.” Journal of Applied Mechanics, 26, pp. 599-602. 1959.

Ketterhagen, W., Curtis, J., Wassgren, C., and Hancock, B. “Predicting the Flow Mode from Hoppers Using the Discrete Element Method.” Power Technology, 195, pp. 1-10. 2009.

Kloss, C., Goniva, C., Hager, A., Amberger, S., and Pirker, S. “Models, Algorithms, and Validation for Opensource DEM and CFD-DEM.” Progress in Computational Fluid Dynamics, An Int. J., 12, pp. 140-152. 2012. Online: www.liggghts.com.

Kruggel-Emden, H., Wirtz, S., Simsek, E., and Scherer, V. “Modeling of Granular Flow and Combined Heat Transfer in Hoppers by the Discrete Element Method (DEM).” Journal of Pressure Vessel Technology, 128, pp. 439-444. 2006.

Li, Y., Xu, Y., and Thornton, C. “A Comparison of Discrete Element Simulations and Experiments for ‘Sandpiles’ Composed of Spherical Particles.” Powder Technology, 160, pp. 219-228. 2005.

Lorenz, A., Tuozzolo, C., and Louge, M. “Measurements of Impact Properties of Small, Nearly Spherical Particles.” Experimental Mechanics, 37, No.3, pp. 292-298. 1997.

Marinelli, J. “Food Powder Properties.” In “Ecapsulated and Powdered Foods.” Onwulata, C. (editor). CRC Press: Boca Raton, Fl. 2005.

Marinelli, J., and Carson, J. “Solve Solids Flow Problems in Bins, Hoppers, and Feeders.” Chemical Engineering Progress, 1992. Online: http://rdptech.com/technical-resources/biosolids-storage-and-conveying-systems/solids-flow-bins-hoppers-feeders-marinelli.pdf.

Mindlin, R. D. and Deresiewicz, H. “Elastic Spheres in Contanct Under Varying Oblique Forces.” Journal of Applied Mechanics, 20, pp. 327-344. 1953.

Nguyen, T. V., Brennen, C. E., and Sabersky, R. H. “Funnel Flow in Hoppers.” Journal of Applied Mechanics, 47, pp. 729-735. 1980.

Plimpton, S. “Fast Parallel Algorithms for Short-Range Molecular Dynamics.” J Comp Phys, 117, pp. 1-19. 1995. Online: lammps.sandia.gov.

Rao, S. “Discharge dynamics from hoppers: a discrete element method (DEM) study.” ME 8893 special topics report. Georgia Institute of Technology. 2012.

Roberts, A. “Characterisation for Hopper and Stockpile Design.” From “Characterisation of Bulk Solids,” McGlinchey (editor). Blackwell Publishing Ltd., Oxford, UK. 2005.

Schultze, D. “Storage of Powders and Bulk Solids in Silos.” Technical paper. Online: http://www.dietmar-schulze.de/fre.html. 2011.

Schwedes, J. “Review on Testers for Measuring Flow Properties of Bulk Solids.” Granular Matter 5, pp. 1-43. 2003.

Simsek, E., Brosch, B., Wirtz, S., Scherer, V., and Krüll, F. “Numerical Simulation of Grate Firing Systems Using a Coupled CFD/Discrete Element Method (DEM).” Powder Technology, 193, pp. 266-273. 2009.

The Georgia Institute of Technology. “PACE: A Partnership for an Advanced Computing Environment.” www.pace.gatech.edu. 2013.

Vargas, W., and McCarthy, J. “Heat Conduction in Granular Materials.” AIChE Journal, 47, pp. 1052-1059. 2001.

Walton, O. R. and Braun, R. L. “Viscosity, granular-temperature, and stress calculations for shearing assemblies of inelastic, frictional discs.” Journal of Rheology, 30, No. 5. pp. 949-980. 1986.

Wheeler, A., and Ganji, A. “Introduction to Engineering Experimentation.” 1st edition. Prentice Hall, Englewood Cliffs, New Jersey, United States. 1996.

Wu, A., and Sun, Y. “Granular Dynamic Theory and its Applications.” Metallurgical Industry Press, Beijing and Springer-Verlang GmbH Berlin Heidelberg. 2008.

Zhou, Y. C., Xu, B. H., Yu, A. B. and Zulli, P. “An Experimental and Numerical Study of the Angle of Repose of Coarse Spheres.” Powder Technology, 125, pp. 45-54. 2002.